UNIVERSIDADE DE SÃO PAULO
INSTITUTO DE FÍSICA DE SÃO CARLOS

POLIANA HEIFFIG PENTEADO

Transport through leaked Majorana modes in quantum dots and adatoms

São Carlos

2013

POLIANA HEIFFIG PENTEADO

Transport through leaked Majorana modes in quantum dots and adatoms

Tese apresentada ao Programa de Pós-Graduação em Física do Instituto de Física de São Carlos da Universidade de São Paulo, para obtenção do título de Doutor em Ciências.

Área de concentração: Física Básica Orientador: Prof. Dr. José Carlos Egues

Versão Corrigida

(Versão original disponível na Unidade que aloja o Programa)

São Carlos

2013

AUTORIZO A REPRODUÇÃO E DIVULGAÇÃO TOTAL OU PARCIAL DESTE TRABALHO, POR QUALQUER MEIO CONVENCIONAL OU ELETRÔNICO PARA FINS DE ESTUDO E PESQUISA, DESDE QUE CITADA A FONTE.

Ficha catalográfica elaborada pelo Serviço de Biblioteca e Informação do IFSC,
com os dados fornecidos pelo(a) autor(a)

Heiffig Penteado, Poliana
Transport through leaked Majorana modes in quantum dots and adatoms / Poliana Heiffig Penteado; orientador Jose Carlos Egues - versão corrigida -- São Carlos, 2013.
117 p.

Tese (Doutorado - Programa de Pós-Graduação em Física Básica) -- Instituto de Física de São Carlos, Universidade de São Paulo, 2013.

1. Quantum transport. 2. Spin diode. 3. Majorana zero modes. 4. Kitaev model. 5. Green\'s functions. I. Egues, Jose Carlos , orient. II. Título.

To my parents Paulo and Stella
and to my sister Juliana

ACKNOWLEDGMENTS

I would like to thank all the people who direct and/or indirectly contributed to my accomplishing this thesis.

My first and sincere appreciation goes to my advisor Carlos Egues for all I have learned from him and for his continuous help and support in all stages of this thesis. I would also like to thank Carlos for providing me the opportunity to interact with internationally important groups, to participate in international conferences, to take part in the organization of workshops, conferences, etc., while still a PhD student. These opportunities certainly contributed a great deal to enriching my scientific experience.

I am grateful to the members of our group at IFSC: Gerson, Marco, Fu, Denis and Vernek for the enlightening physics discussions. Special thanks goes to Professors Fabricio M. Souza and Edson Vernek, both from Federal University of Uberlandia, for their patience, assistance and guidance during the development of the two different topics treated in this thesis. I also would like to thank our secretary Cris for all the administrative work, and the IFSC and library staff members for the technical support.

As a PhD student, I had the privilege of meeting and collaborating with remarkable people. Among them, I am grateful to Prof. Patrik Recher for the hospitality during my stays at the University of Würzburg and at the Technical University of Braunschweig. In addition, I thank Prof. Recher and his former post doc Paolo Michetti, as well as his PhD student Benedikt Probst, for the valuable physics discussions, which for sure contributed to my maturing as a physicist. I also thank Prof. Daniel Loss for the hospitality during my several visits to his group at the University of Basel.

I consider myself fortunate to have had the opportunity to get to know Mrs. Karie Friedman, a former editor of Reviews of Modern Physics. I thank her for contributing a great deal to the improvement of my spoken as well as written English skills. I also appreciate very much our lovely chats about life in general and how much I have learned from her experience during her stays at IFSC as an in-house Editor.

Last but not least, I would like to specially thank my parents and my sister for always believing in me, for their continuous love and support. Without them I could not have made it here. I also would like to express my gratitude to Alessandra, Marcos Felipe and Lucilda for their friendship in tough times, and to those who even not being around during my PhD, were certainly present in thought: Aline, Carina and Daniela.

This work was funded by CAPES
and PRP/USP within the Research Support
Center Initiative (NAP Q-NANO)

“You cannot teach a man anything;
you can only help him discover it in himself.”
Galileo Galilei

RESUMO

PENTEADO, P. H. **Transporte através de modos de Majorana em pontos quânticos e adátomos**. 2013. pp. Tese (Doutor em Ciências) - Instituto de Física de São Carlos, Universidade de São Paulo, São Carlos, 2013.

Nesta tese investigamos transporte quântico ressonante em dois sistemas diferentes: (i) uma ponta STM ferromagnética acoplada a um átomo (interagente) adsorvido em uma superfície metálica ou semicondutora, e (ii) um ponto quântico conectado a reservatórios de elétrons e lateralmente acoplado a um nanofio supercondutor que possui modos de Majorana (cadeia Kitaev). Ambos os problemas são estudados no contexto de funções de Green, o que nos permite determinar as propriedades de transporte do sistema. Na primeira configuração, devido à natureza ferromagnética e não magnética da ponta STM e da superfície e, respectivamente, é possível obter o efeito diodo de spin, que ocorre apenas no regime em que o adátomo está ocupado com um único elétron. Além disso, por causa da presença do átomo adsorvido sobre a superfície, oscilções de Friedel são observadas na corrente. O segundo sistema é diferente do primeiro, principalmente pela ausência da interação de Coloumb e pelo fato de não ter spin. Curiosamente, vemos que o modo de Majorana do fio vai para o ponto quântico dando origem assim a um modo com energia zero no ponto quântico localizado sempre no nível de Fermi dos contatos. Surpreendentemente, essa ressonância ocorre mesmo quando o nível do ponto quântico, controlado por uma tensão externa, está muito acima ou muito abaixo do nível de Fermi dos contatos. Propomos três possíveis cenários experimentais para identificar de maneira conclusiva este modo de Majorana em fios através do modo que aparece no ponto quântico.

Palavras-chave: Transporte quântico. Funções de Green. Diodo de spin. Férmions de Majorana. Modelo de Kitaev. Modos de energia zero.

ABSTRACT

PENTEADO, P. H. **Transport through leaked Majorana modes in quantum dots and adatoms**. 2013. pp. Thesis (Doctor of Philosophy in Physics) - Instituto de Física de São Carlos, Universidade de São Paulo, São Carlos, 2013.

We investigate quantum resonant transport in two different systems: (i) a ferromagnetic Scanning Tunneling Microscope (STM) tip coupled to an adatom (interacting) on a host surface (metallic or semiconductor), and (ii) a quantum dot connected to source and drain leads and side-coupled to a superconducting nanowire sustaining Majorana zero modes (Kitaev chain). Both problems are studied within the Green's functions approach, which allows us to determine the transport properties of the system. In the first setup, due to the ferromagnetic and nonmagnetic 'natures' of the tip and host, respectively, it is possible to obtain the spin-diode effect, which occurs only in the singly occupied regime. In addition, because of the presence of the adsorbed atom on the surface, Friedel oscillations are observed in the current. The second system differs from the first mainly because it is spinless and there is no Coloumb interaction. Interestingly, we find that the Majorana mode of the wire leaks into the dot thus giving rise to a Majorana (zero mode) resonance in the dot, pinned to the Fermi level of the leads. Surprisingly, this resonance occurs even when the gate-controlled dot level is far above or far below the Fermi level of the leads. We study three possible experimental scenarios to probe unambigoulsy this Majorana mode in wires via these leaked/pinned modes.

Keywords: Quantum transport. Green's functions. Spin-diode. Majorana fermions. Kitaev model. Zero modes

List of Figures

Figure 1.1 - Illustration of a quantum dot (QD) coupled to two electron reservoirs. A bias voltage V applied to system leads to an imbalance in the chemical potential of the contacts resulting in current flow in the system. The gate voltage V_g controls the energy levels of the dot. The parameters Γ^{L} and $\Gamma^{\mathrm{R}}_{\uparrow}$ ($\Gamma^{\mathrm{R}}_{\downarrow}$) correspond to the tunneling rates associated to the left and right (spin-dependent) leads, respectively. 28

Figure 1.2 - Sketch of the Coulomb blockade regime. The region in the middle represents a single level (spin degenerate) quantum dot separating two electron reservoirs whose chemical potentials are μ_L (left) and μ_R (right). When this level with energy ε_d is occupied, the next electron that will hop into the dot has to pay an energy $\varepsilon_d + U$ due to the Coulomb interaction U. 29

Figure 1.3 - Sketch of the energy states (a). The green rectangle indicates the tunnel barrier separating the normal part of the nanowire on the left from the wire section with induced superconducting gap Δ. An external voltage V is applied between the normal and the superconductor. The red stars illustrate the locations of the Majorana pair. (b) Differential conductance as a function of the applied bias voltage for various values of magnetic field. The dashed red line emphasizes the zero-energy peak. Figure taken from Ref. (1). 33

Figure 2.1 - Ferromagnetic Scanning Tunneling Microscope (FM-STM) tip coupled to a host surface with an adatom. The matrix elements t_{12}, t_{13} and t_{23} represent the couplings tip-adatom, tip-surface and adatom-surface, respectively. The tip-adatom lateral distance is denoted by R. 38

Figure 2.2 - Illustration of the time contour used in the definition of the contour-ordered Green's functions. The transient branch $t_0 - i\beta$ can be neglected in our study since we are only interested in the steady state current. . . . 41

Figure 2.3 - Adatom occupations and magnetization as functions of the lateral tip position R for both forward $eV = 30 < \Gamma_0$ (solid lines) and reverse $eV = -30\Gamma_0$ (dashed lines) bias voltages. The blue and red curves (solid and dashed) represent the spin up and down populations, respectively. The black curves correspond to the magnetization of the system $m = n_\uparrow - n_\downarrow$. 55

Figure 2.4 - Spin-resolved currents against the tip position R. Both negative (dashed lines) and positive (solid lines) bias voltages are shown. For $|eV| = 30\Gamma_0$ only single occupancy (i.e., $\varepsilon_\sigma + U$ is much higher than the emitter chemical potential) is allowed. This results in the spin-diode effect: for negative bias voltages the current is polarized for all R values while for positive biases the current polarization goes to zero when the tip is close to the adatom. 56

Figure 2.5 - Blow up of the spin-polarized currents for a range of R in which only the direct tip-host tunneling is relevant. The dashed line corresponds to the current obtained via Eq. (2.22). An agreement between the dashed and solid lines should be reached in the large-R limit. (a) Spin-up current (solid gray line) for $V < 0$; the thicker solid line represents the LDOS at the Fermi level. (b) Spin-down current (solid gray line) for $V < 0$. (c) Spin-up current (solid black line) for $V > 0$. (d) Spin-udown current (solid black line) for $V > 0$. 57

Figure 2.6 - Similar to Fig. 2.3 except that $|eV| = 80\Gamma_0$ here. This bias allows double occupancy of the adatom. For forward voltages (solid lines) the adatom becomes doubly occupied for large R values ($n_\uparrow + n_\downarrow = 2$). 58

Figure 2.7 - Similar to Fig. 2.4 except that $|eV| = 80\Gamma_0$ here. This bias allows double occupancy of the adatom. In this regime no spin-diode effect is observed. The spin polarized currents are the same (in modulus) for both positive and negative eV. 58

Figure 2.8 - Zoom of the spin-resolved currents in the range of negligible tip-adatom coupling. 59

Figure 2.9 - (a) Current polarization against R. In the single occupancy regime ($eV = \pm 30\Gamma_0$, solid lines) the current polarization is approximately constant for reverse bias ($V < 0$, red curve) and goes down to zero for direct bias ($V > 0$, black curve) when the tip is close to the adatom. In the case of double occupancy ($eV = \pm 80\Gamma_0$, dashed lines) the current polarization is suppressed for small R, however it does not vanish; notice that the dashed lines lie essentially on top of each other. For large R's, the polarization for both single and double occupancies tends to a plateau and presents tiny oscillations (b). 60

Figure 3.1 - Bulk energy for the Kitaev model as a function of k for $\Delta = 0.4t$ and several values of μ. The solid blue curves represent the energy in the absence of superconductivity. The dashed red lines show what when $\Delta \neq 0$ a gap opens at $k = \pm\pi/2$ (a). In (b) $|\mu| > t$ and we are in the trivial gapped phase. The panels (c) and (d) show that when $\mu = -t$ or t the gap closes at $k = 0$ or $k = \pm\pi$, respectively, indicating that there are different phases conneted by a gap close. 64

Figure 3.2 - Illustration of the Hamiltonian in Eq. (3.14) for (a) $\mu \neq 0$ and $\Delta = t = 0$, and (b) $\mu = 0$ and $\Delta = t \neq 0$. 66

Figure 3.3 - Illustration of the real setup. A nanowire, e.g., InSb, with spin-orbit interaction in proximity to a bulk s-wave superconductor. e.g., Nb. The gate electrodes tune the chemical potential of the wire such that the topological regime is reached. Majorana fermions γ_1 and γ_2 appear on the edges of the wire. This figure was taken from the review by Leijnse and Flensberg (2). 71

Figure 3.4 - Energy dispersion relation of Hamiltonian (3.28) with $|\tilde{B}| = 0$ (a). When the magnetic field is switched on (b), the bands are split. (c) Effect of a more intense magnetic field. (d) Energy bands when the superconducting pairing potential Δ is non-zero. 72

Figure 4.1 - Representation of a quantum dot (QD) coupled to source (S) and drain (D) metallic leads and connected to a Kitaev chain. The system dot+leads is considered as a site of the wire, however, with a distinct coupling parameter t_0 and no induced superconductivity $\Delta = 0$. 76

Figure 4.2 - Illustration of the system using the Majorana representation. 77

Figure 4.3 - Illustration of the recursive method used to obtain the Green's function of the dot. (a) Representation of the system. (b) and (c) show the first and second steps, respectively, of the process. In each of them the Green's function of the last site added is exactly calculated. 79

Figure 4.4 - Density of states of a dot ρ_{dot} coupled to source and drain leads as a function of the energy ε. The four curves correspond to different values of ε_{dot}: black $\varepsilon_{\text{dot}} = 0$, red $\varepsilon_{\text{dot}} = -2\Gamma_L$, blue $\varepsilon_{\text{dot}} = -4\Gamma_L$ and green $\varepsilon_{\text{dot}} = 5\Gamma_L$. 85

Figure 4.5 - Conductance of the system as a function of the applied gate potential. Single peak centered at $\varepsilon_{\text{dot}} = 0$ when the dot level is aligned with the Fermi level of the leads. 85

Figure 4.6 - Density of states of a usual tight-binding chain. The dot can be viewed as a site of the chain since $V_L = 0$ and $t_0 = t/2$. The two curves represent the DOS for a site on the edge ρ_{edge} (solid black line) and in the bulk ρ_{bulk} (dashed red line). 87

Figure 4.7 - Local density of states for the site on the edge ρ_{edge} (solid black line) and in the bulk ρ_{bulk} (dashed red line) of the Kitaev chain as functions of the energy with $t_0 = 0$, $\Delta = 0.2t$ and $\mu = 0$. 88

Figure 4.8 - Dot (a) and first chain site (b) LDOS, ρ_{dot} and ρ_1, respectively, as functions of the energy ε for several values of t_0, $\varepsilon_{\text{dot}} = -5\Gamma_L$, $\Delta = 0.2t$ and $\mu = 0$. 88

Figure 4.9 - $\rho_{\text{dot}}/\rho_{\text{dot}}^{\max}$ (solid purple line) and $\rho_1/\rho_1^{\max}$ (dot-dashed pink line) at $\varepsilon = 0$ as functions of the dot-wire coupling t_0, with $\rho_{\text{dot}(1)} = \max[\rho_{\text{dot}(1)}(\varepsilon = 0, t_0)]$ 89

Figure 4.10 -LDOS of the second site ρ_2 in the Kitaev chain as a function of ε for several values of t_0 (a). In (b) we show a blowup of ρ_2 to emphasize the small magnitude of the peaks. 89

Figure 4.11 -LDOS of the third site ρ_3 in the Kitaev chain as a function of ε for different values of t_0 (a). In (b) we show a blowup of ρ_2 to emphasize the small magnitude of the peaks. 90

Figure 4.12 -LDOS for the dot, first site and a site in the middle of the chain. The Majorana zero mode has completely leaked to the dot for $t_0 = 100\Gamma_L$. . . 90

Figure 4.13 -Color map of the electronic density of states as a function of ε and eV_g. The two horizontal lines at eV_{g1} (dot-dashed yellow line) and eV_{g2} (dashed yellow line) represent plots similar to those seen in Fig. 4.8. . . 91

Figure 4.14 -Sketch of the dot LDOS for the Majorana (left) and Kondo (right) cases. 91

Figure 4.15 -Two-terminal conductance G of the system as a function of the applied gate voltage eV_g. The solid curves correspond to $\Delta = 0.2t$ and the dashed ones to $\Delta = 0$ for distinct μ. 92

Figure 4.16 -Color map of the Majorana density of states as a function of ε and eV_g of the dot Majoranas A (a) and B (b) and of the first site of the Kitaev chain, (c) and (d), respectively. 93

Figure 4.17 -Conductance G as a function of the chemical potential μ. In (a) we fix the dot-wire coupling t_0 and vary ε_{dot} and in (b) we set $\varepsilon_{\text{dot}} = 0$ for several values of t_0, both for $\Delta = 0.2t$. 93

Figure 4.18 -Conductance G as a function of μ for $\Delta = 0$. Panels (a) and (b) show, respectively, curves for $t_0 = 10\Gamma_L$ and different values of ε_{dot} and $\varepsilon_{\text{dot}} = 0$ for several values of t_0. The parameters are the same as those in Fig. 4.17. 94

Figure 4.19 -Conductance G as a function of μ for $\Delta = t$. In (a) we set $t_0 = 10\Gamma_L$ and vary ε_{dot}. In (b) we fix $\varepsilon_{\text{dot}} = -5\Gamma_L$ for different values of t_0. 95

Figure A.1 - Semi-infinite wire modeling the leads of our setup (a). The sites are coupled by a hopping parameter $t = D/2$. In (b) we illustrate the “real” coupled system we solve: a site 1 of the original chain connected to a site $\tilde{2}$ renormalized by the rest of the chain (c). If another site is added to the already renormalized site nothing changes essentially, that is $\tilde{1} = \tilde{2}$” (d). 116

Figure A.2 - Linear behavior of the real part (red curve) of $G_L\left(\varepsilon\right)$ within the edges of the conduction band $D = 10t$, $t = 10$ meV, and DOS of the leads (black curve). 117

List of Tables

Table 2.1 - Parameters used in the self-consistent calculation. 53

Summary

1 Introduction **27**

1.1 Majorana Fermions 30

1.1.1 Majorana fermion properties 33

1.2 Outline of this thesis 35

2 Ferromagnetic STM tip operating as a spin-diode **37**

2.1 Description of the system 37

2.2 Non-resonant transport 39

2.3 Transmission coefficient calculation 43

2.4 Calculating $\rho_\sigma(\mathbf{R}, \omega)$ for the subsystem adatom+surface 45

2.5 Resonant + non-resonant transport 46

2.6 Matrix Green's function formulation 49

2.7 Numerical technique 53

2.8 Results 54

2.8.1 Single Occupancy 54

2.8.2 Double Occupancy 57

2.8.3 Current Polarization 59

3 Majorana Fermions: “sneaky” fermions 61

3.1 Kitaev model 62

3.2 Practical realization of Majorana modes in superconducting 1D nanowires . . . 68

3.2.1 Real system 70

4 Majorana leaking into a quantum dot connected to a Kitaev wire 75

4.1 Description of the system 75

4.2 Recursive Green’s functions and related physical quantities 78

4.2.1 Equation of motion for $G_{\alpha d\beta d}(t,t')$ 80

4.3 Results 83

4.3.1 Some analytical results 83

4.4 Numerical results 87

5 Conclusions 97

REFERENCES 99

APPENDICES 110

A Some analytical results 113

Chapter 1

Introduction

Nanotechnology - manipulation of matter with at least one dimension sized from 1 to 100 nanometers - has imposed a new paradigm for the development of electronic devices. Its definition reflects the fact that at ‘nanoscale’, quantum mechanical effects are important and a quantum transport description is necessary.

The typical system we are interested in studying is composed of a two-terminal device consisting of charge reservoirs bridged by a nanoscale object, namely a quantum dot (QD), see Fig. 1.1. Transport through quantum constrictions such as nanowires and quantum dots presents peculiar quantum signatures in, e.g., the measured conductance. In this context, quantum transport offers a unique and powerful tool to probe fundamental physical phenomena, e.g., spin-dependent transport, a subject of intense study in the field of spintronics, due to its potential application in the development of spin-based devices (3, 4).

In a narrow sense spintronics refers to ‘spin control of electronics’, i.e., flipping a spin or turning on a magnetic field would result ideally, for example, in the cessation of the current flowing in a given system. The wishful thinking is a device that would orient spin by passing a current or applying a gate voltage. In this way the spin would be fully integrated with electronics, what would allows us to write, store and manipulate, as well as read the information based on spin (5). In metallic systems, ‘spintronics’ is related, e.g., to the study of the effect known as tunneling magnetoresistance (TMR) (6), in which an increase of the conductance of a system composed of two ferromagnets separated by a thin insulator is observed when the magnetization of both ferromagnets is parallel aligned. This effect arises if the insulating layer is thin enough (typically a few nanometers), so electrons can tunnel from one ferromagnet into the other. The effect is also present in double ferromagnetic junctions connected via a metallic island or a quantum dot (7), and is used in technological applications such as read-heads of hard disk drives.

Another interesting effect emerges when a dot is coupled to two metallic/semiconductor contacts: one nonmagnetic (NM) and the other ferromagnetic (FM). In Fig. 1.1 we show this setup, a quantum dot coupled to NM and FM leads. Electrons can tunnel in both directions depending on the sign of the applied bias voltage (V) (e.g., V>0 electrons go from the NM to the FM lead) and the gate voltage V_g controls the energy levels of the dot. It was pointed out that this system, in a particular bias voltage range, can operate as a spin-filter and as a spin-diode (8). In a further work, Souza *et al.* (9) showed that in a similar system, however, in the presence of the electron-electron interaction in the dot, when the nonmagnetic lead operates as the source and the ferromagnetic lead as the drain of electrons (V>0), the current flowing in the system is unpolarized. In the opposite scenario, i.e., when the ferromagnetic lead is the emitter and the nonmagnetic lead is the collector (V<0), a spin-polarized current arises. This rectification of the current occurs again in a particular range voltage when the dot is singly occupied or in the so-called Coulomb-blockade (spin-dependent in this case) regime (10, 11). This regime comes about when the energy level ε_d of a dot is occupied and another electron tries to hop into the dot. Because of the Coulomb interaction, this electron has to pay an extra energy $\varepsilon_d + U$ to get in. If the level $\varepsilon_d + U$ is above the Fermi energy of the leads, the electron is blockaded and hence not allowed to go in the dot, see Fig. 1.2. Therefore the spin-diode effect arises essentially due to an interplay between the Coulomb interaction and the spin-accumulation in the dot.

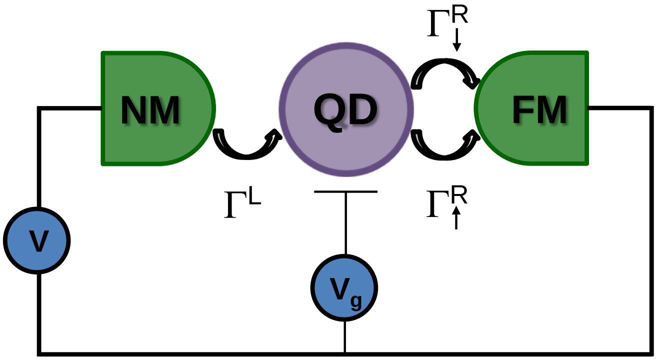

Figure 1.1 – Illustration of a quantum dot (QD) coupled to two electron reservoirs. A bias voltage V applied to system leads to an imbalance in the chemical potential of the contacts resulting in current flow in the system. The gate voltage V_g controls the energy levels of the dot. The parameters Γ^L and $\Gamma^R_\uparrow$ ($\Gamma^R_\downarrow$) correspond to the tunneling rates associated to the left and right (spin-dependent) leads, respectively.

In this thesis, we calculate the transport properties (e.g., conductance and current) of two different systems. One of them is an outgrowth of the work mentioned above (9). We basically

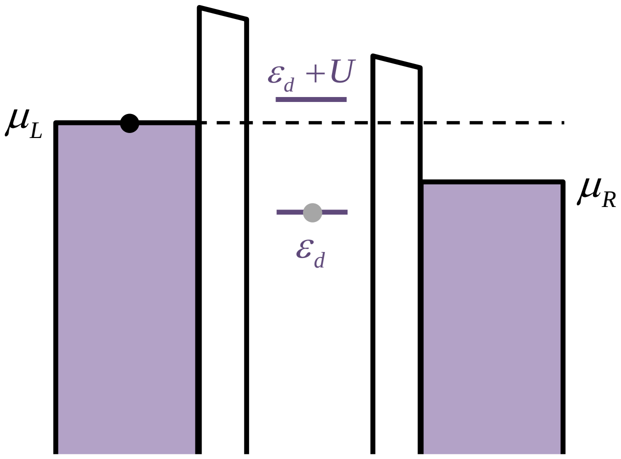

Figure 1.2 – Sketch of the Coulomb blockade regime. The region in the middle represents a single level (spin degenerate) quantum dot separating two electron reservoirs whose chemical potentials are μ_L (left) and μ_R (right). When this level with energy ε_d is occupied, the next electron that will hop into the dot has to pay an energy $\varepsilon_d + U$ due to the Coulomb interaction U.

have the same setup as shown in Fig. 1.1, however, the role of the FM contact is played by a Scanning Tunneling Microscope (STM) tip, the dot is replaced by an atom adsorbed on a metallic/semiconductor surface that works as the nonmagnetic lead. The additional feature of this system is that the STM tip can be moved along the surface from a position right on top of the atom to far away from it. The electrons can tunnel from the tip directly to the surface or via the adatom. Because of the nature of the leads (ferromagnetic tip and nonmagnetic surface) we can observe the spin-diode effect. In addition, due to the presence of the adatom (impurity), we can see the emergence of spin-dependent Friedel oscillations in the current, a manifestation of the oscillations in the density of states of the subsystem surface+adatom (12). The density of states and the current of the system are determined within the nonequilibrium Green's functions approach (Keldysh formalism), which allows us to deal with the electron-electron interaction in the dot and to go beyond the linear response regime.

The other problem we address is connected to the recent and interesting topic of Majorana fermions (13). We study a setup consisting of a semiconducting nanowire modeled by a Kitaev chain and side-coupled to a quantum dot connected to two nonmagnetic metallic leads. We theoretically calculate the conductance of the system through the quantum dot and propose three different ways of experimentally probing the Majorana mode. The calculation is performed within the linear response regime using the Green's functions formalism. In the following sections, we discuss the properties of the Majoranas, the current status of the research in this field and describe in detail the setup we study.

1.1 Majorana Fermions

Spin-$1/2$ fermions coupled to an electromagnetic field obey the Dirac relativistic quantum equation (14)

$$i\hbar\frac{\partial\psi}{\partial t}=\left[c\alpha\cdot\left(\mathbf{p}-\frac{e}{c}\mathbf{A}\right)+\beta mc^2+e\Phi\right]\psi, \tag{1.1}$$

where α and β are 4×4 matrices written as

$$\alpha=\begin{pmatrix}0 & \sigma\\ \sigma & 0\end{pmatrix},\ \text{and}\quad \beta=\begin{pmatrix}I_{2\times2} & 0\\ 0 & -I_{2\times2}\end{pmatrix}, \tag{1.2}$$

which satisfy the anti-commutation relations

$$\left\{\alpha_j,\alpha_k\right\}=2\delta_{j,k},\quad \left\{\alpha_j,\beta\right\}=0\quad\text{and}\quad\beta^2=1. \tag{1.3}$$

The vector α represents the Pauli matrices and ψ is a four-component spinor describing the fermion field. In general, Eq. (1.1) has complex solutions ψ that are not eigenstates of the charge conjugation operator, under the action of which, particles and antiparticles are transformed into one another $\psi\rightarrow\psi^*$. This means that a complex solution of (1.1) represents a fermion that has a distinct anti-fermion (e.g., electron and positron, respectively), having the same energy and spin, but opposite charge and magnetic moment (15). In the quantum field theory language, if a given field φ creates a particle A (destroys the antiparticle $\bar{A}$), the complex field φ^* will create $\bar{A}$ and destroy A. Therefore, particles that are their own antiparticles must be described by real fields φ, which obey $\varphi=\varphi^*$ and are eigenstates of the charge conjugation operator.

The natural question now would be "is it possible to find real solutions that satisfy a Dirac-type equation?". In 1937, Ettore Majorana (16) posed and answered this query by discovering a modification of Dirac equation that involves only real quantities. The real solutions to this equation correspond to neutral-charge fermions, known as Majorana fermions. Electrically neutral particles and the identification $\varphi=\varphi^*$ are quite usual features among bosons, being the photon a standard example. No one knows, however, whether Majorana particles (fermions) exist in nature as building blocks. Majorana himself speculated that his equation could be applied to neutrinos, but even today this is still an open question in particle physics (17).

In solid-state physics though, recent investigations suggest that condensed matter systems may offer the possibility of observing these exotic particles (18–21). In this context, Majorana fermions do not refer to elementary particles but rather to quasiparticles bound states, which correspond to low-energy collective excitations of a complicated many-body system. An example of such an excitation that is its own antiparticle is the exciton - a neutral quasiparticle formed by bound states of electrons and holes. Usual excitons, however, are always bosons with integer spin and thus cannot represent Majorana fermions. Where then should we look for half-integer particles that are their own antiparticles?

At first sight it seems hopeless to realize Majorana fermions in ordinary materials, e.g. metals, since electrons are charged and definitely different from their 'antiparticles', the holes. Superconductivity, on the other hand, can change this picture because in superconductors electrons form so-called Cooper pairs, which are composite bosons. This means that their wave functions are symmetric under particle interchange and they are allowed to be in the same state, i.e., they can 'condense' into the same ground quantum state (22–24). As a consequence, charge conservation is violated: electrons in Cooper pairs can be added or subtracted from the condensate without substantially changing its properties. In addition, superconductors screen electric and confine magnetic fields so that charge is no longer observable.

The most common type of superconducting pairing is called s-wave symmetry, in which electrons carry opposite spins (singlet). In second quantization, the quasiparticle (Bogoliubov quasiparticles) operators have the form $d = uc_{\uparrow}^{\dagger} + vc_{\downarrow}$, where c_{σ} annihilates (creates) an electron (a hole) with spin projection $\sigma =\uparrow,\downarrow$. Hence if superconductors indeed harbor Majoranas fermions, it means that the associated quasiparticle annihilation operator has to have the form $\gamma = uc_{\sigma}^{\dagger} + u^{*}c_{\sigma}$, which is Hermitian and thus leads to $\gamma = \gamma^{\dagger}$. Note that the previous definition suggests that the fermion operators composing the Majoranas are 'spinless', in other words, that only electrons with the same spin can pair up. There are currently two ways of getting around the spin-quantum number issue: (i) systems that naturally have spin-triplet pairing (electrons with the same spin) or (ii) systems in which superconductivity coexists with spin-orbit interaction or some other mechanism that breaks spin conservation. In the first context, Majoranas were predicted to occur as quasiparticles in a fractional quantum Hall state of a two-dimensional electron gas with filling $\nu = 5/2$ (25) and in vortices or, as we shall see later on, at the edges of p-wave superconductors, e.g. in so-called half-vortex states of the superconductor Sr_2RuO_4 (26). The experimental status of both proposals though is still unresolved (20). However as has been shown (27), the existence of Majorana fermions is a "topological invariant", which guarantees that they will exist in any system with the same topological properties as a p-wave superconductor.

Following this "topological idea", solution (ii) was first theoretically implemented by Fu and Kane in Ref. (28), in which they show that the proximity effect between an ordinary s-wave superconductor and a 3D topological insulator (29) leads to the presence of Majorana bound states at vortices formed at the two-dimensional surface of topological insulators. In 2010 Sau et al. (30) showed that a conventional 2D semiconductor should work just as well, provided it has a strong spin-orbit coupling and is subjected to a magnetic field. In that same year, two other works (31, 32) predicted that given a magnetic field parallel to an InAs or InSb nanowire in proximity to an s-wave superconductor, a pair of Majorana modes would appear at the opposite ends of the wire. Due to the proximity between the two materials, Cooper pairs leak through the interface into the wire, which then inherits the superconductivity. In addition, the spin-orbit coupling together with the magnetic field allow an effectively spinless (p-wave superconductivity) regime to be reached. Note that in p-wave superconductors, the quasi-particles satisfy particle-hole symmetry $\gamma^\dagger(E) = \gamma(-E)$, consequently, the Majorana modes obeying $\gamma^\dagger = \gamma$ should have zero energy.

Other several proposals were made in order to observe the emergence of Majorana fermions in condensed matter systems, e.g., on the interface between a ferromagnet and a superconductor deposited on a 2D topological insulator (33–35), in cold atomic gases (36–38), in carbon nanotubes (39–41), just to name a few.

The 1D nanowire setup was recently implemented by Kouwenhoven's group (1), followed by many other observations that can be interpreted as Majorana signatures (42–46). In Kouwenhoven's group experiment an InSb wire is connected to a normal-metal gold electrode on one side of the circuit and to a superconducting NbTiN electrode on the other. A gate voltage applied to the system acts as a knob allowing the experimentalists to tune the Fermi energy of the wire. When a bias voltage is applied between the normal metal and the superconductor, they measure the conductance of the system. Ordinary electrons cannot tunnel into the superconducting gap but if a Majorana resides there [see Fig. 1.3 (a)], the electron can tunnel into that

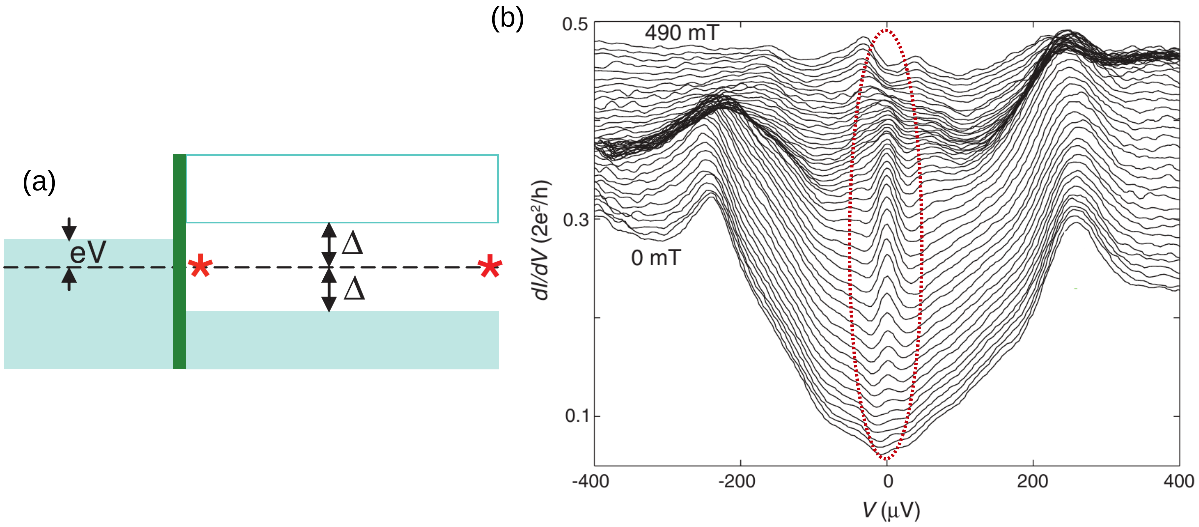

Figure 1.3 – Sketch of the energy states (a). The green rectangle indicates the tunnel barrier separating the normal part of the nanowire on the left from the wire section with induced superconducting gap Δ. An external voltage V is applied between the normal and the superconductor. The red stars illustrate the locations of the Majorana pair. (b) Differential conductance as a function of the applied bias voltage for various values of magnetic field. The dashed red line emphasizes the zero-energy peak. Figure taken from Ref. (1).

state and a peak in the conductance should be seen. What was observed is shown in Fig. 1.3 (b). In agreement with the theory, at a given value of the magnetic field a peak in the conductance emerges when the bias voltage is tuned to zero. As can be seen in the figure, this peak persists for a wide range of magnetic field intensities and gate voltages.

Although this might seem a clear evidence for a Majorana zero mode, researchers started wondering whether what experimentalists were seeing indeed represents the Majorana physics. This is so because zero bias peaks also arise from other phenomena, e.g., the Kondo effect, Andreev bound states and antilocalization (47–49). It is in this context that our study fits in. As we shall see in the following, the setup nanowire+spin-orbit coupling+magnetic field+s-wave superconductivity can be mapped onto the so-called Kitaev model (50), which we use to represent the superconducting nanowire in our system. Next we summarize some of the Majorana fermion properties.

1.1.1 Majorana fermion properties

Let us denote γ the annihilation operator of a Majorana fermion. As we have already mentioned, since Majoranas have the property of being their own antiparticle it follows that $\gamma^\dagger = \gamma$.

In addition, acting this operator on a given state twice is the same as creating and destroying a Majorana mode leaving the system unchanged, which leads to $\gamma^2 = 1$. We emphasize that strictly speaking Majoranas do not represent particles, rather they can be viewed as 'half' regular fermions, whose operators can be written as

$$f = \frac{1}{2}\left(\gamma_A + i\gamma_B\right) \quad \text{and} \quad f^{\dagger} = \frac{1}{2}\left(\gamma_A - i\gamma_B\right). \tag{1.4}$$

From the anti-commutation relations obeyed by f and using $\gamma^2 = 1$, we obtain

$$\left\{\gamma_i, \gamma_j\right\} = 2\delta_{i,j}. \tag{1.5}$$

In principle, any ordinary fermionic operator can be written in terms of Majoranas. This constitutes simply a mathematical operation without physical consequences, however, f remains unusual in two respects. First, as we will show later on, the Majoranas γ_A and γ_B can arbitrarily localize far apart from each other, e.g., at the two ends of the 1D nanowire, hence f constitutes a non-local operator. Second, as we have already mentioned, these Majorana modes have zero-energy, which implies that f can empty or full a non-local state with no energy cost, resulting in a ground-state degeneracy. A consequence of these properties is the emergence of non-Abelian statistics (51). It is in this peculiarity that lies the major interest in observing Majorana fermions in the condensed matter scenario.

The non-local state present in the system is protected from most types of decoherence, since local perturbations can only affect one of the Majoranas. Due to their non-Abelian statistics, the state can be manipulated by physical exchange of the Majoranas, which can potentially be applied to topological quantum computation (51, 52).

In a few words, non-Abelian statistics means that particle exchanges are non-trivial operations which generally do not commute. We know that fermions and bosons follow the Fermi-Dirac and Bose-Einstein statistics, respectively. This means that by exchanging two fermions (bosons) the many-body wavefunction of the system acquires a phase -1 (1). In 2D systems, however, the particles known as anyons obey a different statistics: Abelian or non-Abelian, neither fermionic nor bosonic (53, 54). By exchanging Abelian anyons, the wavefunction gains a phase $e^{i\theta}$ intermediate between 1 and -1. The exchange of non-Abelian anyons does not simply lead to a phase factor in the wavefunction, but rather can change to a different quantum state.

As we have mentioned, perhaps the simplest way of detecting the presence of a Majorana bound state in a superconductor-nanowire system is through transport measurements. However, an unambiguous way of proving their existence is to verify the braiding statistics property via some interference experiment (55). As we shall see in Chapter 4, we claim that our results provide a clear proof of the presence of the zero mode bound at the end of the nanowire (56).

1.2 Outline of this thesis

As briefly outlined above, the focus of this thesis is the study of transport properties of two different systems: (i) a ferromagnetic STM tip connected to an atom adsorbed on a nonmagnetic surface and (ii) a superconducting nanowire modeled by the Kitaev chain and side-coupled to a dot connected to source and drain leads. To both we apply the Green's functions formalism, the nonequilibrium approach to the STM system and the equilibrium to the Majorana setup.

In Chapter 2 we present a detailed description of the formulation in terms of nonequilibrium Green's functions used to calculate the spin-resolved currents and the spin population in the adatom in the system STM tip+adatom+surface. We first determine the current and density of states of the subsystem adatom+surface in the particular case when the coupling to the tip can be neglected, i.e., the tip acts as a probe. We find oscillations in the density of states (Friedel oscillations) similar to those observed in a system containing an impurity on the surface of a metal. The numerical calculation is performed within a self-consistent approach due to the presence of the Coulomb interaction. We then compute the adatom occupation and the spin-resolved currents when the tip-adatom coupling is relevant. We plot the currents and occupations as functions of the lateral distance between the tip and the adatom and observe the emergence of a spatially resolved spin-diode effect, that is, polarized current when the ferromagnetic tip acts as the source and the nonmagnetic surface as the drain of electrons and for the opposite case, unpolarized current. This rectification of the current occurs only when the adatom is singly occupied and arises from the interplay between the Coulomb interaction and the spin-dependent tunneling rates. We also observe spin-dependent Friedel oscillations in the currents, a direct result due to the presence of the adatom on the surface. In the doubly occupied regime we show that the current is unpolarized in both cases.

Chapter 3 is devoted to the Majorana fermions. We review and summarize their properties and describe in detail the mapping of the Kitaev model onto the system semiconducting nanowire+spin-orbit+s-wave superconductivity+magnetic field into the Kitaev chain we use to represent our superconducting nanowire.

In Chapter 4 we show our results for the system semiconducting-nanowire, side-coupled to a dot connected to leads. We detail the equilibrium recursive Green's functions approach we use to determine the conductance of the system and the local density of states of the dot and of the sites in the chain. We propose a direct way of probing the Majorana end mode in the chain by measuring the two-terminal conductance through the side-coupled dot. We show that the Majorana end mode of the wire leaks into the dot thus giving rise to a Majorana resonance in the dot. Surprisingly, we find that this dot Majorana mode is pinned to the Fermi level of the leads even when the gate controlled dot level is far off resonance. We then suggest three experimental ways of probing the Majorana end mode in the wire via the leaked/pinned Majorana mode in the dot: (i) with the dot kept off resonance we plot the conductance G vs the wire-dot coupling, which can be controlled by an external gate, and see the emergence of a $e^2/2h$ peak in G as the Majorana end mode "leaks" into the dot; (ii) Alternatively, we plot G vs the gate voltage V_g over a range in which the energy level of the dot runs from far below to far above the Fermi-level of the leads. We find G to be essentially a plateau at $e^2/2h$, different from the conductance obtained when a normal electron mode is coupled to the dot; (iii) We drive the wire through a non-topological/topological phase transition by varying the chemical potential μ of the wire. We calculate the conductance of the dot as a function of μ and show that the presence/absence of the Majorana end mode in the wire drastically alter the conductance of the dot. Although our system is non-interacting and we do not treat the Kondo problem, we claim that our findings could be used as a means of unambiguously distinguishing Majorana zero-mode peaks from those of the Kondo effect.

Finally, in Chapter 5 we summarize our results and present some perspectives for future work.

Chapter 2

Ferromagnetic STM tip operating as a spin-diode

In this chapter, we investigate spin-polarized transport in a system composed of a ferromagnetic Scanning Tunneling Microscope (STM) tip coupled to an adsorbed atom (adatom) on a host surface. Electrons can tunnel directly from the tip to the surface or via the adatom. Since the tip is ferromagnetic and the host surface (metal or semiconductor) is non-magnetic we can observe a spin-diode effect (9) when the adatom is in the regime of single occupancy. This effect leads to an unpolarized current for direct bias ($V > 0$) and polarized current for reverse ($V < 0$) bias voltages, if the tip is nearby the adatom. We use the nonequilibrium Keldysh technique to derive the spin-polarized current in the system and analyze the interplay between the lateral displacement of the tip and the intra adatom Coulomb interaction on the spin-diode effect. As the tip moves away from the adatom the spin-diode effect vanishes and the currents become polarized for both $V > 0$ and $V < 0$. We also show that there is an imbalance between the up and down spin populations in the adatom, which can be tuned by the tip position and the bias. As we shall see, due to the presence of the adatom, we observe spin-resolved Friedel oscillations in the current, which reflects the oscillations in the calculated local density of states of the subsystem surface+adatom.

2.1 Description of the system

Let us first describe our system. It is composed of a FM-STM tip over an adatom, which can be viewed as a quantum dot, on a host surface, Fig.2.1. Electrons can tunnel from the tip to the substrate or vice-versa via two possible ways: (i) direct tunneling tip-to-surface or (ii) tunneling via the localized state of the adatom. The system is modeled by the Hamiltonian

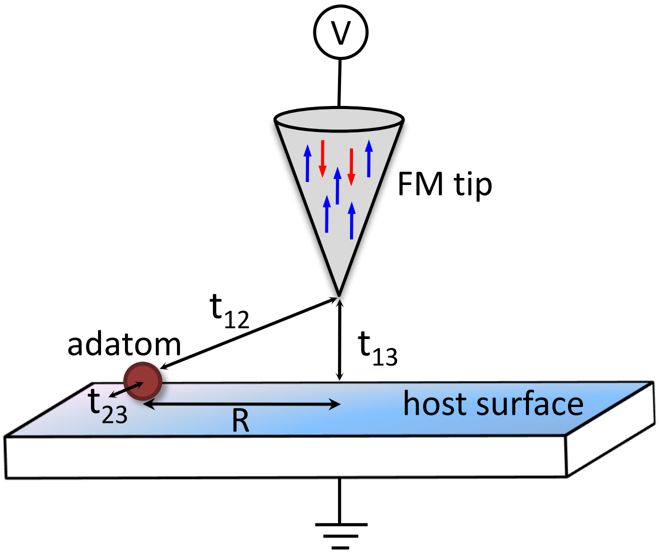

Figure 2.1 – Ferromagnetic Scanning Tunneling Microscope (FM-STM) tip coupled to a host surface with an adatom. The matrix elements t_{12}, t_{13} and t_{23} represent the couplings tip-adatom, tip-surface and adatom-surface, respectively. The tip-adatom lateral distance is denoted by R.

$$H = H_1 + H_2 + H_3 + H_{12} + H_{13} + H_{23}, \tag{2.1}$$

in which H_i corresponds to the tip ($i = 1$), the adatom ($i = 2$) or the surface ($i = 3$), and reads

$$H_i = \sum_{\mathbf{k}_i\sigma} \varepsilon_{\mathbf{k}_i\sigma} c^\dagger_{\mathbf{k}_i\sigma} c_{\mathbf{k}_i\sigma} + \delta_{i2} U \hat{n}_\uparrow \hat{n}_\downarrow, \tag{2.2}$$

where for $i = 1(3)$, $\mathbf{k}_i$ is the wave number for electrons in the tip (host) and the label σ stands for the electron spin components $\uparrow$ and $\downarrow$. Here $\varepsilon_{\mathbf{k}_i\sigma}$ is the energy of the state $\mathbf{k}_i\sigma$ and $c_{\mathbf{k}_i\sigma}$ ($c^\dagger_{\mathbf{k}_i\sigma}$) annihilates (creates) an electron in the quantum state $\mathbf{k}_i\sigma$. We consider a Stoner-like ferromagnetic dispersion $\varepsilon_{\mathbf{k}_1\sigma} = \hbar^2 k_1^2/2m + \sigma\Delta$ for the tip, with m the free electron mass and Δ the usual Stoner parameter (57, 58), and a free electron dispersion $\varepsilon_{\mathbf{k}_3} = \hbar^2 k_3^2/2m$ for the surface. For the adatom, $i = 2$, we consider only a single spin-degenerate energy level, $\varepsilon_{\mathbf{k}_2\sigma} = \varepsilon_\sigma$. In this case the index $\mathbf{k}_2$ simply denotes the adatom level. The second term in H_2 accounts for the Coulomb interaction U.

The coupling terms in Eq. (2.1) can be written as

$$H_{ij} = \sum_{\mathbf{k}_i \mathbf{k}_j \sigma} (t_{ij} c^{\dagger}_{\mathbf{k}_i \sigma} c_{\mathbf{k}_j \sigma} + t^*_{ij} c^{\dagger}_{\mathbf{k}_j \sigma} c_{\mathbf{k}_i \sigma}), \tag{2.3}$$

where t_{ij} is the coupling parameter between subsystems i and j; t_{12}, t_{13} and t_{23} account for the tunnelings tip-adatom, tip-surface and adatom-surface, respectively. When a bias voltage is applied these transfer terms drive the system out of equilibrium.

In the following, we use a real space formulation to calculate the spin-resolved current of the system. This is particularly convenient since we are interested in looking at Friedel oscillations on the surface. As we shall see later on, this formulation is equivalent to a formulation in the **k** space.

2.2 Non-resonant transport

For simplicity let us first consider the transport regime in which the direct coupling between the tip and the adatom is negligible (non-resonant transport), which is valid for large enough tip-adatom lateral distances. The Hamiltonian of the system in this case reduces to

$$H = H_1 + H_2 + H_3 + H_{13} + H_{23}. \tag{2.4}$$

The electrical current for spin σ between the tip and the surface can be calculated from the definition (59)

$$I_1^{\sigma} = -e\langle \dot{N}_1^{\sigma} \rangle = -ie\langle [H, N_1^{\sigma}] \rangle, \tag{2.5}$$

with e the electron charge ($e > 0$) and N_1^{σ} the total number operator given by

$$N_1^{\sigma} = \int d\mathbf{r}_1 \Psi_1^{\sigma^{\dagger}}(\mathbf{r}_1, t) \Psi_1^{\sigma}(\mathbf{r}_1, t), \tag{2.6}$$

where $\Psi_1^{\sigma}(\mathbf{r}_1, t)$ and $\Psi_1^{\sigma^{\dagger}}(\mathbf{r}_1, t)$ are quantum field operators for the electrons in the tip. In Eq. (2.5) and throughout this chapter we assume $\hbar = 1$.

The quantity $\langle O(t) \rangle$ defines the nonequilibrium average value of a physical observable denoted by the operator $O(t)$, and is given by (59, 60)

$$\langle O(t)\rangle = \mathrm{Tr}[\rho O(t)], \tag{2.7}$$

where ρ is the thermal equilibrium density matrix $\rho = (\mathrm{Tr}e^{-\beta H_0})^{-1}e^{-\beta H_0}$, H_0 the Hamiltonian containing only the H_i terms in Eq. (2.4) and $O(t)$ is an operator in the Heisenberg picture, i.e., its time-dependence is governed by the full Hamiltonian of Eq. (2.4).

The only non-vanishing term in the commutator of Eq. (2.5) is $[H_{13}, N_1^\sigma]$. For electrons with spin σ, the tip-surface coupling can be written as (61)

$$H_{13} = \sum_\sigma \int\int d\mathbf{r}_1 d\mathbf{r}_3 [T(\mathbf{r}_1,\mathbf{r}_3)\Psi_1^{\sigma^\dagger}(\mathbf{r}_1,t)\Psi_3^\sigma(\mathbf{r}_3,t) + h.c.], \tag{2.8}$$

in which $T(\mathbf{r}_1,\mathbf{r}_3)$ is a matrix element that accounts for the coupling between the tip and the surface and $\Psi_3^\sigma(\mathbf{r}_3,t)$ is the quantum field operator for electrons in the surface. Calculating $[H_{13}, N_1^\sigma]$ and using the result in Eq. (2.5) we find

$$\begin{aligned} I_1^\sigma &= ie\int\int d\mathbf{r}_1 d\mathbf{r}_3 [T(\mathbf{r}_1,\mathbf{r}_3)\langle\Psi_1^{\sigma^\dagger}(\mathbf{r}_1,t)\Psi_3^\sigma(\mathbf{r}_3,t)\rangle - \\ &\qquad T^*(\mathbf{r}_1,\mathbf{r}_3)\langle\Psi_3^{\sigma^\dagger}(\mathbf{r}_3,t)\Psi_1^\sigma(\mathbf{r}_1,t)\rangle]. \end{aligned} \tag{2.9}$$

Let us define the lesser Green's function,

$$G_\sigma^<(\mathbf{r}_3,t_3;\mathbf{r}_1,t_1) = i\langle\Psi_1^{\sigma^\dagger}(\mathbf{r}_1,t_1)\Psi_3^\sigma(\mathbf{r}_3,t_3)\rangle, \tag{2.10}$$

in terms of which the current can be rewritten as

$$I_1^\sigma = 2e\mathrm{Re}\left\{\int\int d\mathbf{r}_1 d\mathbf{r}_3 T(\mathbf{r}_1,\mathbf{r}_3)G_\sigma^<(\mathbf{r}_3,t;\mathbf{r}_1,t)\right\}. \tag{2.11}$$

The challenge now is to determine $G_\sigma^<(\mathbf{r}_3,t;\mathbf{r}_1,t)$. To this end, we use the nonequilibrium Keldysh formalism[1] (59, 60, 62, 63).

Similarly to the equilibrium case, here we introduce an ordered Green's function

$$G_\sigma(\mathbf{r}_3,\tau_3;\mathbf{r}_1,\tau_1) = -i\langle T_C\Psi_3^\sigma(\mathbf{r}_3,\tau_3)\Psi_1^{\sigma^\dagger}(\mathbf{r}_1,\tau_1)\rangle, \tag{2.12}$$

---

[1] Reference (62), a previous work done in our group, contains all the details of the Keldysh formalism.

with the τ's defined, however, on a contour C in the complex plane. The operator T_C, called contour-ordering operator, orders the operators according to the position of their time arguments on the contour. From the contour-ordered Green's function we can obtain the lesser $G^<_\sigma$, greater $G^>_\sigma$, retarded G^r_σ and advanced G^a_σ Green's functions, which are directly linked to the observables.

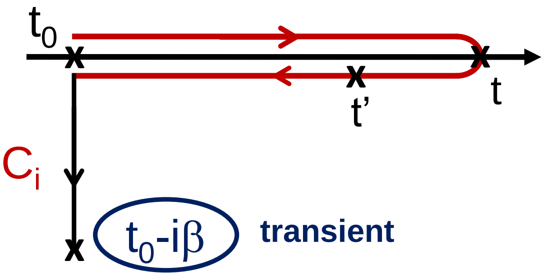

Figure 2.2 – Illustration of the time contour used in the definition of the contour-ordered Green's functions. The transient branch $t_0 - i\beta$ can be neglected in our study since we are only interested in the steady state current.

To determine $G^<_\sigma$, $G^>_\sigma$, G^r_σ and G^a_σ, we use the equation of motion technique. Calculating the equation of motion for the Green's function in Eq. (2.12) we obtain

$$\left(i\frac{\partial}{\partial\tau_1}-\frac{\nabla^2}{2m}\right)G_\sigma(\mathbf{r}_3,\tau_3;\mathbf{r}_1,\tau_1) = -\int d\mathbf{r}'_3 T(\mathbf{r}'_3,\mathbf{r}_1)G_\sigma(\mathbf{r}_3,\tau_3;\mathbf{r}'_3,\tau'_3), \tag{2.13}$$

or in the integral form

$$G_\sigma(\mathbf{r}_3,\tau_3;\mathbf{r}_1,\tau_1) = \int\int d\mathbf{r}'_1 d\mathbf{r}'_3 \int_C d\tilde{\tau} G_\sigma(\mathbf{r}_3,\tau_3;\mathbf{r}'_3,\tilde{\tau})T(\mathbf{r}'_3,\mathbf{r}'_1)g_\sigma(\mathbf{r}'_1,\tilde{\tau};\mathbf{r}_1,\tau_1), \tag{2.14}$$

where g_σ is the free-electron Green's function of the tip and the time integral is over the contour C. The next step is to perform an appropriate analytical continuation. This procedure consists essentially in replacing the contour integral over τ in Eq. (2.13) by a real time integral over t. Here we follow the Langreth procedure (64). For the lesser Green's function $G^<_\sigma$ we have

$$\begin{aligned} G^<_\sigma(\mathbf{r}_3,t_3;\mathbf{r}_1,t_1) &= \int\int d\mathbf{r}'_1 d\mathbf{r}'_3 \int d\tilde{t} \left[G^r_\sigma(\mathbf{r}_3,t_3;\mathbf{r}'_3,\tilde{t})T(\mathbf{r}'_3,\mathbf{r}'_1)g^<_\sigma(\mathbf{r}'_1,\tilde{t};\mathbf{r}_1,t_1)\right. \\ &+ \left. G^<_\sigma(\mathbf{r}_3,t_3;\mathbf{r}'_3,\tilde{t})T(\mathbf{r}'_3,\mathbf{r}'_1)g^a_\sigma(\mathbf{r}'_1,\tilde{t};\mathbf{r}_1,t_1)\right]. \end{aligned} \tag{2.15}$$

In the above equation g^a_σ and $g^<_\sigma$ correspond to the analytically continued free-electron advanced and lesser Green's functions of the tip, respectively. Here we use lower case to denote the free-electron Green's functions of the tip, the adatom and the surface. We note that $G^<_\sigma(\mathbf{r}_3,t_3;\mathbf{r}_1,t_1)$ is coupled to $G^r_\sigma(\mathbf{r}_3,t_3;\mathbf{r}'_3,\tilde{t})$ and also to $G^<_\sigma(\mathbf{r}_3,t_3;\mathbf{r}'_3,\tilde{t})$. To completely determine $G^<_\sigma(\mathbf{r}_3,t_3;\mathbf{r}_1,t_1)$ we then need to perform an iterative process and obtain a system of equations for the Green's functions G^r_σ and $G^<_\sigma$.

Substituting Eq. (2.15) into Eq. (2.11) we obtain

$$\begin{aligned} I_1^\sigma &= 2e\mathrm{Re}\Bigg\{\int\int\int\int\int d\mathbf{r}_1 d\mathbf{r}_3 d\mathbf{r}'_1 d\mathbf{r}'_3 d\tilde{t}\, T(\mathbf{r}_1,\mathbf{r}_3)T(\mathbf{r}'_3,\mathbf{r}'_1)\left[G^r_\sigma(\mathbf{r}_3,t;\mathbf{r}'_3,\tilde{t})g^<_\sigma(\mathbf{r}'_1,\tilde{t};\mathbf{r}_1,t)\right. \\ &+ \left. G^<_\sigma(\mathbf{r}_3,t;\mathbf{r}'_3,\tilde{t})g^a_\sigma(\mathbf{r}'_1,\tilde{t};\mathbf{r}_1,t)\right]\Bigg\}. \end{aligned} \tag{2.16}$$

Performing a Fourier transform in the time coordinate we find

$$\begin{aligned} I_1^\sigma &= 2e\int\frac{d\omega}{2\pi}\mathrm{Re}\Bigg\{\int\int\int\int d\mathbf{r}_1 d\mathbf{r}_3 d\mathbf{r}'_1 d\mathbf{r}'_3 T(\mathbf{r}_1,\mathbf{r}_3)T(\mathbf{r}'_3,\mathbf{r}'_1)[G^r_\sigma(\mathbf{r}_3,\mathbf{r}'_3,\omega)g^<_\sigma(\mathbf{r}'_1,\mathbf{r}_1,\omega) \\ &+ G^<_\sigma(\mathbf{r}_3,\mathbf{r}'_3,\omega)g^a_\sigma(\mathbf{r}'_1,\mathbf{r}_1,\omega)]\Bigg\}. \end{aligned} \tag{2.17}$$

Additionally, Fourier transforming $g^<_\sigma$ and g^a_σ results in

$$\begin{aligned} I_1^\sigma &= 2e\int\frac{d\omega}{2\pi}\mathrm{Re}\Bigg\{\sum_{\mathbf{k}_1}\int\int\int\int d\mathbf{r}_1 d\mathbf{r}_3 d\mathbf{r}'_1 d\mathbf{r}'_3 e^{-i\mathbf{k}_1\cdot\mathbf{r}_1}T(\mathbf{r}_1,\mathbf{r}_3)e^{i\mathbf{k}_1\cdot\mathbf{r}'_1}T(\mathbf{r}'_3,\mathbf{r}'_1)\times \\ &\quad [G^r_\sigma(\mathbf{r}_3,\mathbf{r}'_3,\omega)g^<_{\mathbf{k}_1\sigma}(\omega)+G^<_\sigma(\mathbf{r}_3,\mathbf{r}'_3,\omega)g^a_{\mathbf{k}_1\sigma}(\omega)]\Bigg\}. \end{aligned} \tag{2.18}$$

Now we assume that the coupling between the tip and the surface is local (61, 65) (point source), i.e., $T(\mathbf{r}_1,\mathbf{r}_3)=T^0(\mathbf{r}_1)\delta(\mathbf{r}_3-\mathbf{R})$, $T^0(\mathbf{r}_1)$ being a proportionality factor and $\mathbf{R}$ the tip-adatom lateral distance. Integrating over the surface coordinates we find

$$\begin{aligned} I_1^\sigma &= 2e\int\frac{d\omega}{2\pi}\mathrm{Re}\Bigg\{\sum_{\mathbf{k}_1}\int\int d\mathbf{r}_1 d\mathbf{r}'_1 e^{-i\mathbf{k}_1\cdot\mathbf{r}_1}T^0(\mathbf{r}_1)e^{i\mathbf{k}_1\cdot\mathbf{r}'_1}T^{0^*}(\mathbf{r}'_1)[G^r_\sigma(\mathbf{R},\mathbf{R},\omega)g^<_{\mathbf{k}_1\sigma}(\omega) \\ &+ G^<_\sigma(\mathbf{R},\mathbf{R},\omega)g^a_{\mathbf{k}_1\sigma}(\omega)]\Bigg\}, \end{aligned} \tag{2.19}$$

and then over $\mathbf{r}_1$ and $\mathbf{r}_1'$ we arrive at

$$I_1^\sigma = 2e\int \frac{d\omega}{2\pi}\mathrm{Re}\left\{\sum_{\mathbf{k}_1} |t^0_{13\mathbf{k_1}}|^2 [G^r_\sigma(\mathbf{R},\mathbf{R},\omega) g^<_{\mathbf{k}_1\sigma}(\omega) + G^<_\sigma(\mathbf{R},\mathbf{R},\omega) g^a_{\mathbf{k}_1\sigma}(\omega)]\right\}, \tag{2.20}$$

where $t^0_{13\mathbf{k_1}}$ is the Fourier transform of $T^0(\mathbf{r}_1)$. It is convenient to perform a Fourier transform on $G^r_\sigma(\mathbf{R},\mathbf{R},\omega)$ and $G^<_\sigma(\mathbf{R},\mathbf{R},\omega)$. This results in

$$I_1^\sigma = 2e\int \frac{d\omega}{2\pi}\mathrm{Re}\left\{\sum_{\mathbf{k}_3,\mathbf{k}_3'}\sum_{\mathbf{k}_1} t_{13\mathbf{k}_1\mathbf{k}_3} t^*_{13\mathbf{k}_1\mathbf{k}_3'} [G^r_{\mathbf{k}_3\mathbf{k}_3',\sigma}(\omega) g^<_{\mathbf{k}_1\sigma}(\omega) + G^<_{\mathbf{k}_3\mathbf{k}_3',\sigma}(\omega) g^a_{\mathbf{k}_1\sigma}(\omega)]\right\}, \tag{2.21}$$

where $t_{13\mathbf{k}_1\mathbf{k}_3} = t^0_{13\mathbf{k}_1} e^{i\mathbf{k}_3\cdot\mathbf{R}}$. The proportionality $t_{13} \propto e^{i\mathbf{k_3}\cdot\mathbf{R}}$ was originally discussed in Ref. (66) and further used in Ref. (67). In what follows we assume $t^0_{13\mathbf{k}_1}$ to be a constant, i.e., independent of $\mathbf{k_1}$. As we have mentioned before, Eq. (2.21) could have been directly derived from the $\mathbf{k}$ space Hamiltonian $H^\sigma_{13} = \sum_{\mathbf{k}_1,\mathbf{k}_3} t_{13} c^\dagger_{\mathbf{k}_1\sigma} c_{\mathbf{k}_3\sigma} + t^*_{13} c^\dagger_{\mathbf{k}_3\sigma} c_{\mathbf{k}_1\sigma}$, with $t_{13} = t^0_{13} e^{i\mathbf{k}_3\cdot\mathbf{R}}$. Observe that this is completely equivalent to the real space Hamiltonian Eq. (2.8), with a point source, $T(\mathbf{r}_1,\mathbf{r}_3) = T^0(\mathbf{r}_1)\delta(\mathbf{r}_3 - \mathbf{R})$.

Next we rewrite the current expression (2.20) in terms of a transmission coefficient (68) similarly to the Landauer equation (69).

2.3 Transmission coefficient calculation

Rewritting equation (2.20) we obtain

$$I_1^\sigma = e\int \frac{d\omega}{2\pi}\left[2\pi |t^0_{13}|^2 \rho_{1\sigma}(\omega)\right] i\left\{G^<_\sigma(\mathbf{R},\mathbf{R},\omega) + f_1(\omega)[G^r_\sigma(\mathbf{R},\mathbf{R},\omega) - G^a_\sigma(\mathbf{R},\mathbf{R},\omega)]\right\},$$

where $f_1(\omega)$ and $\rho_{1\sigma}(\omega) = \sum_{\mathbf{k}_1}\delta(\omega - \varepsilon_{\mathbf{k}_1\sigma})$ are, respectively, the Fermi function and the density of states of the tip. If the tip is weakly coupled to the surface, we can calculate the current in the lowest order of $|t^0_{13}|^2$. This means that the Green's functions $G^r_\sigma(\mathbf{R},\mathbf{R},\omega)$ and $G^<_\sigma(\mathbf{R},\mathbf{R},\omega)$ are assumed tip-decoupled, i.e., here they are local Green's functions for the subsystem adatom-surface only. In other words, the tip behaves as a probe, not affecting the local density of states. This allows us to write the current as

$$I_1^\sigma = e\int \frac{d\omega}{2\pi}\left[f_1(\omega) - f_3(\omega)\right] T_\sigma(\mathbf{R},\omega), \tag{2.22}$$

where $f_3(\omega)$ is the Fermi function of the surface and the transmission coefficient is defined by

$$\begin{aligned} T_\sigma(\mathbf{R},\omega) &= \left[2\pi|t^0_{13}|^2\rho_{1\sigma}(\omega)\right]\left[-2\mathrm{Im}\{G^r_\sigma(\mathbf{R},\mathbf{R},\omega)\}\right] \\ &= \left[2\pi|t^0_{13}|^2\rho_{1\sigma}(\omega)\right]\left[2\pi\rho_\sigma(\mathbf{R},\omega)\right], \end{aligned} \tag{2.23}$$

with $\rho_\sigma(\mathbf{R},\omega) = -\frac{1}{\pi}\mathrm{Im}\{G^r_\sigma(\mathbf{R},\mathbf{R},\omega)\}$ – the local density of states (LDOS). In particular, in the absence of the adatom, the LDOS becomes the unperturbed surface density of states per spin, $\rho_3(\omega) = \sum_{\mathbf{k}_3}\delta(\omega-\varepsilon_{\mathbf{k}_3}) = m/n\pi\hbar^2 = 1/2D = \rho^0_3$, with n the 2D electronic density and D the band half width.

In this case and in the zero temperature limit, the current reads

$$I^\sigma_1 = e2\pi|t^0_{13}|^2\rho_{1\sigma}\rho^0_3 eV, \tag{2.24}$$

where V is the bias voltage.

As we shall see in the next section, in the presence of the adatom, similarly to the case of an impurity on the surface of a metal, the LDOS shows Friedel oscillations; these affect the current that oscillates around the value given by Eq. (2.24). The current plateau given by Eq. (2.24) is valid only for small tip-surface coupling parameter t^0_{13}. If we calculate the Green functions $G^r_\sigma(\mathbf{R},\mathbf{R},\omega)$ and $G^<_\sigma(\mathbf{R},\mathbf{R},\omega)$ accounting for the tip, a small correction arises and Eq. (2.24) becomes

$$I^\sigma_1 = G_\sigma V \tag{2.25}$$

with

$$G_\sigma = \frac{e}{h}\frac{4r}{(1+r)^2}, \tag{2.26}$$

where $r = \pi^2|t^0_{13}|^2\rho_{1\sigma}\rho_3$. This feature was pointed out in Ref. (70). Note that we can regain Eq. (2.24) (now divided by $\hbar$) by expanding the above expression for the current up to second order in the coupling parameter.

2.4 Calculating $\rho_\sigma(\mathbf{R},\omega)$ for the subsystem adatom+surface

To determine the LDOS in the presence of the adatom, we calculate $G^r_\sigma(\mathbf{r}_3,\mathbf{r}'_3,\omega)$ by Fourier transforming $G^r_{\mathbf{k}_3\mathbf{k}'_3,\sigma}(\omega)$,

$$G^r_\sigma(\mathbf{r}_3,\mathbf{r}'_3,\omega)=\sum_{\mathbf{k}_3\mathbf{k}'_3} e^{i\mathbf{k}_3\cdot\mathbf{r}_3}e^{-i\mathbf{k}'_3\cdot\mathbf{r}'_3}G^r_{\mathbf{k}_3\mathbf{k}'_3,\sigma}(\omega), \tag{2.27}$$

assuming there is no tip-to-surface coupling, i.e., considering $H=H_2+H_3+H_{23}$. Following the procedure we described in the previous section – equation of motion + analytical continuation – we obtain

$$G^r_{\mathbf{k}_3\mathbf{k}'_3,\sigma}(\omega) \;=\; \delta_{\mathbf{k}_3,\mathbf{k}'_3}g^r_{\mathbf{k}_3\sigma}(\omega)+\sum_{\mathbf{k}_2\mathbf{k}'_2}|t_{23}|^2 g^r_{\mathbf{k}_3\sigma}(\omega)g^r_{\mathbf{k}'_3\sigma}(\omega)G^r_{\mathbf{k}_2\mathbf{k}'_2,\sigma}(\omega), \tag{2.28}$$

where $g^r_{\mathbf{k}_3\sigma}(\omega)=(\omega-\varepsilon_{k_3}+i\delta)^{-1}$ and $\sum_{\mathbf{k}_2\mathbf{k}'_2}G^r_{\mathbf{k}_2\mathbf{k}'_2,\sigma}(\omega)\equiv G^r_{22\sigma}(\omega)$ is the adatom retarded Green's function. To obtain the equation of motion for $G^r_{\mathbf{k}_3\mathbf{k}'_3,\sigma}(t-t')$, we first perform a time derivative with respect to t; the resulting equation couples $G^r_{\mathbf{k}_3\mathbf{k}'_3,\sigma}(t-t')$ to $G^r_{\mathbf{k}_2\mathbf{k}'_3,\sigma}(t-t')$. By differentiating this second Green function now with respect to t', we find an equation that relates $G^r_{\mathbf{k}_3\mathbf{k}'_3,\sigma}(t-t')$ to the adatom Green function $G^r_{\mathbf{k}_2\mathbf{k}'_2,\sigma}(t-t')$.

Using Eq. (2.28) in Eq. (2.27) we find

$$G^r_\sigma(\mathbf{r}_3,\mathbf{r}'_3,\omega)=\sum_{\mathbf{k}_3}\frac{e^{i\mathbf{k}_3\cdot(\mathbf{r}_3-\mathbf{r}'_3)}}{\omega-\varepsilon_{k_3}+i\delta}+|t_{23}|^2\sum_{\mathbf{k}_3}\frac{e^{i\mathbf{k}_3\cdot\mathbf{r}_3}}{\omega-\varepsilon_{k_3}+i\delta}\sum_{\mathbf{k}'_3}\frac{e^{-i\mathbf{k}'_3\cdot\mathbf{r}'_3}}{\omega-\varepsilon_{k'_3}+i\delta}G^r_{22\sigma}(\omega). \tag{2.29}$$

Let

$$\sum_{\mathbf{k}_3}\frac{e^{i\mathbf{k}_3\cdot\mathbf{r}_3}}{\omega-\varepsilon_{k_3}+i\delta}=R(r_3,\omega)+iI(r_3,\omega), \tag{2.30}$$

where $R(r_3,\omega)$ and $I(r_3,\omega)$ denote the corresponding real and imaginary parts given by

$$R(r_3,\omega)=\rho_3^0\int_{-1}^{1}dx\frac{\frac{\omega}{D}-x}{\left(\frac{\omega}{D}-x\right)^2+\delta^2}J_0\left(k_F r_3\sqrt{1+x}\right), \tag{2.31}$$

and

$$I(r_3,\omega)=-\pi\rho_3^0 J_0\left(k_F r_3\sqrt{1+\frac{\omega}{D}}\right), \tag{2.32}$$

with k_F the Fermi wave number and $J_0(x)$ the Bessel function of the first kind. We can then write the LDOS as

$$\rho_\sigma(R,\omega) = \rho_3^0 \left\{ 1 + \frac{\Gamma_3}{2} J_0^2\left(k_F R \sqrt{1+\frac{\omega}{D}} \right) \left[(1-q^2)\mathrm{Im}G_{22\sigma}^r - 2q\mathrm{Re}G_{22\sigma}^r(\omega) \right] \right\}, \tag{2.33}$$

where $\Gamma_3 = 2\pi |t_{23}|^2 \rho_3^0$ and $q = R(R,\omega)/I(R,\omega)$. In order to determine the transmission coefficient, we only have to calculate the adatom retarded Green's function $G_{22\sigma}^r(\omega)$, obtained here using the Hubbard I approximation. (59) This approximation accounts for the Coulomb interaction and consists in factorizing the higher-order correlation functions appearing in the resulting equation of motion for $G_{22\sigma}^r(\omega)$. As a result we have

$$G_{22\sigma}^r(\omega) = \frac{1}{g_{2\sigma}^{r^{-1}}(\omega) - \Sigma^r(\omega)}, \tag{2.34}$$

with

$$g_{2\sigma}^r(\omega) = \frac{\omega - \varepsilon_\sigma - U(1-n_{\bar\sigma})}{(\omega-\varepsilon_\sigma)(\omega-\varepsilon_\sigma-U)}, \tag{2.35}$$

where $\bar\sigma = -\sigma$, $n_{\bar\sigma}$ is the average occupation and Σ^r is the self energy related to the coupling between the adatom and the host surface, $\Sigma^r = -\frac{i}{2}\Gamma_3$.

2.5 Resonant + non-resonant transport

In this section we determine the *total* current – tip-to-adatom-to-host + tip-to-host – flowing in the system. In addition to the non-resonant (tip-to-host) current, calculated in Section A, here we consider the contribution from the direct tunneling of electrons between the tip and the adatom (resonant current). The corresponding additional term H_{12} is now taken into account and the Hamiltonian describing the system is given by Eq. (2.1). Note that for large enough R distances ($R \to \infty$) we regain the non-resonant case. Here for convenience we perform the calculation in **k** space.

We model the tip-surface, tip-adatom and adatom-surface couplings, respectively, by considering

$$t_{12} = t_{12}^0 e^{-R/R_0}, \tag{2.36}$$

$$t_{13} = t_{13}^0 e^{i\mathbf{k}_3\cdot\mathbf{R}}, \tag{2.37}$$

$$t_{23} = t_{23}^0, \tag{2.38}$$

where t_{12}^0, t_{13}^0 and t_{23}^0 are (constant) phenomenological parameters and R_0 gives the exponential spatial decay for the coupling between the tip and the adatom as the tip moves away from it.

The current flowing into the tip or leaving it can be determined from Eq. (2.5). Calculating the commutator in this equation via Eqs. (2.1)-(2.3) we find

$$\begin{aligned}[][H, N_1^\sigma] &= \sum_{j=2}^{3} [H_{1j}, N_1^\sigma] \\ &= \sum_{j=2}^{3} \sum_{\mathbf{k}_1,\mathbf{k}_j} \left(-t_{1j} c_{\mathbf{k}_1\sigma}^\dagger c_{\mathbf{k}_j\sigma} + t_{1j}^* c_{\mathbf{k}_j\sigma}^\dagger c_{\mathbf{k}_1\sigma} \right).\end{aligned} \tag{2.39}$$

Substituting this result into Eq. (2.5) we obtain

$$I_1^\sigma = -ie \sum_{j=2}^{3} \sum_{\mathbf{k}_1,\mathbf{k}_j} \left\{ -t_{1j} \langle c_{\mathbf{k}_1\sigma}^\dagger c_{\mathbf{k}_j\sigma} \rangle + t_{1j}^* \langle c_{\mathbf{k}_j\sigma}^\dagger c_{\mathbf{k}_1\sigma} \rangle \right\}, \tag{2.40}$$

or in terms of the lesser Green's function $G_{\mathbf{k}_j\mathbf{k}_1,\sigma}^<(t,t)$,

$$I_1^\sigma = 2e\mathrm{Re}\left\{ \sum_{j=2}^{3} \sum_{\mathbf{k}_1,\mathbf{k}_j} t_{1j} G_{\mathbf{k}_j\mathbf{k}_1,\sigma}^<(t,t) \right\}, \tag{2.41}$$

where $G_{\mathbf{k}_j\mathbf{k}_1,\sigma}^<(t,t) = i\langle c_{\mathbf{k}_1\sigma}^\dagger(t) c_{\mathbf{k}_j\sigma}(t)\rangle$. Equation (2.41) is equivalent to Eq. (2.11) when $t_{12} = 0$. Now we must find an expression for the lesser Green's function. Following the procedure described in section 2.2, below we write down the equation of motion for the contour-ordered Green's function $G_{\mathbf{k}_j\mathbf{k}_1,\sigma}(\tau,\tau') = -i\langle T_C c_{\mathbf{k}_j\sigma}(\tau) c_{\mathbf{k}_1\sigma}^\dagger(\tau')\rangle$

$$\left(i\frac{\partial}{\partial\tau'} + \varepsilon_{\mathbf{k}_1} \right) G_{\mathbf{k}_j\mathbf{k}_1,\sigma}(\tau,\tau') = -\sum_{l=2}^{3} \sum_{\mathbf{k}_l} t_{1l}^* G_{\mathbf{k}_j\mathbf{k}_l,\sigma}(\tau,\tau'), \tag{2.42}$$

or in the integral form

$$G_{\mathbf{k}_j\mathbf{k}_1,\sigma}(\tau,\tau') = \sum_{l=2}^{3}\sum_{\mathbf{k}_l} t_{1l}^{*}\int_C d\tau_1 G_{\mathbf{k}_j\mathbf{k}_l,\sigma}(\tau,\tau_1)g_{\mathbf{k}_1\sigma}(\tau_1,\tau'), \tag{2.43}$$

where $g_{\mathbf{k}_1\sigma}(\tau_1,\tau')$ is the tip free-electron Green's function, and then analytically continue Eq. (2.43) to find $G^{<}_{\mathbf{k}_j\mathbf{k}_1,\sigma}(t,t')$. Using this result in Eq. (2.41) we have

$$I_1^{\sigma} = 2e\mathrm{Re}\left\{\sum_{j,l=2}^{3}\sum_{\mathbf{k}_1,\mathbf{k}_j,\mathbf{k}_l} t_{1j}t_{1l}^{*}\int dt_1\left[G^{r}_{\mathbf{k}_j\mathbf{k}_l,\sigma}(t,t_1)g^{<}_{\mathbf{k}_1\sigma}(t_1,t)+G^{<}_{\mathbf{k}_j\mathbf{k}_l,\sigma}(t,t_1)g^{a}_{\mathbf{k}_1\sigma}(t_1,t)\right]\right\}.$$

Taking the Fourier transform of the above expression we find

$$\begin{aligned}
I_1^{\sigma} = 2e\mathrm{Re}\Bigg\{&\int\frac{d\omega}{2\pi}\times\\
&\sum_{\mathbf{k}_1\mathbf{k}_2\mathbf{k}_2'} t_{12}t_{12}^{*}[G^{r}_{\mathbf{k}_2\mathbf{k}_2',\sigma}(\omega)g^{<}_{\mathbf{k}_1\sigma}(\omega)+G^{<}_{\mathbf{k}_2\mathbf{k}_2',\sigma}(\omega)g^{a}_{\mathbf{k}_1\sigma}(\omega)]+\\
&\sum_{\mathbf{k}_1\mathbf{k}_2\mathbf{k}_3} t_{12}t_{13\mathbf{k}_3}^{*}[G^{r}_{\mathbf{k}_2\mathbf{k}_3,\sigma}(\omega)g^{<}_{\mathbf{k}_1\sigma}(\omega)+G_{\mathbf{k}_2\mathbf{k}_3,\sigma}(\omega)^{<}g^{a}_{\mathbf{k}_1\sigma}(\omega)]+\\
&\sum_{\mathbf{k}_1\mathbf{k}_3\mathbf{k}_2} t_{13\mathbf{k}_3}t_{12}^{*}[G^{r}_{\mathbf{k}_2\mathbf{k}_3,\sigma}(\omega)g^{<}_{\mathbf{k}_1\sigma}(\omega)+G^{<}_{\mathbf{k}_3\mathbf{k}_2,\sigma}(\omega)g^{a}_{\mathbf{k}_1\sigma}(\omega)]+\\
&\sum_{\mathbf{k}_1\mathbf{k}_3\mathbf{k}_3'} t_{13\mathbf{k}_3}t_{13\mathbf{k}_3'}^{*}[G^{r}_{\mathbf{k}_3\mathbf{k}_3',\sigma}(\omega)g^{<}_{\mathbf{k}_1\sigma}(\omega)+G^{<}_{\mathbf{k}_3\mathbf{k}_3',\sigma}(\omega)g^{a}_{\mathbf{k}_1\sigma}(\omega)]\Bigg\}.
\end{aligned} \tag{2.44}$$

Using Eqs. (2.36)-(2.37) we can rewrite Eq. (2.44) as

$$\begin{aligned}
I_1^{\sigma} = 2e\mathrm{Re}\Bigg\{\int\frac{d\omega}{2\pi}&|t_{12}^{0}|^2 e^{-2(R/R_0)}[G^{r}_{22\sigma}g^{<}_{1\sigma}+G^{<}_{22\sigma}g^{a}_{1\sigma}]+\\
&t_{12}^{0}t_{13}^{0*}e^{-R/R_0}[G^{r}_{\underline{3}2\sigma}g^{<}_{1\sigma}+G^{<}_{\underline{3}2\sigma}g^{a}_{1\sigma}]+\\
&t_{13}^{0}t_{12}^{0*}e^{-R/R_0}[G^{r}_{2\underline{3}\sigma}g^{<}_{1\sigma}+G^{<}_{2\underline{3}\sigma}g^{a}_{1\sigma}]+\\
&|t_{13}^{0}|^2[G^{r}_{\underline{33}\sigma}g^{<}_{1\sigma}+G^{<}_{\underline{33}\sigma}g^{a}_{1\sigma}]\Bigg\},
\end{aligned} \tag{2.45}$$

where we have introduced the definitions

$$
\begin{aligned}
g^{<,a}_{1\sigma}(\omega) &= \sum_{\mathbf{k}_1} g^{<,a}_{\mathbf{k}_1\sigma}(\omega), \\
G^{<,r}_{\underline{3}2\sigma} &= \sum_{\mathbf{k}_3\mathbf{k}_2} e^{i\mathbf{k}_3\cdot\mathbf{R}} G^{<,r}_{\mathbf{k}_3\mathbf{k}_2,\sigma}, \\
G^{<,r}_{2\underline{3}\sigma} &= \sum_{\mathbf{k}_2\mathbf{k}_3} e^{-i\mathbf{k}_3\cdot\mathbf{R}} G^{<,r}_{\mathbf{k}_2\mathbf{k}_3,\sigma}, \\
G^{<,r}_{\underline{33}\sigma} &= \sum_{\mathbf{k}_3\mathbf{k}'_3} e^{i(\mathbf{k}_3-\mathbf{k}'_3)\cdot\mathbf{R}} G^{<,r}_{\mathbf{k}_3\mathbf{k}'_3,\sigma}.
\end{aligned}
\tag{2.46}
$$

Note that from Eq. (2.44) we regain Eq. (2.21) in the limit $t^0_{12} = 0$, i.e., when the tip is far away from the adatom.

In the following, we rewrite the Green's functions using a matrix representation. As we shall see, in this context it is possible to obtain a Dyson equation.

2.6 Matrix Green's function formulation

We can see from Eq. (2.44) that $G^<_{\mathbf{k}_j\mathbf{k}_1,\sigma}(t,t')$ is coupled to other Green's functions. In order to find these Green's functions, we have to apply the equation of motion technique to the corresponding contour-ordered Green's function for each one of them and then perform an analytical continuation to obtain the respective $G^{<,r}$. After a straightforward calculation we find

$$
G_{\mathbf{k}_i\mathbf{k}_j,\sigma}(\tau,\tau') = \delta_{\mathbf{k}_i\mathbf{k}_j} g_{\mathbf{k}_j\sigma}(\tau,\tau') \sum_{l(l\neq j)} \sum_{\mathbf{k}_l} \int d\tilde{\tau} G_{\mathbf{k}_i,\mathbf{k}_l,\sigma}(\tau,\tilde{\tau}) t^*_{jl} g_{\mathbf{k}_j\sigma}(\tilde{\tau},\tau'), \tag{2.47}
$$

i.e., a system of coupled equations for the Green's functions. Here $g_{\mathbf{k}_j\sigma}(\tau,\tau')$ is the free-electron Green's function of the tip ($j=1$), the adatom ($j=2$) or the host surface ($j=3$). These three Green's functions $g_{\mathbf{k}_j\sigma}(\tau,\tau')$ ($j=1,2,3$) can be easily evaluated. Interestingly, by defining

$$\begin{aligned}
G_{ij\sigma} &= \sum_{\mathbf{k}_i\mathbf{k}_j} G_{\mathbf{k}_i\mathbf{k}_j,\sigma}, && (2.48)\\
G_{\underline{3}j\sigma} &= \sum_{\mathbf{k}_3\mathbf{k}_j} e^{i\mathbf{k}_3\cdot\mathbf{R}} G_{\mathbf{k}_3\mathbf{k}_j,\sigma}, && (2.49)\\
G_{j\underline{3}\sigma} &= \sum_{\mathbf{k}_j\mathbf{k}_3} e^{-i\mathbf{k}_3\cdot\mathbf{R}} G_{\mathbf{k}_j\mathbf{k}_3,\sigma}, && (2.50)\\
G_{\underline{33}\sigma} &= \sum_{\mathbf{k}_3\mathbf{k}'_3} e^{i(\mathbf{k}_3-\mathbf{k}'_3)\cdot\mathbf{R}} G_{\mathbf{k}_3\mathbf{k}'_3,\sigma}, && (2.51)
\end{aligned}$$

where the sum *is not* taken over the spin indices, we can write down a Dyson equation of the form

$$\mathbf{G}_\sigma(\tau,\tau') = \mathbf{g}_\sigma(\tau,\tau') + \int d\tau_1 \mathbf{G}_\sigma(\tau,\tau_1)\Sigma\mathbf{g}_\sigma(\tau_1,\tau'), \tag{2.52}$$

with $\mathbf{G}_\sigma(\tau,\tau')$ being a matrix Green's's function whose elements are defined following Eqs. (2.48)-(2.51), i.e.,

$$\mathbf{G}_\sigma = \begin{pmatrix} G_{11\sigma} & G_{12\sigma} & G_{13\sigma} & G_{1\underline{3}\sigma} \\ G_{21\sigma} & G_{22\sigma} & G_{23\sigma} & G_{2\underline{3}\sigma} \\ G_{31\sigma} & G_{32\sigma} & G_{33\sigma} & G_{3\underline{3}\sigma} \\ G_{\underline{3}1\sigma} & G_{\underline{3}2\sigma} & G_{\underline{3}3\sigma} & G_{\underline{33}\sigma} \end{pmatrix}. \tag{2.53}$$

Additionally the self-energy is given by

$$\Sigma = \begin{pmatrix} 0 & t_{12} & 0 & t^0_{13} \\ t^*_{12} & 0 & t_{23} & 0 \\ 0 & t^*_{23} & 0 & 0 \\ t^{0*}_{13} & 0 & 0 & 0 \end{pmatrix}, \tag{2.54}$$

and

$$\mathbf{g}_\sigma = \begin{pmatrix} g_{1\sigma} & 0 & 0 & 0 \\ 0 & g_{2\sigma} & 0 & 0 \\ 0 & 0 & g_{3\sigma} & g_{\underline{3}^*\sigma} \\ 0 & 0 & g_{\underline{3}\sigma} & g_{3\sigma} \end{pmatrix}, \tag{2.55}$$

with the matrix elements

$$
\begin{aligned}
g_{j\sigma}(\tau,\tau') &= \sum_{\mathbf{k}_j}{}' g_{\mathbf{k}_j\sigma}(\tau,\tau'),\ \ j=1,2,3 && (2.56)\\
g_{\underline{3}\sigma}(\tau,\tau') &= \sum_{\mathbf{k}_3} e^{i\mathbf{k}_3\cdot\mathbf{R}} g_{\mathbf{k}_3\sigma}(\tau,\tau'), && (2.57)\\
g_{\underline{3}^*\sigma}(\tau,\tau') &= \sum_{\mathbf{k}_3} e^{-ik_3\cdot\mathbf{R}} g_{\mathbf{k}_3\sigma}(\tau,\tau'). && (2.58)
\end{aligned}
$$

Note that Eq. (2.28) and the LDOS, given by Eq. (2.33), can be derived from the present matrix formulation by taking $t_{12}=0$ and $t_{13}=0$ in the self-energy matrix [Eq. (2.54)].

Performing an analytic continuation in Eq. (2.52) we obtain the Dyson equation for the retarded Green's function

$$
\mathbf{G}_\sigma^r = [\mathbf{g}_\sigma^{r^{-1}} - \S^r]^{-1}, \tag{2.59}
$$

and the Keldysh (71) equation

$$
\mathbf{G}_\sigma^< = \mathbf{G}_\sigma^r \mathbf{g}_\sigma^{r^{-1}} \mathbf{g}_\sigma^< \mathbf{g}_\sigma^{a^{-1}} \mathbf{G}_\sigma^a, \tag{2.60}
$$

where

$$
\mathbf{g}_\sigma^{r,<} = \begin{pmatrix} g_{1\sigma}^{r,<} & 0 & 0 & 0 \\ 0 & g_{2\sigma}^{r,<} & 0 & 0 \\ 0 & 0 & g_{3\sigma}^{r,<} & g_{\underline{3}^*\sigma}^{r,<} \\ 0 & 0 & g_{\underline{3}\sigma}^{r,<} & g_{3\sigma}^{r,<} \end{pmatrix}. \tag{2.61}
$$

The advanced Green's's function $\mathbf{g}_\sigma^a$ is given by $\mathbf{g}_\sigma^a = [\mathbf{g}_\sigma^r]^*$. From Eqs. (2.59) and (2.60) we see that if $\mathbf{g}_\sigma^r$ and $\mathbf{g}_\sigma^<$ are known we can determine immediately $\mathbf{G}_\sigma^r$ and $\mathbf{G}_\sigma^<$, and so the spin-resolved current, Eq. (2.45). The first nonzero (diagonal) elements ($g_{1\sigma}^<$ and $g_{1\sigma}^r$) in Eq. 2.61 are

$$
\begin{aligned}
g_{1\sigma}^<(\omega) &= \sum_{\mathbf{k}_1} g_{k_1\sigma}^<(\omega) = \sum_{\mathbf{k}_1} 2\pi i f_1(\omega)\delta(\omega-\varepsilon_{\mathbf{k}_1\sigma})\\
&= 2\pi i f_1(\omega)\rho_{1\sigma}(\omega), && (2.62)
\end{aligned}
$$

$$
\begin{aligned}
g_{1\sigma}^r(\omega) &= \sum_{\mathbf{k}_1} g_{k_1\sigma}^r(\omega) = \sum_{\mathbf{k}_1}\left[P\left(\frac{1}{\omega-\varepsilon_{\mathbf{k}_1\sigma}}\right) - i\pi\delta(\omega-\varepsilon_{\mathbf{k}_1\sigma})\right]\\
&= \Lambda_1(\omega) - i\pi\rho_{1\sigma}(\omega), && (2.63)
\end{aligned}
$$

where $f_1(\omega)$ is the tip Fermi distribution function, $\rho_{1\sigma}(\omega)$ is the tip density of states and $\Lambda_1(\omega) = P\sum_{\mathbf{k}_1}\left(\frac{1}{\omega-\varepsilon_{\mathbf{k}_1\sigma}}\right)$, where P stands for the Cauchy Principal Value. The retarded adatom Green's's function $g^r_{2\sigma}(\omega)$ is given by Eq. (2.35). The lesser component can be calculated straightforwardly from the relation $g^<_{2\sigma}(\omega) = in_\sigma A_\sigma(\omega)$, where

$$A_\sigma(\omega) = 2\pi(1-n_{\bar{\sigma}})\delta(\omega-\varepsilon_\sigma) + 2\pi n_{\bar{\sigma}}\delta(\omega-\varepsilon_\sigma-U), \tag{2.64}$$

and n_σ is the average spin-resolved occupation of the adatom. The third diagonal element of $\mathbf{g}^r$ is given by

$$\begin{aligned} g^r_{3\sigma}(\omega) &= \sum_{\mathbf{k}_3} g^r_{k_3\sigma}(\omega) = \sum_{\mathbf{k}_3}\left[P\left(\frac{1}{\omega-\varepsilon_{\mathbf{k}_3}}\right) - i\pi\delta(\omega-\varepsilon_{\mathbf{k}_3})\right] \\ &= \Lambda_3(\omega) - i\pi\rho_3(\omega), \end{aligned} \tag{2.65}$$

where $\rho_3(\omega) = \rho_3^0$ is the 2D density of states of the surface defined at the end of Sec. 2.3, and $\Lambda_3(\omega) = P\sum_{\mathbf{k}_3}\left(\frac{1}{\omega-\varepsilon_{\mathbf{k}_3}}\right)$. For the corresponding lesser Green's function we find

$$g^<_{3\sigma}(\omega) = \sum_{\mathbf{k}_3} g^<_{\mathbf{k}_3\sigma}(\omega) = 2\pi i f_3(\omega)\rho_3^0, \tag{2.66}$$

where $f_3(\omega)$ is the Fermi distribution function of the host surface.

Finally, we should calculate the off-diagonal elements of the matrix $\mathbf{g}_\sigma$. For the retarded Green's function we have

$$\begin{aligned} g^r_{\underline{3}\sigma}(\omega) &= \sum_{\mathbf{k}_3} e^{i\mathbf{k}_3\cdot\mathbf{R}} g^r_{k_3\sigma}(\omega) \\ &= \rho_3^0\int_{-1}^{1} dx \frac{\frac{\omega}{D}-x}{(\frac{\omega}{D}-x)^2+\delta^2} J_0(k_F R\sqrt{1+x}) - \\ &\qquad i\pi\rho_3^0 J_0\left(k_F R\sqrt{1+\frac{\omega}{D}}\right). \end{aligned} \tag{2.67}$$

For the lesser Green's function we find

$$\begin{aligned} g^<_{\underline{3}\sigma}(\omega) &= \sum_{\mathbf{k}_3} e^{i\mathbf{k}_3\cdot\mathbf{R}} g^<_{k_3\sigma}(\omega), \\ &= 2\pi i\rho_3^0 f_3(\omega) J_0\left(k_F R\sqrt{1+\frac{\omega}{D}}\right). \end{aligned} \tag{2.68}$$

The Green's functions $g^r_{\underline{3}^*\sigma}$ and $g^<_{\underline{3}^*\sigma}$ have exactly the same expressions as Eqs. (2.67) and (2.68), respectively.

2.7 Numerical technique

As we have seen, our main task is to determine the current from Eq. (2.45). To this end, we first calculate $\mathbf{G}^r_\sigma$ and $\mathbf{G}^<_\sigma$ from Eqs. (2.59) and (2.60), respectively. Then we substitute the relevant matrix elements in Eq. (2.45). Note that in the presence of the Coulomb interaction, $g^r_{2\sigma}(\omega)$ and $g^<_{2\sigma}(\omega)$ depend on the adatom occupation $n_{\bar{\sigma}}$; so do $\mathbf{G}^r_\sigma$ and $\mathbf{G}^<_\sigma$. This implies a self-consistent calculation, where n_σ is calculated iteratively via

$$n_\sigma = \int \frac{d\omega}{2\pi i} G^<_{22\sigma}(\omega). \tag{2.69}$$

As a matter of simplification we use the wide-band limit for the tip, so the density of states $\rho_{1\sigma}(\omega)$ is taken as constant ρ^0_1 (ρ^0_3 is already a constant), evaluated at the Fermi level. This is a good approximation when $eV, k_BT << D$, where D is the band half width. The ferromagnetism of the tip is introduced via the density of states $\rho_{1\sigma} = \rho^0_1(1 \pm p)$, where p is the tip polarization and the $+$ and $-$ signs apply to spin up and down, respectively (58) Since the characteristic tunneling rate between the tip and the adatom is given by $\Gamma_{1\sigma} = 2\pi|t_{12}|^2\rho_{1\sigma}$, we find $\Gamma_{1\sigma} = 2\pi|t_{12}|^2\rho^0_1(1 \pm p)$, which is the standard phenomenology to account for the ferromagnetism of the electrode (72). Analogously, the tunneling rate between the adatom and the host surface is $\Gamma_3 = 2\pi|t_{23}|^2\rho^0_3 \equiv \Gamma_0$. In our calculation we take $\Gamma_0 = 10\mu\text{eV}$ as the energy scale. All the phenomenological parameters used here are summarized in table 2.1.

Parameter	**Magnitude**
Band half width	$D = 1000\Gamma_0$
Adatom Charging Energy	$U = 30\Gamma_0$
Tip chemical potential	$\mu_1 = -eV/2$
Host chemical potential	$\mu_3 = eV/2$
System temperature	$k_BT = \Gamma_0$
Tip degree of polarization	$p = 0.4$
Decaying factor of t_{12}	$R_0 = 1/k_F$

Table 2.1 – Parameters used in the self-consistent calculation.

Note that in Table 2.1 we define the origin of the energy scale such that $\mu_1 = \mu_3 = \varepsilon_\sigma = 0$ at zero bias, i.e., the adatom energy level is aligned with the chemical potential of the leads in the absence of an applied bias. In order to be consistent with $\Gamma_0 = 2\pi|t_{23}|^2\rho_3^0$ and the value of ρ_3^0 for typical semiconductors, e.g, GaAs, the factor t_{23} is taken as $\Gamma_0/\sqrt{10}$. We assume $t_{13}^0 = 0.01t_{23}^0$ and adopt values for t_{12}^0 and ρ_1^0 consistent with $\Gamma_0 = 2\pi|t_{12}^0|^2\rho_1^0$. Note that for $eV = \pm 30\Gamma_0$ the adatom can be occupied by a single electron since ε_σ is within the conduction window (the energy range between μ_1 and μ_3) and $\varepsilon_\sigma + U$ is without this range. On the other hand for $eV = \pm 150\Gamma_0$ the dot can be doubly occupied since both ε_σ and $\varepsilon_\sigma + U$ lie inside the conduction window. The parameter R_0 controls how fast the coupling t_{12} decays in space when the tip moves away from the adatom. We take it equal to k_F^{-1}. Hereafter k_F^{-1} will be used as a length scale.

2.8 Results

Below we present our results for the singly and doubly occupied regimes.

2.8.1 Single Occupancy

Figure 2.3 shows the adatom occupations against the lateral distance R between the tip and the adatom. We study both forward ($eV = +30\Gamma_0$) and reverse ($eV = -30\Gamma_0$) bias cases. As mentioned before, for $|eV| = 30\Gamma_0$ the adatom cannot be doubly occupied, since $\varepsilon_\sigma + U$ lies above the Fermi energy of the source. For $V > 0$ the host NM surface is the source and the FM tip is the drain of electrons, i.e., the electrons flow from the NM surface (+ adatom) to the tip. For $V < 0$ we have the opposite.

For $R = 0$ and $V > 0$ (solid blue and red lines) we find $n_\uparrow < n_\downarrow$. This is reasonable since spin up electrons tunnel from the adatom into the tip much more easily than the spin down ones, due to the larger spin up density of states, $\rho_{1\sigma} = \rho_1^0(1 \pm p)$ ($p > 0$), which implies $\Gamma_{1\uparrow} > \Gamma_{1\downarrow}$, and gives rise to a larger spin down population. For a constant bias voltage, as the tip moves away from the adatom [see Eq. (2.36)] the tunneling rates $\Gamma_{1\uparrow}$ and $\Gamma_{1\downarrow}$ decrease, but the incoming rates Γ_3 stay the same, this results in an increase of both $n_\uparrow$ and $n_\downarrow$. We note, however, that the spin down population (solid red line) increases more quickly than the spin up one (solid blue

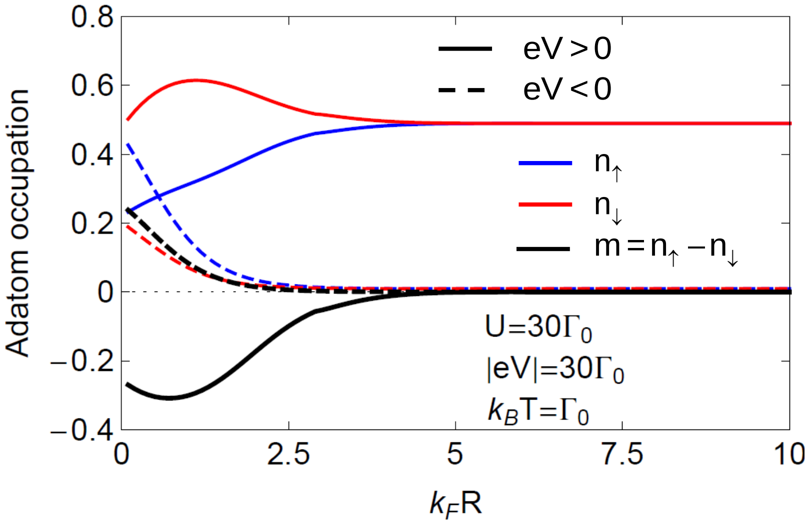

Figure 2.3 – Adatom occupations and magnetization as functions of the lateral tip position R for both forward $eV = 30 < \Gamma_0$ (solid lines) and reverse $eV = -30\Gamma_0$ (dashed lines) bias voltages. The blue and red curves (solid and dashed) represent the spin up and down populations, respectively. The black curves correspond to the magnetization of the system $m = n_\uparrow - n_\downarrow$.

line), this is because $\Gamma_{1\downarrow} < \Gamma_{1\uparrow}$, see Fig. 2.3. As the $n_\uparrow$ adatom population increases with R, the $n_\downarrow$ one tends to be more blocked due to the spin-dependent Coulomb blockade. The interplay between the Coulomb blockade and the decrease of the tunneling rates $\Gamma_{1\uparrow,\downarrow}$ makes $n_\downarrow$ reach a maximum, subsequently decreasing to attain the limit $n_\uparrow = n_\downarrow = 0.5$ for large enough R's.

In contrast, for $eV = -30\Gamma_0$, $n_\uparrow > n_\downarrow$ for small R values, see in Fig. 2.3 the dashed blue and red lines. This is a consequence of $\Gamma_{1\uparrow} > \Gamma_{1\downarrow}$, which means that more spins up tunnel to the adatom. Besides, the outgoing rates Γ_3 (the same for the up and down components) is smaller than $\Gamma_{1\uparrow}$, which results in a larger spin up accumulation in the adatom. As the tip moves away from the adatom, $\Gamma_{1\uparrow}$ and $\Gamma_{1\downarrow}$ go to zero exponentially and the populations $n_\uparrow$ and $n_\downarrow$ are completely drained out into the host surface, thus resulting in an empty adatom.

The magnetization $m = n_\uparrow - n_\downarrow$ is also shown in Fig. 2.3 (solid and dashed black lines). Observe that for small R the adatom is spin down polarized for $V > 0$ and spin up polarized for $V < 0$. As R increases, m tends to zero for both positive and negative bias voltages. However, m tends to zero much slower for $V > 0$ than for $V < 0$, a consequence of the interplay between the Coulomb interaction (spin-Coulomb blockade) and the tunneling rates $\Gamma_{1\sigma}$, that change with the tip position as it moves away from the adatom.

In Fig. 2.4 we present the spin-resolved currents for both $eV = \pm 30\Gamma_0$. The spin-diode effect (9) can be clearly seen for small values of R. While for $V > 0$ (solid lines) we find $I_\uparrow \approx I_\downarrow$

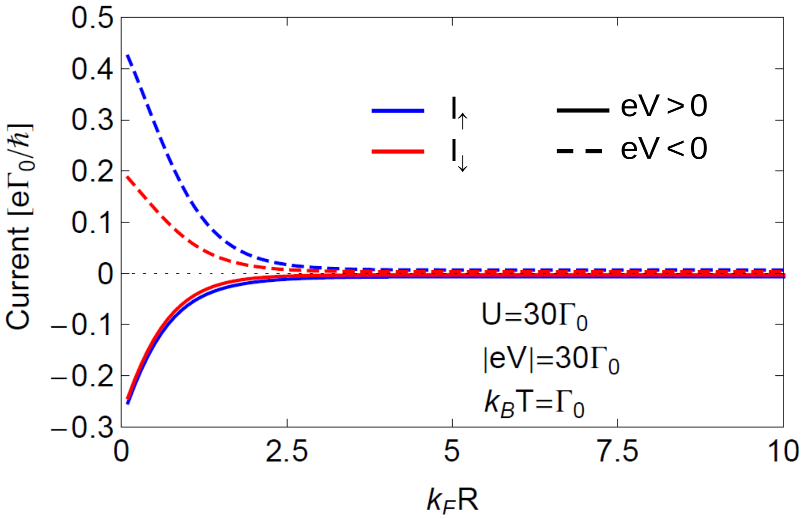

Figure 2.4 – Spin-resolved currents against the tip position R. Both negative (dashed lines) and positive (solid lines) bias voltages are shown. For $|eV| = 30\Gamma_0$ only single occupancy (i.e., $\varepsilon_\sigma + U$ is much higher than the emitter chemical potential) is allowed. This results in the spin-diode effect: for negative bias voltages the current is polarized for all R values while for positive biases the current polarization goes to zero when the tip is close to the adatom.

for small R values, for $V < 0$ (dashed lines) we observe $I_\uparrow > I_\downarrow$. This shows that the current polarization can be controlled via both the bias sign and the tip position. In the case of $V < 0$, we have $\Gamma_{1\uparrow} > \Gamma_3 > \Gamma_{1\downarrow}$, i.e., the spin up population is greater than the spin down one, $m > 0$. As a consequence, in the absence of the Coulomb interaction in the adatom, $I_\uparrow > I_\downarrow$ (the case $U = 0$ resembles the curves in the double occupancy regime ($eV >> U$), see Fig. 2.7. In the presence of U, $I_\downarrow$ is suppressed, since $n_\downarrow$ tends to be more blocked than $n_\uparrow$ (see Fig. 2.6), which results in an enhancement in the difference between $I_\uparrow$ and $I_\downarrow$. For $V > 0$, the magnetization changes sign $m < 0$, now the spin up population tends to be more blocked, and $I_\uparrow$ is more strongly suppressed compared to $I_\downarrow$, interestingly attaining values close to $I_\downarrow$. The amplification of $I_\uparrow$ compared to $I_\downarrow$ for $V < 0$, when the tip is closer to the adatom, does not occur in the double occupancy regime ($eV = \pm 150\Gamma_0$) as we will see in the next section.

In Fig. 2.5 we show the current for a range of R in which only the direct tip-host tunneling (non-resonant transport) is relevant. Note that $I_\uparrow$ and $I_\downarrow$ tend to distinct plateaus for large enough R's. These plateaus correspond to the background current between the tip and the host surface, given approximately by Eq. (2.24). By comparison with Eq. (2.45) we plot in dashed line the current obtained via Eq. (2.22). In the large-R limit, we expect an agreement between both equations, since Eq. (2.22) was derived in the case of negligible tunneling between the tip and the adatom (see the solid black and grey lines). The minor difference between the two

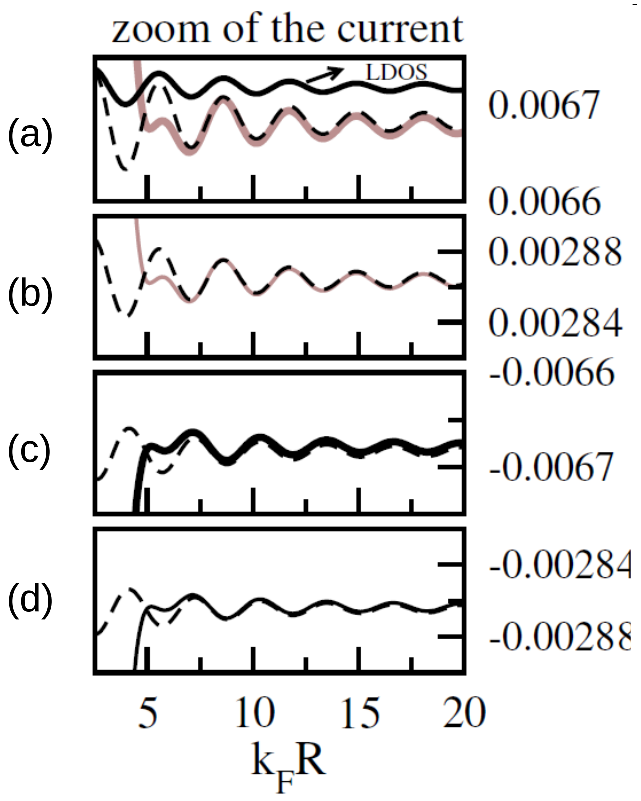

Figure 2.5 – Blow up of the spin-polarized currents for a range of R in which only the direct tip-host tunneling is relevant. The dashed line corresponds to the current obtained via Eq. (2.22). An agreement between the dashed and solid lines should be reached in the large-R limit. (a) Spin-up current (solid gray line) for $V < 0$; the thicker solid line represents the LDOS at the Fermi level. (b) Spin-down current (solid gray line) for $V < 0$. (c) Spin-up current (solid black line) for $V > 0$. (d) Spin-udown current (solid black line) for $V > 0$.

results is due to Eq. (2.22) having been obtained in the limit of small tip-surface coupling parameter t_{13}^{0}. The LDOS evaluated at the Fermi level, $\rho_\sigma(R,0)$, is also shown in Fig. 2.5 (a); it oscillates around the unperturbed surface density of states ρ_3^0. Friedel-like oscillations are seen for both spin components, thus reflecting the oscillations in the LDOS due to the scattering center (adatom). Note that Friedel oscillations have been seen experimentally in a variety of systems. (73–75)

2.8.2 Double Occupancy

Figures 2.6 and 2.7 show the spin-resolved adatom occupations and currents, respectively in the double occupancy regime, i.e., when the bias voltage is large enough ($|eV| = 80\Gamma_0$) to allow for two electrons of opposite spins in the adatom at the same time. For $V > 0$ (black lines), as

R increases both $n_\uparrow$ and $n_\downarrow$ populations tend to unity and the adatom becomes doubly occupied ($n_\uparrow + n_\downarrow = 2$). This is so because electrons can jump into the adatom but cannot leave it for large R values. In contrast, for $V < 0$ both $n_\uparrow$ and $n_\downarrow$ vanish as R increases because the electron source (tip) decouples from the adatom. Observe also that the magnetization m is enhanced as R tends to zero and switches sign depending on whether eV is positive or negative.

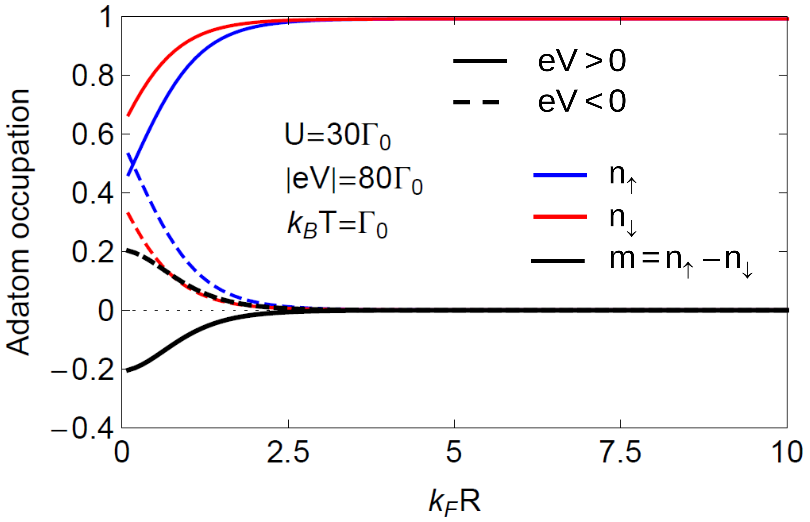

Figure 2.6 – Similar to Fig. 2.3 except that $|eV| = 80\Gamma_0$ here. This bias allows double occupancy of the adatom. For forward voltages (solid lines) the adatom becomes doubly occupied for large R values ($n_\uparrow + n_\downarrow = 2$).

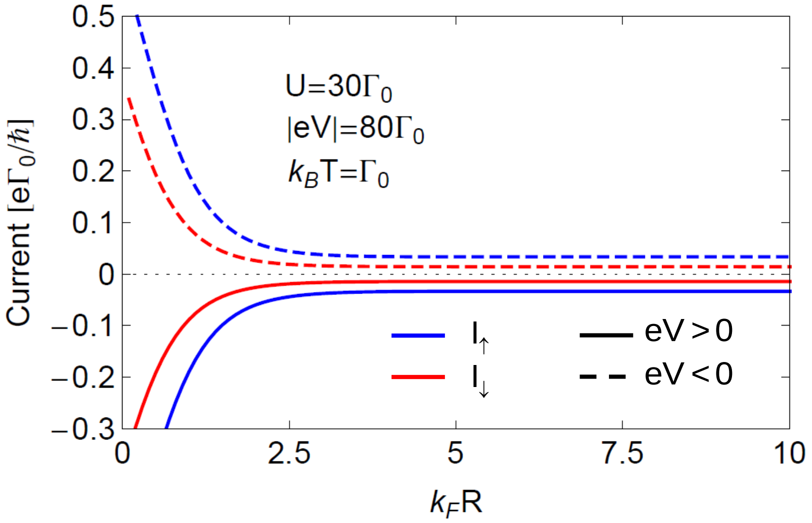

Figure 2.7 – Similar to Fig. 2.4 except that $|eV| = 80\Gamma_0$ here. This bias allows double occupancy of the adatom. In this regime no spin-diode effect is observed. The spin polarized currents are the same (in modulus) for both positive and negative eV.

The current in the double occupancy regime (Fig. 2.7) has a similar behavior for both positive and negative biases. Note that $|I_\uparrow| > |I_\downarrow|$ for $V > 0$ and $V < 0$, in contrast to the single occupancy regime where we find $I_\uparrow \approx I_\downarrow$ for $V > 0$ [Fig. 2.4]; hence no spin-diode effect is observed here. In Figs. 2.8(a)-(d) we show a zoom of the spin-resolved currents in the range of negligible tip-adatom coupling. As before, we observe Friedel oscillations, which reflect the disturbance in the LDOS due to the localized impurity (adatom). The dashed black lines in Figs. 2.8(a)-(d) show the current obtained via Eq. (2.22).

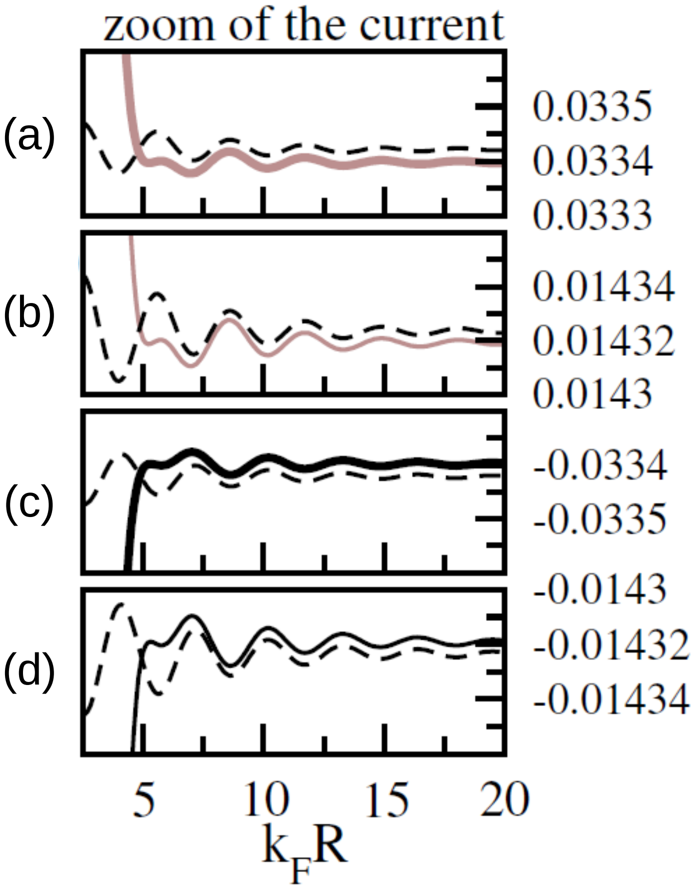

Figure 2.8 – Zoom of the spin-resolved currents in the range of negligible tip-adatom coupling.

2.8.3 Current Polarization

Figure 2.9 (a) displays the current polarization, $\wp = (I_1^\uparrow - I_1^\downarrow)/(I_1^\uparrow + I_1^\downarrow)$, as a function of R. Both single ($|eV| = 30\Gamma_0$) and double ($|eV| = 150\Gamma_0$) occupancies are shown. For $eV = -30\Gamma_0$ (solid red line) the polarization is approximately constant $\sim 40\%$ while for $eV = +30\Gamma_0$ (solid black line) it is strongly suppressed when the tip is close to the adatom. This is a type of *spatially resolved* spin-diode (9), which allows a polarized current to flow only for reverse bias. In the case of double occupancy, though, both positive and negative biases present a similar behavior

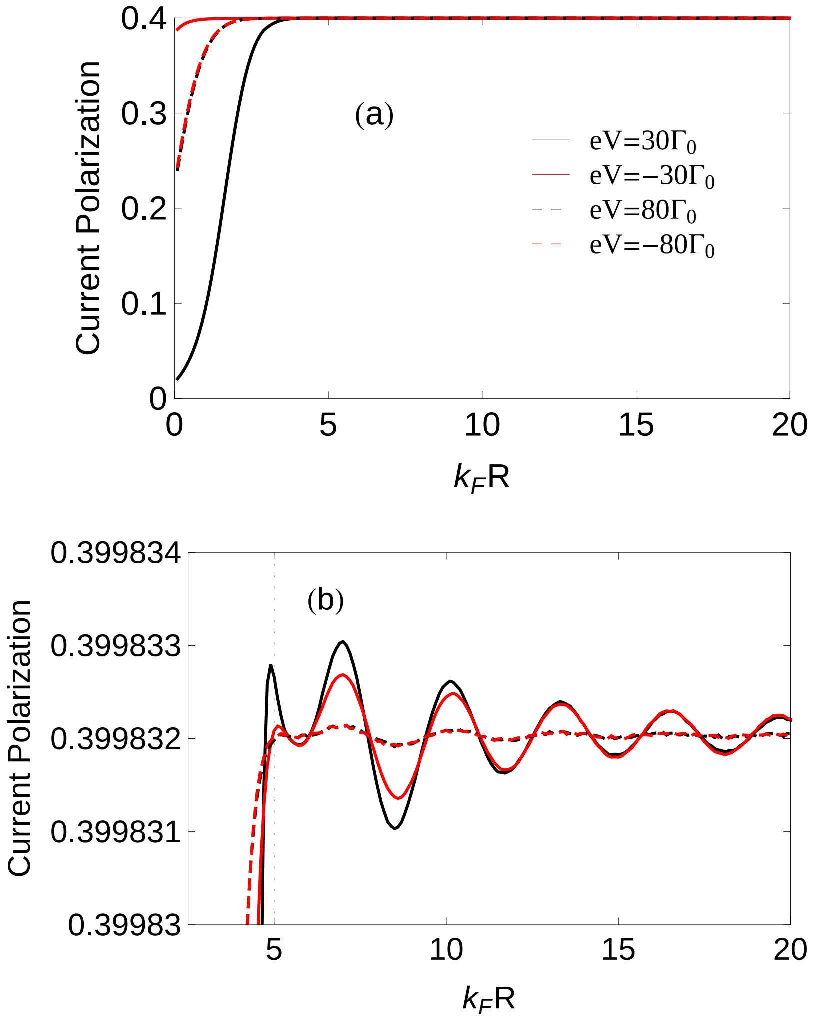

Figure 2.9 – (a) Current polarization against R. In the single occupancy regime ($eV = \pm 30\Gamma_0$, solid lines) the current polarization is approximately constant for reverse bias ($V < 0$, red curve) and goes down to zero for direct bias ($V > 0$, black curve) when the tip is close to the adatom. In the case of double occupancy ($eV = \pm 80\Gamma_0$, dashed lines) the current polarization is suppressed for small R, however it does not vanish; notice that the dashed lines lie essentially on top of each other. For large R's, the polarization for both single and double occupancies tends to a plateau and presents tiny oscillations (b).

with a 40% current polarization away from the adatom and a slight suppression as the tip moves closer to it. This 40% current polarization for large R's in the single- *and* double-occupancy cases follows straightforwardly by calculating $\wp$ using the spin-resolved non-resonant currents in Eq. (2.24). Figure 2.9 (b) shows a blow up of the current polarization and also reveals Friedel oscillations.

Chapter 3

Majorana Fermions: “sneaky” fermions

We start this section by briefly reviewing some of the Majorana fermion properties mentioned in Chapter 1 and then introducing the Kitaev model, which we use to simulate the real systems composed of semiconductor nanowires with strong spin-orbit coupling brought into proximity to an s-wave superconductor (31, 32, 76, 77).

Majorana fermions are neutral spin-$\frac{1}{2}$ ‘particles’ that are their own antiparticles. In terms of operators this property is translated as

$$\gamma^{\dagger} = \gamma \quad \text{and} \quad \gamma^2 = 1, \tag{3.1}$$

where γ denotes one of these modes. Calling a Majorana mode a ‘particle’ can be sometimes misleading in the sense that, unlike a usual electronic state in a metal there is no meaning in saying that a state is being occupied or not by a Majorana. This is so because a Majorana can be viewed as a half-electron. In this way, to obtain an electronic state with a well-defined occupation number two Majoranas, e.g., γ_A and γ_B, should be combined

$$f = \frac{1}{2}\left(\gamma_A + i\gamma_B\right) \quad \text{and} \quad f^{\dagger} = \frac{1}{2}\left(\gamma_A - i\gamma_B\right), \tag{3.2}$$

being $f^{\dagger}$ (f) the creation (annihilation) operator of a normal fermion. From the relations above and using the conventional anti-commutation relation obeyed by electrons $\{f, f^{\dagger}\} = 1$ and $\{f, f\} = 0$, we obtain

$$\{\gamma_i, \gamma_j\} = 2\delta_{ij}, \quad i, j = \mathrm{A}, \mathrm{B}. \tag{3.3}$$

The natural question now is where should we look for such exotic entities? In condensed matter systems we know that none of the elementary particles fulfill the relations above. If there is a chance of observing Majoranas in solid state systems they must emerge in the form of non-trivial excitations (2, 13, 78). Superconductors and similar systems where fermions pair and condense offer the ideal platform to search for such excitations. In superconducting phases for instance, the so-called Bogoliubov quasiparticles satisfy particle-hole symmetry $\gamma^{\dagger}(\varepsilon) = \gamma(-\varepsilon)$, consequently, the zero-energy quasiparticles $\gamma^{\dagger}(0) = \gamma(0)$ might represent the Majorana fermions we are looking for, i.e., they would emerge as zero-energy excitations of the system. Isolated Majorana fermions were predicted to occur in vortices and on the edges of effective spinless superconducting systems with triplet pairing - p-wave pairing symmetry in 1D and $p_x \pm ip_y$ pairing symmetry in 2D (26, 38, 79–81).

Many proposals for realizing Majorana fermions in condensed matter systems have been suggested (28, 34, 35, 39, 41, 82–87). In our study, however, we are particularly interested in the setups involving a 1D nanowire with spin-orbit coupling with proximity-induced s-wave superconductivity and an externally induced Zeeman splitting. In the following we present the Kitaev toy model that is a realization of such a system (88).

3.1 Kitaev model

We have mentioned that Majorana fermions can appear bound to vortices of p-wave superconductors or similarly at the surface of 3D topological insulators in proximity to an s-wave superconductor. So far, in none of these systems Majorana modes have been observed.

In this section, we introduce the Kitaev model, which as we will see, hosts Majorana fermions localized at the ends of the chain and can be experimentally realized with the current available technology by combining a semiconducting nanowire with spin-orbit interaction subjected to an external magnetic field and in proximity to an s-wave superconductor. In this context, the model was first studied by Kitaev (50) and consists of a 1D tight-binding chain of spinless regular fermions with p-wave superconductivity. The Hamiltonian that describes the system is given by

$$H = -\mu \sum_{j=1}^{N} c_j^{\dagger} c_j - \frac{1}{2} \sum_{j=1}^{N-1} \left(t c_j^{\dagger} c_{j+1} + \Delta e^{i\phi} c_j c_{j+1} + \text{H.c.} \right), \tag{3.4}$$

where $c_j^{\dagger}$ (c_j) creates (annihilates) an electron at site j, t is the hopping parameter, μ the chemical potential measured from the ground state energy, Δ the p-wave pairing amplitude and ϕ its corresponding superconducting phase. Note that this Hamiltonian is not time-reversal symmetric since it accounts for only one spin component.

Let us first consider periodic boundary conditions and study the bulk properties of the chain. By Fourier transforming the creation and annihilation operators,

$$\begin{aligned} c_j &= \frac{1}{\sqrt{2\pi}}\sum_k e^{ikx_j} c_k, \\ c_j^\dagger &= \frac{1}{\sqrt{2\pi}}\sum_k e^{-ikx_j} c_k^\dagger, \end{aligned} \tag{3.5}$$

in which $x_j = ja$ and $a = 1$ is the lattice constant, we can rewrite the Hamiltonian (3.4) as

$$H = \frac{1}{2}\sum_k \left(\varepsilon_k c_k^\dagger c_k - \varepsilon_k c_{-k} c_{-k}^\dagger + \Delta_k c_{-k} c_k + \Delta_k^* c_k^\dagger c_{-k}^\dagger\right) + \frac{1}{2}\sum_k \varepsilon_k, \tag{3.6}$$

with $\varepsilon_k = -\mu - t\cos k$ the kinetic energy and $\Delta_k = -i\Delta e^{i\phi}\sin k$ the transformed pairing potential.

Using a matrix representation we can express the equation above (up to a constant term) as

$$H = \sum_k \begin{pmatrix} c_k^\dagger & c_{-k} \end{pmatrix} \begin{pmatrix} \varepsilon_k & \Delta_k^* \\ \Delta_k & -\varepsilon_k \end{pmatrix} \begin{pmatrix} c_k & c_{-k}^\dagger \end{pmatrix}, \tag{3.7}$$

or in terms of quasiparticle operators (24)

$$a_k = u_k c_k + v_k c_{-k}^*, \tag{3.8}$$

as

$$H = \sum_k E_{\text{bulk}}(k) a_k^\dagger a_k, \tag{3.9}$$

with

$$E_{\text{bulk}} = \pm\sqrt{\varepsilon_k^2 + |\Delta_k|^2} \tag{3.10}$$

and

$$u_k = \frac{\Delta_k}{|\Delta_k|}\frac{\sqrt{E_{\text{bulk}} + \varepsilon_k}}{\sqrt{2E_{\text{bulk}}}}, \qquad v_k = \left(\frac{E_{\text{bulk}} - \varepsilon_k}{\Delta_k}\right) u_k. \tag{3.11}$$

In Fig. 3.1 we plot the bulk energy as a function of k in the absence ε_k (solid blue curves) and

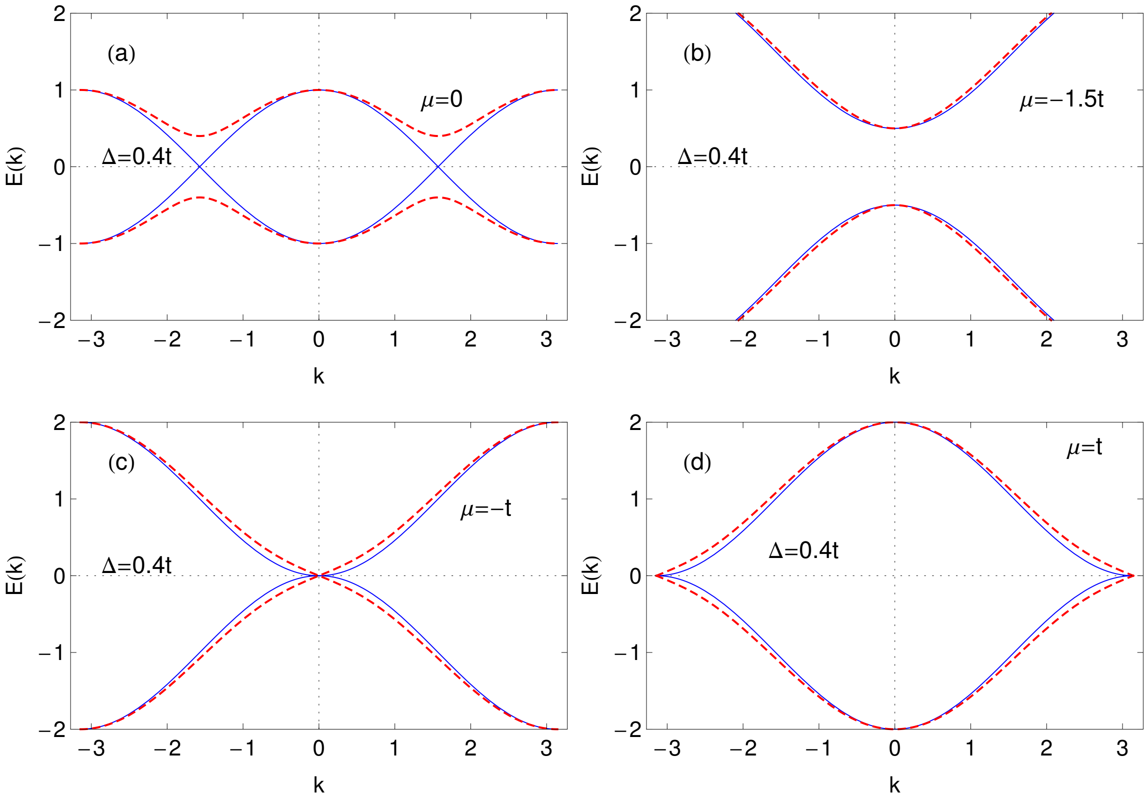

Figure 3.1 – Bulk energy for the Kitaev model as a function of k for $\Delta = 0.4t$ and several values of μ. The solid blue curves represent the energy in the absence of superconductivity. The dashed red lines show what when $\Delta \neq 0$ a gap opens at $k = \pm\pi/2$ (a). In (b) $|\mu| > t$ and we are in the trivial gapped phase. The panels (c) and (d) show that when $\mu = -t$ or t the gap closes at $k = 0$ or $k = \pm\pi$, respectively, indicating that there are different phases conneted by a gap close.

in the presence of superconductivity E_{bulk} (dashed red lines) for different values of the chemical potential μ. We can see in 3.1 (a) that the pairing potential Δ_k opens a gap at $k = \pm\pi/2$. For $|\mu| > t$ [Fig. 3.1 (b)], the system is always gapped independent of the value of Δ_k. However, the gap closes for $\mu = t$ or $-t$, exactly when the Fermi level respectively coincides with the top and bottom of the conduction band, see Figs. 3.1 (c) and 3.1 (d). Being Δ_k an odd function of k, there is no Cooper pairing at $k = 0$ and $k = \pm\pi$, thus leaving the system gapless when $\mu = \pm t$.

Apparently, the physics of the system is different in two cases: (i) $\mu < -t$ ($\mu > t$) Fig. 3.1 (b) and (ii) $|\mu| < t$ Fig. 3.1 (a), both in the gapped regime. The first connects smoothly to the vacuum when we take $\mu \to -\infty$ (independent of Δ_k), where no fermions are present. In the second, on the other hand, a partially filled band acquires a gap due to the p-wave pairing Δ_k. These two regimes are called strong and weak pairing, respectively. They actually constitute two distinct phases separated by a phase transition at which the bulk gap closes. This means that to go from one phase to the other, the bulk gap has necessarily to close like in Figs. 3.1 (c) and 3.1 (d). In this thesis, we will not show how to express the 'topological invariant' distinguishing these two phases (50). We want though to emphasize that the 'non-trivial topology' characterizing the weak pairing phase leads to the appearance of Majorana modes in the Kitaev chain with open boundary conditions. In fact, as we will see, these modes appear at the ends of the chain. This is so due to the bulk-boundary correspondence (27).

The Kitaev model is the simplest example of a superconducting phase (topological superconductor) that supports Majorana fermions. According to Eq. (3.2), we can express the fermion operators in terms of two Majorana operators for each site,

$$\begin{aligned} c_j &= e^{-i\phi/2}\frac{(\gamma_{Bj} + i\gamma_{Aj})}{2}, \\ c_j^\dagger &= e^{i\phi/2}\frac{(\gamma_{Bj} - i\gamma_{Aj})}{2}, \end{aligned} \tag{3.12}$$

and from the relation above we have

$$\begin{aligned} \gamma_{Aj} &= i\left(e^{-i\phi/2}c_j^\dagger - e^{i\phi/2}c_j\right), \\ \gamma_{Bj} &= e^{i\phi/2}c_j + e^{-i\phi/2}c_j^\dagger. \end{aligned} \tag{3.13}$$

It is quite simple to see that γ_{Aj} and γ_{Bj} do satisfy the condition $\gamma^\dagger = \gamma$ as well as the anticommutation relation $\{\gamma_{\alpha i}, \gamma_{\alpha' j}\} = 2\delta_{\alpha\alpha'}\delta_{ij}$.

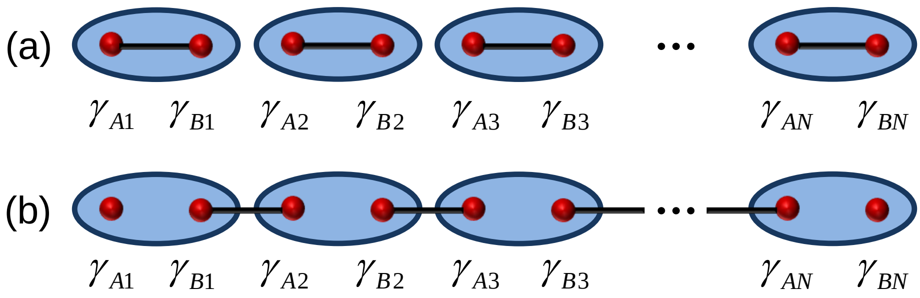
(a)
γ_{A1} γ_{B1} γ_{A2} γ_{B2} γ_{A3} γ_{B3} γ_{AN} γ_{BN}
(b)
γ_{A1} γ_{B1} γ_{A2} γ_{B2} γ_{A3} γ_{B3} γ_{AN} γ_{BN}

Figure 3.2 – Illustration of the Hamiltonian in Eq. (3.14) for (a) $\mu \neq 0$ and $\Delta = t = 0$, and (b) $\mu = 0$ and $\Delta = t \neq 0$.

In terms of Majorana operators the Hamiltonian (3.4) reads

$$H = -\frac{\mu}{2}\sum_{j=1}^{N}\left(1 + i\gamma_{Bj}\gamma_{Aj}\right) - \frac{i}{4}\sum_{j=1}^{N-1}\left[\left(\Delta + t\right)\gamma_{Bj}\gamma_{Aj+1} + \left(\Delta - t\right)\gamma_{Aj}\gamma_{Bj+1}\right]. \tag{3.14}$$

The easiest way of seeing this Hamiltonian leads to localized Majorana modes is to first consider two limiting cases.

(a) The first case corresponds to $\mu < 0$ but $t = \Delta = 0$, in which the chain resides in what is called the topologically trivial phase. Hamiltonian (3.14) reduces to

$$H = -\frac{\mu}{2}\sum_{j=1}^{N}\left(1 + i\gamma_{Bj}\gamma_{Aj}\right), \tag{3.15}$$

which we can interpret as a pairing between Majoranas A and B at the same lattice site, see Fig.3.2 (a). In this case, the ground state is unique and corresponds to the vacuum of c_j fermions [see first term in Eq. (3.4)]. The spectrum of the system is gapped since it costs a finite energy $|\mu|$ to add a spinless electron to the chain. These conclusions are still valid even away from this fine-tuned condition as long as the gap persists so that the chain remains in the trivial phase.

(b) The second case is the special situation in which $t = \Delta \neq 0$ and $\mu = 0$ (non-trivial or topological phase). The Hamiltonian here is given by

$$H = -i\frac{t}{2}\sum_{j}^{N-1}\gamma_{Bj}\gamma_{Aj+1}, \tag{3.16}$$

which corresponds to pairing Majoranas at adjacent sites, see Fig. 3.2 (b). We now define new fermionic annihilation and creation operators

$$d_j = \frac{1}{2}\left(\gamma_{Aj+1} + i\gamma_{Bj}\right) \quad \text{and} \quad d_j^\dagger = \frac{1}{2}\left(\gamma_{Aj+1} - i\gamma_{Bj}\right), \tag{3.17}$$

such that

$$\gamma_{Aj+1} = d_j + d_j^\dagger \quad \text{and} \quad \gamma_{Bj} = i\left(d_j^\dagger - d_j\right). \tag{3.18}$$

In terms of these new fermionic operators the Hamiltonian reads

$$H = t\sum_{j=1}^{N-1}\left(d_j^\dagger d_j - \frac{1}{2}\right), \tag{3.19}$$

which is diagonal in the basis described by the d_j operators and has a ground state with none of the states occupied. The gap remains in this case since it costs an energy t to add an electron d_j. We note, however, that the single particle Hilbert space spanned by these operators is only of dimension $N-1$ and not equal the original size N. In fact the Majorana operators γ_{A1} and γ_{BN} *do not* appear in the Hamiltonian and we then can construct an extra fermionic operator $f = \frac{1}{2}\left(\gamma_{A1} + i\gamma_{BN}\right)$, corresponding to the missing state that costs zero energy and thus originates a two-fold ground-state degeneracy. The fermionic state represented by the operator f is highly non-local since the Majoranas γ_{A1} and γ_{BN} are localized on the opposite ends of the chain.

To find out when the system supports unpaired Majoranas for a more general parameter regime, we have to find the eigenfunctions of the Hamiltonian and show that these contain a zero-energy solution. It can be shown, however, that the Majorana end states remain as long as the chemical potential μ lies within the gap $|\mu| < t$ (50). In this situation, the Majoranas γ_{A1} and γ_{BN} are no longer completely decoupled and there is an overlap of their wave-functions, which causes the degeneracy of the ground state to be lifted. Despite this splitting (exponential decaying), we will keep calling the Majorana end modes as zero energy states.

There are some challenges involved in realizing the Kitaev model experimentally: (i) the 'fermion doubling problem' - electrons are spin-$\frac{1}{2}$ particles, thus half of the degrees of freedom must be frozen out so that the 1D system appears effectively 'spinless'. An external magnetic field applied to the system or the proximity to a ferromagnetic insulator combined with spin-orbit interaction can overcome this problem by lifting the degeneracy associated to it (89, 90);

(ii) long-range-order p-wave superconductivity is one of the ingredients in the Kitaev model; it is not only extremely rare in nature but stabilizing it for a ‘spinless’ system is exceedingly difficult. Fortunately, it was shown that an alternate route to surmount this issue is possible (91). In the current proposals this route can be translated as a pairing field due to the proximity coupling to a conventional s-wave superconductor.

As we shall see in the next section, the proposal we are interested in employs three ‘basic’ ingredients to cleverly engineer such a system: superconducting proximity effects on semiconductors with strong spin-orbit coupling and time reversal symmetry breaking.

3.2 Practical realization of Majorana modes in superconducting 1D nanowires

The purpose of this thesis is not to show the equivalence between the 1D Kitaev model and the proposed experimental setup (92) containing a wire with spin-orbit interaction, induced superconductivity and subjected to a magnetic field. One of our goals is to emphasize that the system presented here is experimentally feasible and has been intensely investigated in the last 2 years (1, 42–46). In addition, the 1D system has advantages over the 2D analogue. Although the physics responsible for the emergence of the zero-energy Majorana modes is the same in 1D and 2D, experimentally the 1D setups offer for example, the possibility of generating the Zeeman splitting using a parallel magnetic field (31, 32) and a significantly enhanced gap that protects the end modes from thermal effects (93).

In order to present a succinct discussion on how realistic systems can be realized, we follow the reviews by Alicea (13) and Leijnse and Flensberg (2).

Let us start by considering the effects of proximity-induced superconductivity[‡]. The system we consider is a semiconducting wire described by the single-particle Hamiltonian

$$\mathscr{H}_0 = \sum_{\sigma=\uparrow,\downarrow} \int dr \Psi_\sigma^\dagger(\mathbf{r}) H_0 \Psi_\sigma(\mathbf{r}) , \tag{3.20}$$

[‡] We have no intention to introduce the superconductivity topic here. For first readings we suggest Refs. (61, 94).

with

$$H_0(\mathbf{r}) = \frac{\mathbf{p}^2}{2m^*} - \mu + V(\mathbf{r}) + \alpha(\mathbf{E}(\mathbf{r}) \times \mathbf{p}) \cdot \sigma + \frac{1}{2} g\mu_B \mathbf{B}(\mathbf{r}) \cdot \sigma, \tag{3.21}$$

where m^* is the semiconductor effective mass, μ_B the Bohr magneton, g the effective gyromagnetic factor, **B** an applied magnetic field **E** the electric field felt by the valence electrons and σ the Pauli matrices. The fourth term in the expression above is the spin-orbit interaction with strength α, which can represent both the Rashba (95) and Dresselhaus (96) terms.

If an interface between a semiconductor and a superconductor is made, electrons can tunnel between the two systems. In a few words, the electrons in the semiconductor feel an effective 'proximity-induced' superconducting pairing field (97). The pairing effect can be included in the problem by considering the following phenomenological Hamiltonian

$$\mathscr{H}_S = \int drdr' \Psi_\uparrow(\mathbf{r}) \Delta\left(\mathbf{r},\mathbf{r}'\right) \Psi_\downarrow\left(\mathbf{r}'\right) + \text{H.c.}, \tag{3.22}$$

in which $\Delta(\mathbf{r},\mathbf{r}')$ is the pairing potential. We assume here the pairing symmetry to be s-wave, which induces singlet pairing between spin-up and -down electrons.

By using the so-called Nambu spinors (23)

$$\bar{\Psi}(\mathbf{r}) = \begin{pmatrix} \Psi_\uparrow(\mathbf{r}) \\ \Psi_\downarrow(\mathbf{r}) \\ \Psi_\downarrow^\dagger(\mathbf{r}) \\ -\Psi_\uparrow^\dagger(\mathbf{r}) \end{pmatrix} \tag{3.23}$$

common used when handling superconducting systems (to account for electrons and holes), we can write the total Hamiltonian as

$$\begin{aligned} \mathscr{H} &= \mathscr{H}_0 + \mathscr{H}_S \\ &= \frac{1}{2}\int drdr' \bar{\Psi}^\dagger(\mathbf{r}) \left[\bar{H}_0(\mathbf{r})\,\delta\left(\mathbf{r}-\mathbf{r}'\right) + \bar{\Delta}\left(\mathbf{r},\mathbf{r}'\right)\right] \bar{\Psi}(\mathbf{r}), \end{aligned} \tag{3.24}$$

where

$$\bar{H}_0(\mathbf{r}) = \begin{pmatrix} H_0(\mathbf{r}) & 0_{2\times 2} \\ 0_{2\times 2} & -\sigma_y H_0^*(\mathbf{r})\,\sigma_y \end{pmatrix} \tag{3.25}$$

and

$$\bar{\Delta}\left(\mathbf{r},\mathbf{r}'\right)=\begin{pmatrix} 0_{2\times 2} & \Delta^{*}\left(\mathbf{r},\mathbf{r}'\right)I_{2\times 2} \\ \Delta\left(\mathbf{r},\mathbf{r}'\right)I_{2\times 2} & 0_{2\times 2} \end{pmatrix}. \tag{3.26}$$

The term $-\sigma_y H_0^{*}\left(\mathbf{r}\right)\sigma_y$ is the time-reversal of $H_0\left(\mathbf{r}\right)$. We stress that by rewriting the total Hamiltonian as in (3.24), we have not introduced any new physics to the problem.

The goal now is to show that the parameters in Eq. (3.24) can be engineered such that it resembles a spinless p-wave superconductor, (Kitaev Hamiltonian) whose eigensolutions are Majorana fermion states. This means that we want to continuously transform Hamiltonian (3.24) into the Hamiltonian

$$\mathscr{H}_{pw}=\int dx\Psi^{\dagger}\left(x\right)\left(\frac{p^2}{2m^{*}}-\mu\right)\Psi\left(x\right)+\Psi\left(x\right)e^{i\phi}\Delta p_x\Psi\left(x\right)+\text{H.c.} \tag{3.27}$$

which is the continuous version of (3.4), and vice-versa. In the ‘topological’ language we say that both Hamiltonians describe topologically equivalent systems (27).

3.2.1 Real system

A sketch of the experimental setup is shown in Fig. 3.3, a InSb or InAs nanowire, for example, in proximity to an s-wave superconductor (e.g., Nb or Al) and subjected to an external magnetic field **B** (not shown in the figure). The spin-orbit interaction of Rashba, in these wires is already an “intrinsic” (e.g., due to the confining potential) ingredient and its strength α can be electrically manipulated via a gate potential (98). The wire is supposed to be long enough to avoid size quantization along the wire direction and we assume that the gate voltage can tune the chemical potential so that only one sub-band is occupied. The Hamiltonian of this system is a particular case of (3.21),

$$H_0\left(x\right)=\frac{k^2}{2m^{*}}-\mu+\tilde{\alpha}k_x\sigma_y+\frac{1}{2}\tilde{B}, \tag{3.28}$$

where we have considered $\hbar=1$, $\tilde{\alpha}=\alpha E$ and $\tilde{B}=g\mu_B B$. We also assume that the proximity-induced pairing field is homogeneous and couples only electrons at the same position $\Delta\left(x,x'\right)=\Delta\delta\left(x-x'\right)$.

Let us discuss now what happens to the energy spectrum of the system when each one of the

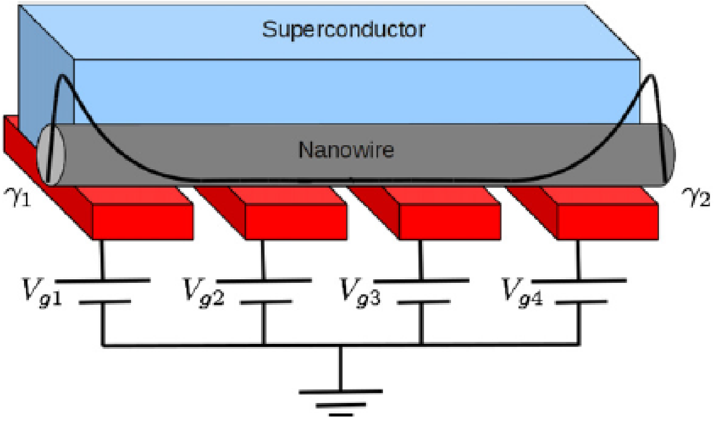

Figure 3.3 – Illustration of the real setup. A nanowire, e.g., InSb, with spin-orbit interaction in proximity to a bulk s-wave superconductor. e.g., Nb. The gate electrodes tune the chemical potential of the wire such that the topological regime is reached. Majorana fermions γ_1 and γ_2 appear on the edges of the wire. This figure was taken from the review by Leijnse and Flensberg (2).

ingredients: spin-orbit, magnetic field and proximity induced superconductivity, is added (see Fig.3.4). The Rasbha spin-orbit interaction "shifts sideways" the initially doubly-degenerate free electron bands; the projection of the spin in each branch can be seen in Fig.3.4 (a). In (b) we show the effect of the magnetic field. It breaks time-reversal symmetry and lifts the spin degeneracy. If the chemical potential is placed within the gap spinless superconductivity can be induced by the proximity effect. Figure 3.4 is the same as (b) for a higher B, which provides a larger gap and the possibility of more easily tune μ. The dispersion relations shown in Fig. 3.4 are obtained by diagonalizing Eq. (3.28), which results in

$$\varepsilon_{\pm}(k_x) = \frac{k_x^2}{2m^*} - \mu \pm \sqrt{\tilde{\alpha}^2 k_x^2 + \tilde{B}^2}, \tag{3.29}$$

where $+$ $(-)$ represents the upper branch (lower branch).

We now turn on the proximity-induced superconducting pairing $\Delta > 0$, and diagonalize Eq. (3.24), the 1D version. The energy spectrum can be seen in Fig. 3.4 (d). Note that the number of bands doubled but there are only two independent solutions since the system possesses particle-hole symmetry, i.e.,positive and negative solutions are identical (creating a quasiparticle with energy E is equivalent to annihilating one with energy $-E$). The Δ potential pairs fermions in the lower band with momentum k_x and $-k_x$, thus driving the wire into Kitaev's topological phase. Singlet pairing (s-wave superconductivity) in Eq. (3.22) generates p-wave pairing because spin-orbit coupling favors opposite spins for k and $-k$ states. The topologi-

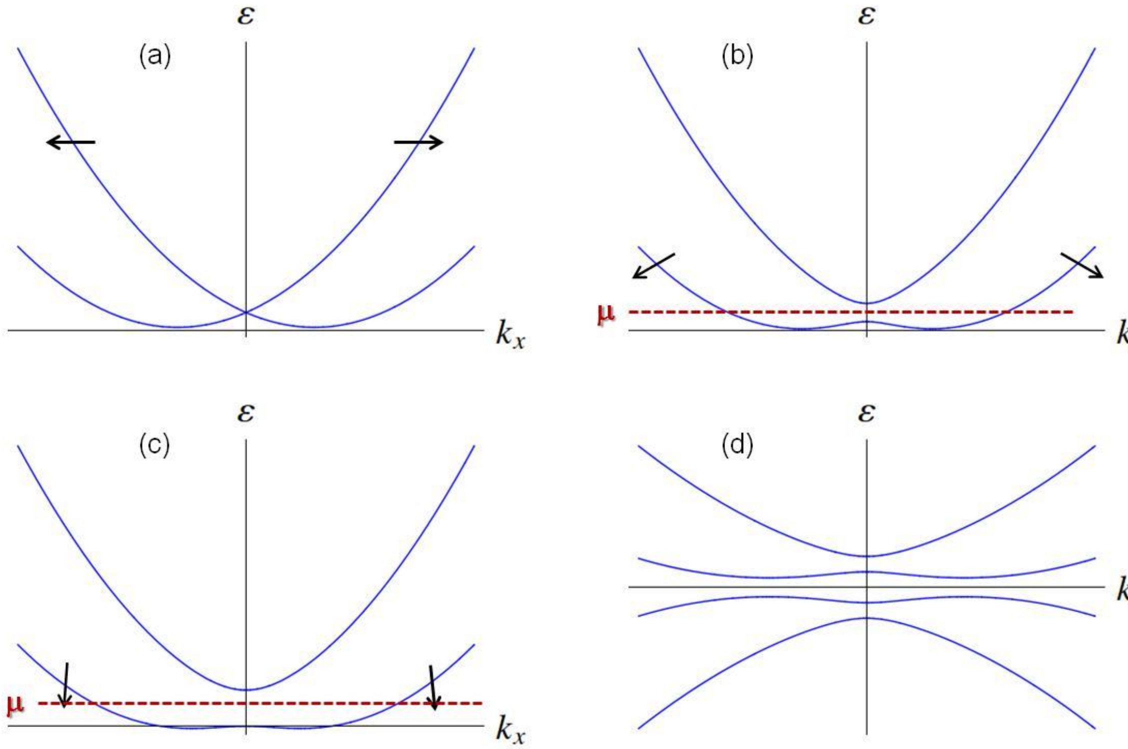

Figure 3.4 – Energy dispersion relation of Hamiltonian (3.28) with $|\tilde{B}| = 0$ (a). When the magnetic field is switched on (b), the bands are split. (c) Effect of a more intense magnetic field. (d) Energy bands when the superconducting pairing potential Δ is non-zero.

cal phase requires $|\Delta < \tilde{B}|/2$. The limit $\Delta > |\tilde{B}|/2$ violates the ‘spinless’ requirement because pairing intermixes states from the upper band.

In the topological regime, the connection with Eq. (3.4) is more evident when $|\tilde{B}| \gg \frac{m^*\tilde{\alpha}^2}{2}, \Delta$. Such a large magnetic field causes the spins to nearly completely polarize. The large gap also allows us to construct a single-band effective Hamiltonian. The eigenvalue equation obeyed by Hamiltonian (3.28) written in a matrix representation (σ_z basis) is given by

$$\begin{pmatrix} \frac{k_x^2}{2m^*} - \mu + \frac{\tilde{B}}{2} & -i\tilde{\alpha}k_x \\ i\tilde{\alpha}k_x & \frac{k_x^2}{2m^*} - \mu - \frac{\tilde{B}}{2} \end{pmatrix} \begin{pmatrix} \Psi_\uparrow \\ \Psi_\downarrow \end{pmatrix} = \varepsilon \begin{pmatrix} \Psi_\uparrow \\ \Psi_\downarrow \end{pmatrix}. \tag{3.30}$$

To derive the low-energy Hamiltonian (spins down sector) we apply the folding down (99, 100) method, which results in

$$\begin{aligned} \Psi_\downarrow(x) &\approx \Psi_x, \\ \Psi_\uparrow &\approx \frac{\tilde{\alpha}}{|\tilde{B}|} k_x \Psi_x \end{aligned} \tag{3.31}$$

and

$$\mathscr{H}_{eff} = \int \left[\Psi_x^\dagger \left(\frac{k_x^2}{2m^*} - \mu - \frac{\tilde{B}}{2} \right) \Psi_x + i \frac{\tilde{\alpha}}{|\tilde{B}|} \Delta \Psi_x k_x \Psi_x \right] . \tag{3.32}$$

The last equation is equivalent to Hamiltonian (3.4).

In summary, we have showed that the Kitaev model can, at least in theory, be experimentally engineered by using a semiconducting nanowire with strong spin-orbit interaction, placed in a external magnetic field and in proximity to an *s*-wave superconductor. The Majorana zero modes in this setup emerge at the ends of the wire, analogously to the zero-energy states in the Kitaev model. In fact, there are several reports of the signatures of these zero modes (1, 42–46), however, there is still controversy as to what the observed modes really means: Kondo effect, disorder and Andreev reflections are some of the possibilities.

In the next chapter we describe in detail the setup we studied in order to possibly observe the emergence of Majorana zero modes. We suggest three experimental ways of probing these end modes in two-terminal conductance measurements through a dot side-coupled to a superconducting nanowire. Our results lead us to believe that these measurements are a smoking-gun evidence for the observation of Majorana zero modes.

Chapter 4

Majorana leaking into a quantum dot connected to a Kitaev wire

Here we use the Green's function technique to investigate the transport through a single-level quantum dot coupled to source and drain leads and connected to a Kitaev wire, see Sec. 3.1. The goal is to calculate the conductance G through the side-coupled dot (see Fig. 4.1) as a way of probing the Majorana end mode present in the topological superconducting nanowire represented by the Kitaev chain. As we show in the following, by tuning some of the parameters of the system, e.g., the dot-chain coupling or the dot level, via a gate voltage, we can observe a leakage of this wire end mode into the dot, which emerges as a resonance in the dot. The most surprising and interesting feature of this setup is that this leaked Majorana mode is pinned to the Fermi level ε_F of the leads even when the dot level ε_{dot} is far off resonance.

4.1 Description of the system

The Hamiltonian of our system, see Fig. 4.1, in the electron representation can be written as

$$H = H_{\text{dot}} + H_{\text{Kitaev}} + H_{\text{dot-Kitaev}} + H_{\text{leads}} + H_{\text{dot-leads}}, \tag{4.1}$$

with

$$H_{\text{dot}} = (\varepsilon_{\text{dot}} - \varepsilon_F)\, d^\dagger d, \tag{4.2}$$

where $d^\dagger$ (d) creates (annihilates) a spinless electron with energy $\varepsilon_{\text{dot}} = \varepsilon_d - eV_g$, which is gate tunable, being V_g the gate potential ($e > 0$) and ε_d the dot level in the absence of the bias voltage. Without loss of generality, here we assume $\varepsilon_d = 0$.

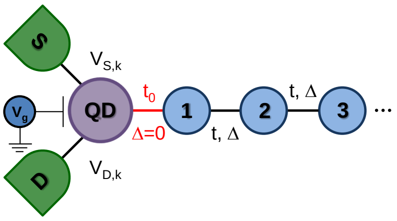

Figure 4.1 – Representation of a quantum dot (QD) coupled to source (S) and drain (D) metallic leads and connected to a Kitaev chain. The system dot+leads is considered as a site of the wire, however, with a distinct coupling parameter t_0 and no induced superconductivity $\Delta = 0$.

The Kitaev wire is represented by

$$H_{\text{Kitaev}} = -\mu \sum_{j=1}^{N} c_j^\dagger c_j - \frac{1}{2} \sum_{j=1}^{N-1} \left(t c_j^\dagger c_{j+1} + \Delta e^{i\phi} c_j c_{j+1} + H.c. \right), \tag{4.3}$$

with N the number of chain sites, $c_j^\dagger$ (c_j) the creation (annihilation) operator of an electron in the j-th site of the wire and μ its chemical potential. The nearest-neighbor hopping strength is denoted by t and the parameters Δ and ϕ characterize the p-wave pairing amplitude and the corresponding superconducting phase. The leads are described by

$$H_{\text{leads}} = \sum_{\ell=S,D} \sum_{\mathbf{k}} (\varepsilon_{\ell\mathbf{k}} - \varepsilon_F) c_{\ell\mathbf{k}}^\dagger c_{\ell\mathbf{k}}, \tag{4.4}$$

where $c_{\ell\mathbf{k}}^\dagger$ ($c_{\ell\mathbf{k}}$) creates (annihilates) a spinless electron with wavevector $\mathbf{k}$ in the lead $\ell = S, D$, whose Fermi energy is ε_F.

The coupling between the dot and the first chain site is given by

$$H_{\text{dot}-\text{Kitaev}} = t_0 \left(d^\dagger c_1 + c_1^\dagger d \right), \tag{4.5}$$

t_0 being the hopping parameter, and the coupling between the leads and the dot is written as

$$H_{\text{dot}-\text{leads}} = \sum_{\mathbf{k},\ell} \left(V_{\ell\mathbf{k}} d^\dagger c_{\ell\mathbf{k}} + V_{\ell\mathbf{k}}^* c_{\ell\mathbf{k}}^\dagger d \right), \tag{4.6}$$

$V_{\ell\mathbf{k}}$ representing the electron tunneling between the dot and the source (S) and drain (D) leads. Note that there is no induced superconductivity in the dot, i.e., $\Delta = 0$. We also stress that our model goes beyond low-energy effective Hamiltonians (101, 102) by covering the complete range of parameters of the Kitaev model.

The next step would be to obtain the dot Green's function and extract from it the transport properties of the system. As a means of elucidating the role played by the Majorana zero mode, we choose to describe our system in the Majorana representation, see Fig. 4.2. To do so, we first decompose the electron operators c_j in terms of two Majorana operators γ_{Aj} and γ_{Bj},

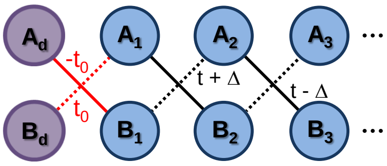

Figure 4.2 – Illustration of the system using the Majorana representation.

$$\begin{aligned} c_j &= e^{-i\phi/2}\frac{(\gamma_{Bj}+i\gamma_{Aj})}{2}, \\ c_j^{\dagger} &= e^{i\phi/2}\frac{(\gamma_{Bj}-i\gamma_{Aj})}{2} \end{aligned} \tag{4.7}$$

where j also includes the quantum dot operator d and is denoted by the index d. It is worth emphasizing that in our description the system dot+leads is also considered as a "site" of the chain, though with a different hopping parameter t_0 and zero superconducting pairing amplitude ($\Delta = 0$). As previously mentioned, the operators $\gamma_{\alpha j}$ ($\alpha = A, B$) have the property $\gamma_{\alpha j}^{\dagger} = \gamma_{\alpha j}$ and obey the commutation relation $\{\gamma_{\alpha j}, \gamma_{\alpha' j'}\} = 2\delta_{\alpha\alpha'}\delta_{jj'}$.

We now rewrite the full Hamiltonian (4.1) in this new basis,

$$H_{\text{dot}} = \frac{1}{2}(\varepsilon_{\text{dot}} - \varepsilon_F)(1 + i\gamma_{Bd}\gamma_{Ad}), \tag{4.8}$$

$$H_{\text{Kitaev}} = -\frac{\mu}{2}\sum_{j=1}^{N}\left(1 + i\gamma_{Bj}\gamma_{Aj}\right) - \frac{i}{4}\sum_{j=1}^{N-1}\left[(\Delta + t)\,\gamma_{Bj}\gamma_{Aj+1} + (\Delta - t)\,\gamma_{Aj}\gamma_{Bj+1}\right], \tag{4.9}$$

$$H_{\text{dot}-\text{Kitaev}} = \frac{i}{2}t_0\left(\gamma_{Bd}\gamma_{A1} - \gamma_{Ad}\gamma_{B1}\right) \tag{4.10}$$

and

$$H_{\text{dot}-\text{leads}} = \sum_{\mathbf{k},\ell}\left[e^{i\phi/2}\frac{V_{\ell\mathbf{k}}}{2}(\gamma_{Bd} - i\gamma_{Ad})\,c_{\ell\mathbf{k}} + e^{-i\phi/2}\frac{V_{\ell\mathbf{k}}^{*}}{2}c_{\ell\mathbf{k}}^{\dagger}(\gamma_{Bd} + i\gamma_{Ad})\right]. \tag{4.11}$$

By observing Fig. 4.2 and looking at the expressions above, we can see that in this new representation the dot Majorana A_d (B_d) is only coupled to the first chain site Majorana B_1 (A_1) but both A_d and B_d are connected to the leads (not shown in the figure). From now on we assume the pairing phase $\phi = 0$, which corresponds to a particular gauge choice.

We discuss next the procedure to obtain the dot Green's function and the spectral properties of the system.

4.2 Recursive Green's functions and related physical quantities

The numerical approach we adopt consists in iteratively calculating the Green's function of each site of the chain by adding sites one by one, i.e, we start with a one-site chain in the first step and obtain the corresponding Green's function. In the next step, we add another site and calculate the Green's function of the coupled system and so on. In the n-th step we have the exact Green's function of the last chain site taking into account the interaction with all the other sites. Using this procedure, we can obtain exactly the Green's function of any site of the chain. We shall illustrate this recursive method later on.

Let us first define the retarded dot Green's function as

$$G^r_{dd}\left(t,t'\right) = -i\theta\left(t-t'\right)\left\langle\left\{d\left(t\right),d^\dagger\left(t'\right)\right\}\right\rangle, \tag{4.12}$$

with $\theta\left(t-t'\right)$ the Heaviside function and the average $\langle\cdots\rangle$, as stated before, can be either a thermodynamic equilibrium average or a ground state expectation value calculated at zero temperature. Using the Majorana representation for the dot operators in (4.12) we can rewrite it as

$$G^r_{dd}\left(t,t'\right) = \frac{1}{4}\left[G^r_{BdBd}\left(t,t'\right) + G^r_{AdAd}\left(t,t'\right) + i\left(G^r_{AdBd}\left(t,t'\right) + G^r_{BdAd}\left(t,t'\right)\right)\right] \tag{4.13}$$

where $G^r_{\alpha d\beta d}\left(t,t'\right) = \langle\{\gamma_{\alpha d}\left(t\right),\gamma_{\beta d}\left(t'\right)\}\rangle$ is the Majorana Green's function. The question now is: why should we calculate the dot Green's function? As we have seen in the previous chapters, $G_{dd}\left(t,t'\right)$ (not necessarily the retarded Green's function) is connected to physical properties. In particular, we are interested in obtaining the local density of states (LDOS) of the dot ρ_{dot} given by

$$\rho_{\text{dot}}\left(\varepsilon\right) = -\frac{1}{\pi}\text{Im}G^r_{dd}\left(\varepsilon\right), \tag{4.14}$$

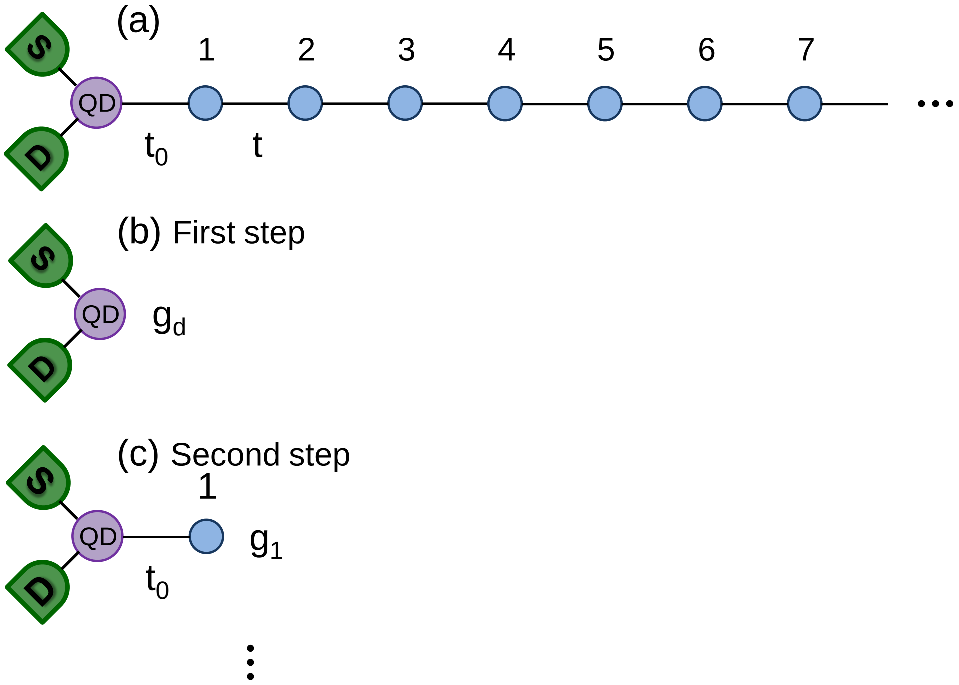

Figure 4.3 – Illustration of the recursive method used to obtain the Green's function of the dot. (a) Representation of the system. (b) and (c) show the first and second steps, respectively, of the process. In each of them the Green's function of the last site added is exactly calculated.

with $G^r_{dd}(\varepsilon)$ the Fourier transform of (4.12), and the conductance G (linear response) of the system written as

$$G=\frac{e^2}{\hbar}\int\frac{d\varepsilon}{2\pi}\frac{\Gamma_S\Gamma_D}{\Gamma_S+\Gamma_D}\left\{-2\mathrm{Im}G^r_{dd}(\varepsilon)\right\}\left(-\frac{\partial f_F}{\partial\varepsilon}\right), \tag{4.15}$$

where Γ_S and Γ_D are the corresponding broadenings due to the source and drain leads, respectively, and $f_F(\varepsilon)$ is the Fermi distribution function of the leads. The expression above is a generalized Landauer-type formula (68, 69, 103), which in principle can be used even for interacting systems.

Equation (4.14) as well as the LDOS of each site of the chain can also be directly expressed in terms of the Majorana Green's functions,

$$\rho_j(\varepsilon)=-\frac{1}{4\pi}\mathrm{Im}\left\{G^r_{AjAj}(\varepsilon)+G^r_{BjBj}(\varepsilon)+i\left[G^r_{AjBj}(\varepsilon)-G^r_{BjAj}(\varepsilon)\right]\right\}, \tag{4.16}$$

with $j=\mathrm{dot},1,2,\ldots,N$. We emphasize that the definition of $G^r_{\alpha j\beta j}$ is useful only to assess the contribution of each Majorana to the LDOS, however, these Green's functions are not related to any physical quantity.

We now continue with the calculation of $G_{dd}(t,t')$.[‡] To do so, we apply the equation of motion technique to each term on the right-hand side of Eq. (4.13). As we mentioned, let us first illustrate the recursive procedure we follow. In Fig. 4.3 (a) we show again a sketch of our system. In 4.3 (b) and 4.3 (c) we have the first two steps of the iterative process: (i) we obtain g_d[‡], i.e., the exact Green's function of the system dot+leads; (ii) Green's function g_1 of the system dot+leads+first site; (iii) … and so on till the last site g_N.

4.2.1 Equation of motion for $G_{\alpha d \beta d}(t,t')$

Here we derive in detail the equation of motion for $G_{AdAd}(t,t') = -i\theta(t-t')\langle\{\gamma_{Ad}(t), \gamma_{Ad}(t')\}\rangle$,

$$i\partial_t G_{AdAd} = \delta\left(t-t'\right)\langle\{\gamma_{Ad}(t), \gamma_{Ad}\left(t'\right)\}\rangle + \langle\{\dot{\gamma}_{Ad}(t), \gamma_{Ad}\left(t'\right)\}\rangle, \tag{4.17}$$

in which the operators evolve with the full Hamiltonian (4.1) in the Majorana representation according to the Heisenberg equation of motion $\dot{\gamma}_{\alpha d}(t) = i[H, \gamma_{\alpha d}]$, $\hbar = 1$. Thus for the time evolution of the operators we have

$$\begin{aligned} \dot{\gamma}_{Ad}(t) &= -\varepsilon_{\text{dot}}\gamma_{Bd}(t) - t_0\gamma_{B1}(t) - \textstyle\sum_{\mathbf{k},\ell}\left(V_{\ell\mathbf{k}}c_{\ell\mathbf{k}}(t) + V^*_{\ell\mathbf{k}}c^\dagger_{\ell\mathbf{k}}(t)\right), \quad &\text{(a)} \\ \dot{\gamma}_{Bd}(t) &= \varepsilon_{\text{dot}}\gamma_{Ad}(t) + t_0\gamma_{A1}(t) + i\textstyle\sum_{\mathbf{k},\ell}\left(V^*_{\ell\mathbf{k}}c^\dagger_{\ell\mathbf{k}}(t) - V_{\ell\mathbf{k}}c_{\ell\mathbf{k}}(t)\right). \quad &\text{(b)} \end{aligned} \tag{4.18}$$

Using the Majorana commutation relation and substituting Eq. (4.18a) into (4.17) we obtain

$$i\partial_t G_{AdAd}\left(t,t'\right) = 2\delta\left(t-t'\right) - i\varepsilon_{\text{dot}}G_{BdAd} - it_0 G_{B1Ad} - i\sum_{\mathbf{k},\ell}\left(V_{\ell\mathbf{k}}G_{\ell\mathbf{k}Ad} + V^*_{\ell\mathbf{k}}\tilde{G}_{\ell\mathbf{k}Ad}\right). \tag{4.19}$$

As previously mentioned, the dot Majorana A_d is coupled to the leads and only to Majorana B_1 of the first chain site. So now we should calculate $G_{B1Ad}(t,t')$ and $\tilde{G}_{\ell\mathbf{k}Ad}(t,t') = -i\theta(t-t')\langle\{c^\dagger_{\ell\mathbf{k}}, \gamma_{\alpha d}\}\rangle$. The latter is easily obtained since it is just connected to the dot. Below we write down the expressions for the four Green's functions that couple the Majoranas A_d and

---

[‡] Since in this chapter the retarded Green's function is the only relevant quantity, from now on we drop the superscript 'r' and adopt the simpler notation $G_{ij}(t,t')$.

[‡] The lower case g_j is just pictorically representing the real Green's functions.

B_d to the leads,

$$\begin{cases} i\partial_t G_{\ell\mathbf{k}Ad} = \varepsilon_{\ell\mathbf{k}} G_{\ell\mathbf{k}Ad} + V^*_{\ell\mathbf{k}} \left(G_{BdAd} + iG_{AdAd}\right)/2, \\ i\partial_t G_{\ell\mathbf{k}Bd} = \varepsilon_{\ell\mathbf{k}} G_{\ell\mathbf{k}Bd} + V^*_{\ell\mathbf{k}} \left(G_{BdBd} + iG_{AdBd}\right)/2, \\ i\partial_t \tilde{G}_{\ell\mathbf{k}Ad} = -\varepsilon_{\ell\mathbf{k}} \tilde{G}_{\ell\mathbf{k}Ad} - V_{\ell\mathbf{k}} \left(G_{BdAd} - iG_{AdAd}\right)/2, \\ i\partial_t \tilde{G}_{\ell\mathbf{k}Bd} = -\varepsilon_{\ell\mathbf{k}} \tilde{G}_{\ell\mathbf{k}Bd} - V^*_{\ell\mathbf{k}} \left(G_{BdBd} - iG_{AdBd}\right)/2. \end{cases} \tag{4.20}$$

Fourier transforming Eqs. (4.19) and (4.20) and using the result to rewrite G_{AdAd}, we have

$$\begin{aligned} \left\{\varepsilon - \sum_{\mathbf{k},\ell} \frac{|V_{\ell\mathbf{k}}|^2}{2} \left[\left(\varepsilon - \tilde{\varepsilon}_{\ell\mathbf{k}}\right)^{-1} \quad + \quad \left(\varepsilon + \tilde{\varepsilon}_{\ell\mathbf{k}}\right)^{-1}\right]\right\} G_{AdAd}\left(\varepsilon\right) = 2 - it_0 G_{B1Ad}\left(\varepsilon\right) \\ - \quad i\left\{\varepsilon_{\mathrm{dot}} + \sum_{\mathbf{k},\ell} \frac{|V_{\ell\mathbf{k}}|^2}{2} \left[\left(\varepsilon - \tilde{\varepsilon}_{\ell\mathbf{k}}\right)^{-1} - \left(\varepsilon + \tilde{\varepsilon}_{\ell\mathbf{k}}\right)^{-1}\right]\right\} G_{BdAd}\left(\varepsilon\right), \end{aligned} \tag{4.21}$$

with $\varepsilon \to \varepsilon + i\eta$ and $\tilde{\varepsilon}_{\ell\mathbf{k}} = \varepsilon_{\ell\mathbf{k}} - \varepsilon_F$. In a more compact form

$$\left(\varepsilon - \Sigma_L\right) G_{AdAd}\left(\varepsilon\right) = 2 + i\mu_0 G_{BdAd}\left(\varepsilon\right) - it_0 G_{B1Ad}\left(\varepsilon\right), \tag{4.22}$$

where we have defined

$$\Sigma_L = \sum_{\mathbf{k},\ell} \frac{|V_{\ell\mathbf{k}}|^2}{2} \left[\left(\varepsilon - \tilde{\varepsilon}_{\ell\mathbf{k}}\right)^{-1} + \left(\varepsilon + \tilde{\varepsilon}_{\ell\mathbf{k}}\right)^{-1}\right] \tag{4.23}$$

and

$$\mu_0 = eV_g - \sum_{\mathbf{k},\ell} \frac{|V_{\ell\mathbf{k}}|^2}{2} \left[\left(\varepsilon - \tilde{\varepsilon}_{\ell\mathbf{k}}\right)^{-1} - \left(\varepsilon + \tilde{\varepsilon}_{\ell\mathbf{k}}\right)^{-1}\right]. \tag{4.24}$$

If the leads are symmetrically coupled to the dot, which is the case here, the sum in ℓ results only in a factor of 2.

The procedure described above has to be repeated for all the dot Majorana Green's functions. As a result, we obtain a system of coupled equations

$$\begin{cases} \left(\varepsilon - \Sigma_L\right) G_{AdAd}\left(\varepsilon\right) = 2 + i\mu_0 G_{BdAd}\left(\varepsilon\right) - it_0 G_{B1Ad}\left(\varepsilon\right), \\ \left(\varepsilon - \Sigma_L\right) G_{BdAd}\left(\varepsilon\right) = -i\mu_0 G_{AdAd}\left(\varepsilon\right) + it_0 G_{A1Ad}\left(\varepsilon\right), \\ \left(\varepsilon - \Sigma_L\right) G_{BdBd}\left(\varepsilon\right) = 2 - i\mu_0 G_{AdBd}\left(\varepsilon\right) + it_0 G_{A1Bd}\left(\varepsilon\right), \\ \left(\varepsilon - \Sigma_L\right) G_{AdBd}\left(\varepsilon\right) = i\mu_0 G_{BdBd}\left(\varepsilon\right) - it_0 G_{B1Bd}\left(\varepsilon\right), \end{cases} \tag{4.25}$$

which can be rewritten in the matrix form

$$\bar{G}_{dd}(\varepsilon) = \bar{g}_{dd}(\varepsilon) + \bar{g}_{dd}(\varepsilon) W_0^{\dagger} \bar{G}_{1d}(\varepsilon). \tag{4.26}$$

In the equation above $G_{ij}(\varepsilon)$ is the 2×2 matrix of Majorana Green's functions

$$\bar{G}_{ij}(\varepsilon) = \begin{pmatrix} G_{AiAj}(\varepsilon) & G_{AiBj}(\varepsilon) \\ G_{BiAj}(\varepsilon) & G_{BiBj}(\varepsilon) \end{pmatrix}, \tag{4.27}$$

$\bar{g}_{dd}(\varepsilon)$ is the Green's function of the system dot+leads

$$\bar{g}_{dd}(\varepsilon) = \left[\mathbf{I}_{2\times2} - \bar{g}_{d}(\varepsilon) V_0(\varepsilon)\right]^{-1} \bar{g}_{d}(\varepsilon), \tag{4.28}$$

with $\bar{g}_d(\varepsilon) = 2(\varepsilon - \Sigma_L)^{-1} \mathbf{I}_{2\times2}$ and

$$V_0 = \frac{1}{2}\begin{pmatrix} 0 & i\mu_0 \\ -i\mu_0 & 0 \end{pmatrix}. \tag{4.29}$$

The 2×2 matrix W_0 plays the role of an effective coupling in the Majorana representantion

$$W_0 = \frac{1}{2}\begin{pmatrix} 0 & -it_0 \\ it_0 & 0 \end{pmatrix}, \tag{4.30}$$

see Fig. 4.2.

The solution of Eq (4.26) with $t_0 = 0$ corresponds to the first step of our recursive method, i.e., the exact dot Green's function in the presence of the leads. Similarly to this equation, we can also calculate the Green's function for the first chain site given by

$$\bar{G}_{11}(\varepsilon) = \tilde{g}_{11}(\varepsilon) + \tilde{g}_{11}(\varepsilon) W^{\dagger} \bar{G}_{21}(\varepsilon). \tag{4.31}$$

Notice that Eqs. (4.26) and (A.9) have the same form; therefore it is possible to determine the local Majorana Green's function for an arbitraty site of the chain. In (A.9) for $j = 1, \ldots, N$ we have

$$\tilde{g}_{jj} = \left[\mathbf{I}_{2\times2} - \bar{g}_{jj}(\varepsilon) W_0 \bar{g}_{dd}(\varepsilon) W_0^{\dagger}\right]^{-1} \bar{g}_{jj}, \tag{4.32}$$

with $\bar{g}_{jj} = \left[\mathbf{I}_{2\times2} - \bar{g}_j(\varepsilon) V\right]^{-1} \bar{g}_j(\varepsilon)$ and $\bar{g}_j(\varepsilon) = 2/\varepsilon$. Finally, the effective couplings V and W

are given by

$$V = \frac{1}{2}\left(\begin{array}{cc} 0 & i\mu \\ -i\mu & 0 \end{array}\right) \text{ and } W = \frac{1}{4}\left(\begin{array}{cc} 0 & i(\Delta+t) \\ i(\Delta-t) & 0 \end{array}\right). \tag{4.33}$$

We stress that in this process there are no approximations. The Green's function of each site is numerically exact. A question that could be raised is: at the end how do we determine the dot Green's function since we are only adding sites and calculating their Green's functions due to the rest of the chain? The answer is quite simple. We iterate backwards, i.e., the first step begins with the Green's function of the n-th site. In practice we consider a chain with 60.000 sites.

4.3 Results

Based on the calculation of the dot LDOS and the conductance, in this section we present and discuss our main findings: the leakage of the Majorana zero mode of the wire into the dot and the pinning of this end mode at the Fermi energy of the leads. We explore these results by suggesting three experimental ways of probing this leaked Majorana mode: (i) by electrically tuning the coupling between the dot and the wire t_0 and measuring the two-terminal conductance G for $\varepsilon_{\text{dot}}(V_g) \neq \varepsilon_F$, we should be able to observe the appearance of the Majorana signature as a peak of magnitude $e^2/2h$ where otherwise we would have $G = 0$; (ii) the other possibility would be to vary V_g (ε_{dot}) from far below to far above the Fermi energy of the leads and measure G to see essentially a plateau at $e^2/2h$; (iii) the third proposal consists in measuring G while driving the wire through a non-topological/topological phase transition, which could be carried out, e.g., by varying the chemical potential of the wire.

4.3.1 Some analytical results

First let us study some particular cases in which it is possible to obtain analytical solutions to our problem. We first take $t_0 = 0$ and obtain the well-known case of a spinless single-level dot coupled to leads. In the Majorana representation we simply have to solve Eq. (4.28), which give us the result

$$G_{dd}(\varepsilon) = \frac{1}{\varepsilon - \varepsilon_{\text{dot}} - \Lambda(\varepsilon) + i\Gamma_L(\varepsilon) + i\eta}, \tag{4.34}$$

where $\Lambda\left(\varepsilon\right)=2|V_L|^2\mathrm{Re}G_L\left(\varepsilon\right)$ shifts the pole of the dot Green's function and $\Gamma_L\left(\varepsilon\right)=2\pi|V_L|^2\rho_L\left(\varepsilon\right)$ broadens the dot level; $G_L\left(\varepsilon\right)$ is the Green's function of the leads and $\rho_L\left(\varepsilon\right)$ their DOS. For more details see Appendix A. Note that the equation above is already the dot Green's function of Eq. (4.12), i.e., the electronic version. We can now employ G_{dd} to calculate the dot LDOS and the conductance G of the system,

$$\begin{aligned}\rho_{\mathrm{dot}}\left(\varepsilon\right) &= -\frac{1}{\pi}\mathrm{Im}G_{dd}\left(\varepsilon\right)\\ &= \frac{1}{\pi}\frac{\Gamma_L^2}{\left(\varepsilon-\varepsilon_{\mathrm{dot}}-\Lambda_L\right)^2+\Gamma_L^2}\end{aligned} \tag{4.35}$$

and

$$G\left[e^2/h\right]=\frac{\Gamma_L^2}{\left(\varepsilon_{\mathrm{dot}}+\Lambda_L\left(0\right)\right)^2+\Gamma_L^2}. \tag{4.36}$$

Equation (4.36) is the limit of (4.15) at zero temperature.

Both equations above have the form of a Lorentzian centered at $\varepsilon_{\mathrm{dot}}+\Lambda_L$ and at Λ_L, respectively, and whose half-width at half-maximum is given by Γ_L (in this case the half-width is 1 since we have normalized the energy axis).

According to realistic simulations (104, 105) and experiments (1), in our numerical results we assume $t=10$ meV and $\Gamma_L=4\times10^{-3}t=40$ μeV. The coupling $V_L=0.1t$ is chosen such that the expression for Γ_L is satisfied. Here we also set $\varepsilon_F=0$. In Fig. 4.4, we plot ρ_{dot} as a function of the energy ε for several values of $\varepsilon_{\mathrm{dot}}$. As we just mentioned, when we vary $\varepsilon_{\mathrm{dot}}$ the location of the peaks changes (Λ_L is negligible). The conductance can be seen in Fig. 4.5, in which we observe a single peak of height e^2/h (59, 106) at $\varepsilon_{\mathrm{dot}}=0$, when the dot level is on resonance with the Fermi level of the leads.

Another situation in which we can obtain an analytical result for the conductance happens when $\Delta=0$. This is what we call trivial phase, because there is no induced superconductivity in the wire, which actually behaves as a third normal lead. Hence the problem we have to solve consists simply of a dot, whose Green's function has already been renormalized by the source and drain leads [Eq. (4.34)], coupled to a contact modeled by a tight-binding chain with hopping parameter $t/2$ and Green's function $g_1\left(\varepsilon\right)$.

The equation of motion technique applied to this problem yields the following system of

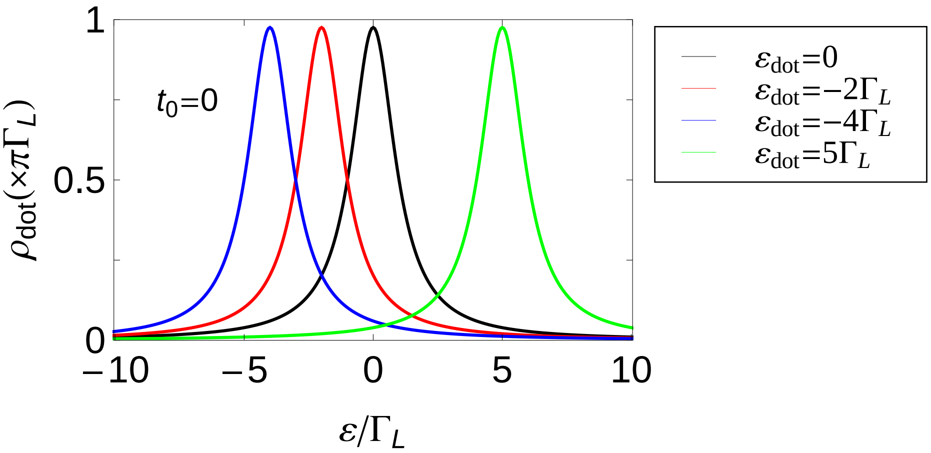

Figure 4.4 – Density of states of a dot $\rho_{\rm dot}$ coupled to source and drain leads as a function of the energy ε. The four curves correspond to different values of $\varepsilon_{\rm dot}$: black $\varepsilon_{\rm dot}=0$, red $\varepsilon_{\rm dot}=-2\Gamma_L$, blue $\varepsilon_{\rm dot}=-4\Gamma_L$ and green $\varepsilon_{\rm dot}=5\Gamma_L$.

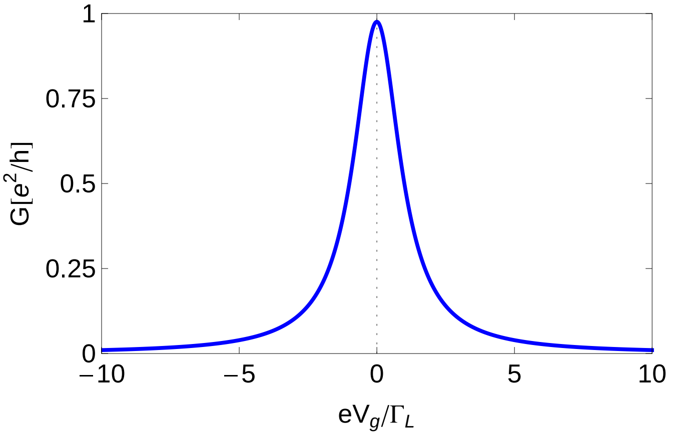

Figure 4.5 – Conductance of the system as a function of the applied gate potential. Single peak centered at $\varepsilon_{\rm dot}=0$ when the dot level is aligned with the Fermi level of the leads.

equations

$$\begin{cases} \tilde{G}_{dd}(\varepsilon) = g_d(\varepsilon) + g_d(\varepsilon)\, t_0 \tilde{G}_{1d}(\varepsilon), & \text{(a)} \\ \tilde{G}_{1d}(\varepsilon) = g_1(\varepsilon)\, t_0 \tilde{G}_{dd}(\varepsilon), & \text{(b)} \end{cases} \tag{4.37}$$

in which $g_d(\varepsilon)$ is given by (4.34) and $g_1(\varepsilon)$ by

$$g_1(\varepsilon) = 2\left(\frac{1-\sqrt{1-g_0(\varepsilon)^2 t^2}}{g_0(\varepsilon)\, t^2}\right), \tag{4.38}$$

with $g_0(\varepsilon) = 1/(\varepsilon - \mu + i\eta)$ the free electronic Green's function. Note that (4.38) can be obtained from (A.12) by replacing $t \to t/2$ and $\omega \to \varepsilon - \mu$.

Substituting (4.37b) into (4.37a) we have

$$\tilde{G}_{dd}(\varepsilon) = \frac{1}{\varepsilon - \varepsilon_{\text{dot}} - \Sigma_{\text{chain}}(\varepsilon) - \Sigma_L(\varepsilon) + i\eta}, \tag{4.39}$$

where $\Sigma_L(\varepsilon) = \Lambda_L(\varepsilon) - i\Gamma_L(\varepsilon)$ is due to the source and drain leads and $\Sigma_{\text{chain}}(\varepsilon) = g_1(\varepsilon)t_0^2$. If we rewrite $\Sigma_{\text{chain}} = \Lambda_{\text{chain}} - i\Gamma_{\text{chain}}$, $\Lambda_{\text{chain}} = \text{Re}\Sigma_{\text{chain}}$ and $\Gamma_{\text{chain}} = -\text{Im}\Sigma_{\text{chain}}$, the dot Green's function $\tilde{G}_{dd}$ is given by

$$\tilde{G}_{dd} = \frac{(\varepsilon - \varepsilon_{\text{dot}} - \Lambda_L - \Lambda_{\text{chain}}) - i(\Gamma_L + \Gamma_{\text{chain}})}{(\varepsilon - \varepsilon_{\text{dot}} - \Lambda_L - \Lambda_{\text{chain}})^2 + (\Gamma_L + \Gamma_{\text{chain}})^2}. \tag{4.40}$$

From the expression above we can determine $\rho_{\text{dot}}(\varepsilon)$,

$$\rho_{\text{dot}}(\varepsilon) = \frac{1}{\pi}\frac{(\Gamma_L + \Gamma_{\text{chain}})}{(\varepsilon - \varepsilon_{\text{dot}} - \Lambda_L - \Lambda_{\text{chain}})^2 + (\Gamma_L + \Gamma_{\text{chain}})^2} \tag{4.41}$$

and the conductance

$$G\left[e^2/h\right] = \frac{\Gamma_L(\Gamma_L + \Gamma_{\text{chain}})}{(\varepsilon_{\text{dot}} + \Lambda_L + \Lambda_{\text{chain}})^2 + (\Gamma_L + \Gamma_{\text{chain}})^2}. \tag{4.42}$$

For $|\mu| < t$ and $\varepsilon_{\text{dot}} = 0$ we have

$$\begin{cases} \Lambda_L(\varepsilon = 0) = 0, \\ \Lambda_{\text{chain}} = -\dfrac{2t_0^2}{t^2}\mu, \\ \Gamma_{\text{chain}} = \dfrac{2t_0^2}{t^2}\sqrt{t^2 - \mu^2}, \end{cases} \tag{4.43}$$

what results in

$$G\left[e^2/h\right] = \frac{\Gamma_L\left(\Gamma_L + \frac{2t_0^2}{t^2}\sqrt{t^2 - \mu^2}\right)}{\frac{4t_0^4}{t^4}\mu + \left(\Gamma_L + \frac{2t_0^2}{t^2}\sqrt{t^2 - \mu^2}\right)^2}. \tag{4.44}$$

In the following section, we discuss this last expression in the context of the emerging Majorana zero mode in the dot.

In Fig. 4.6 we plot the DOS of a 1D tight-binding chain as a function of the energy ε for $t_0 = t/2$ and $\Delta = \varepsilon_{\text{dot}} = \mu = 0$. The dot-leads coupling V_L is zero, thus the dot is viewed as a normal site of the chain, the site on the edge. The dashed red curve corresponds to the known DOS of an infinite tight-binding chain ρ_{bulk} and the solid black line represents the DOS for the site on the edge ρ_{edge}, which can be obtained from Eq. (4.41). When we turn on the superconductor pairing amplitude ($\Delta = 2$ meV) such that the wire undergoes a phase transition (non-topological/topological), see Fig. 4.7, we can observe that ρ_{bulk} is now fully gapped and a zero-energy peak, which corresponds to the Majorana zero mode of the chain, emerges in the DOS of the site on the edge $\rho_{\text{edge}} = \rho_1$.

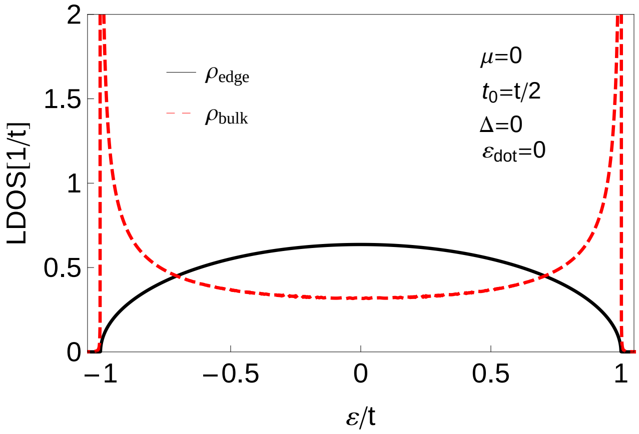

Figure 4.6 – Density of states of a usual tight-binding chain. The dot can be viewed as a site of the chain since $V_L = 0$ and $t_0 = t/2$. The two curves represent the DOS for a site on the edge ρ_{edge} (solid black line) and in the bulk ρ_{bulk} (dashed red line).

Still considering the trivial phase ($\Delta = 0$), we emphasize that when the dot level is coupled to a regular fermionic mode, see Eq. (4.41), the dot energy level simply splits and broadens (if coupled to a continuum). As we shall see, this strikingly contrasts with the topological phase, in which the dot level couples to the Majorana zero mode of the wire and remains ‘locked’ at the Fermi energy of the leads if we vary V_g.

4.4 Numerical results

The numerical results we show here were obtained via the recursive Green’s function method described in section 4.2. Just as a reminder, our choice of parameters was based on realistic simulations and experiments (1, 104, 105). We assume $\varepsilon_F = 0$, the hopping parameter $t = 10$ meV, the electronic broadening level $\Gamma_L = 40\ \mu$eV and the dot-leads coupling $V = 0.1t$.

Figures 4.8 (a) and 4.8 (b) show the LDOS as a function of the energy ε of the dot ρ_{dot} and of the first site of the Kitaev chain ρ_1 for $\varepsilon_{\text{dot}} = -5\Gamma_L$ and different values of the dot-wire coupling t_0. The black curve in ρ_{dot} corresponds to the usual single peak at $\varepsilon = \varepsilon_{\text{dot}}$ of half-

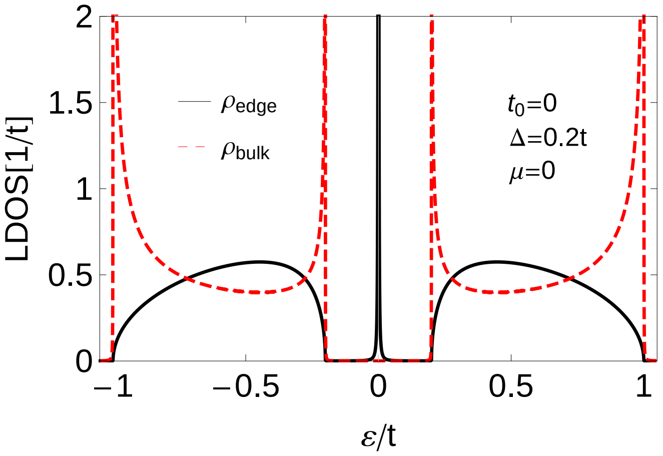

Figure 4.7 – Local density of states for the site on the edge ρ_{edge} (solid black line) and in the bulk ρ_{bulk} (dashed red line) of the Kitaev chain as functions of the energy with $t_0 = 0$, $\Delta = 0.2t$ and $\mu = 0$.

width Γ_L [see Eq. (4.35) and Fig. 4.4]. Notice that since the dot level is far away from the Fermi energy of the leads, the DOS at $\varepsilon = 0$ is practically null. As we increase t_0, however, an additional peak at $\varepsilon = 0$ emerges in ρ_{dot} (red dashed line) while the magnitude of the zero-energy peak corresponding to a Majorana end mode at $t_0 = 0$ observed in ρ_1 decreases. These two features can be better appreciated if we look at the blue $t_0 = 10\Gamma_L$ and green $t_0 = 20\Gamma_L$ curves. The central peak in ρ_1 has decreased up to an almost zero DOS whereas in ρ_{dot} it has reached its maximum height 0.5 (in units of $\pi\Gamma_L$). Lateral peaks emerge in ρ_1, guaranteeing that if we integrate it over the energy we obtain 1. The same happens to ρ_{dot}, the peak previously centered at $\varepsilon = \varepsilon_{\text{dot}}$ for $t_0 = 0$, moves to lower energies and has its height decreased, in addition a new peak appears for higher energies.

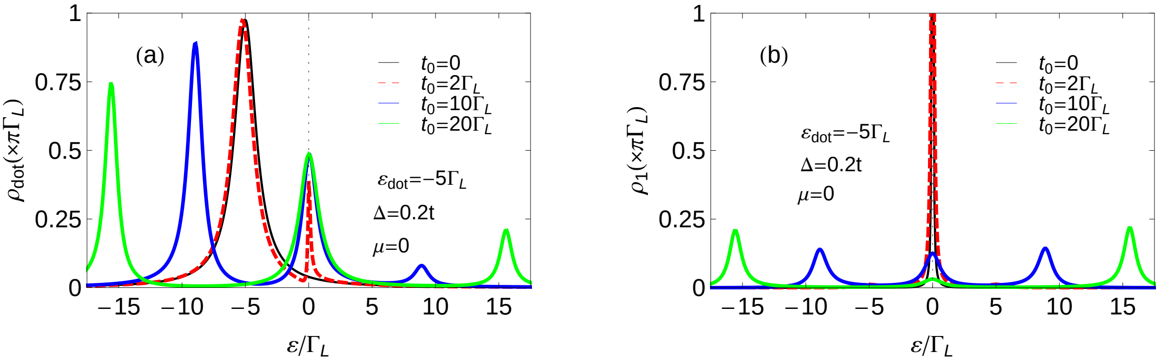

Figure 4.8 – Dot (a) and first chain site (b) LDOS, ρ_{dot} and ρ_1, respectively, as functions of the energy ε for several values of t_0, $\varepsilon_{\text{dot}} = -5\Gamma_L$, $\Delta = 0.2t$ and $\mu = 0$.

The important point we want to stress is that the Majorana zero mode initially located at the first site of the chain leaks into the quantum dot. One of the signatures of this leakage is the emergence of the zero mode in ρ_{dot} at the same time of its suppression in ρ_1. This contrast can be observed in Fig. 4.9, in which we plot $\rho_{\text{dot}(1)}/\rho_{\text{dot}(1)}^{\text{max}}$ calculated at $\varepsilon = 0$ as a function of t_0, with $\rho_{\text{dot}(1)} = \max[\rho_{\text{dot}(1)}(\varepsilon = 0, t_0)]$. As we can see ρ_{dot} goes from its almost zero DOS to one, the opposite happening to ρ_1 thus evidencing that the Majorana escaped to the dot.

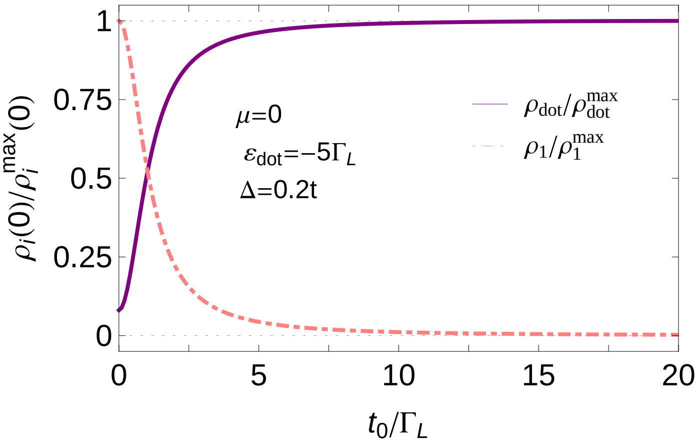

Figure 4.9 – $\rho_{\text{dot}}/\rho_{\text{dot}}^{\text{max}}$ (solid purple line) and $\rho_1/\rho_1^{\text{max}}$ (dot-dashed pink line) at $\varepsilon = 0$ as functions of the dot-wire coupling t_0, with $\rho_{\text{dot}(1)} = \max[\rho_{\text{dot}(1)}(\varepsilon = 0, t_0)]$

.

We can ask ourselves what happens to the DOS of the other sites direct or indirectly connected to the first site of the Kitaev chain. Is there some leakage? Below we show the DOS of the second ρ_2 [Figs. 4.10 (a) and (b)] and third ρ_3 [Figs. 4.11 (a) and (b)] sites as functions of ε. We can see that similarly to ρ_{dot}, ρ_2 has no zero-energy peak when $t_0 = 0$, but as we vary t_0 the

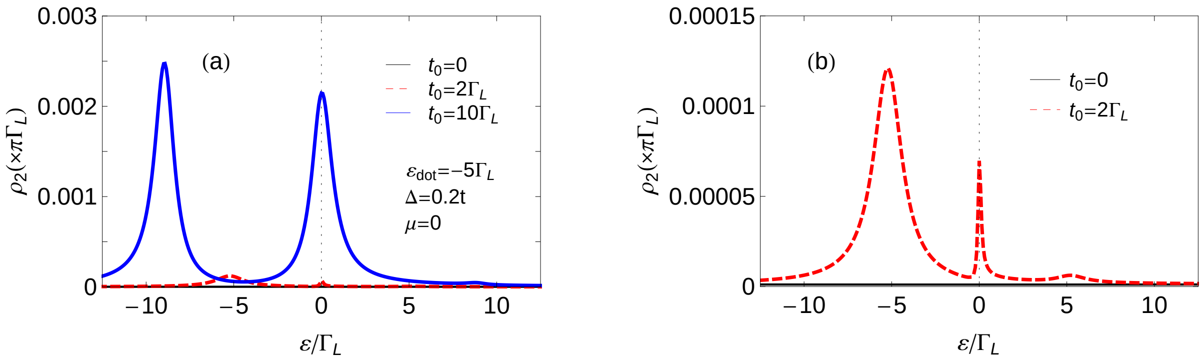

Figure 4.10 – LDOS of the second site ρ_2 in the Kitaev chain as a function of ε for several values of t_0 (a). In (b) we show a blowup of ρ_2 to emphasize the small magnitude of the peaks.

DOS increases at $\varepsilon = 0$. As for ρ_3, it resembles the DOS of the first site of the chain. We note, however, that the magnitude of the peaks in ρ_2 and ρ_3 is at least one order of magnitude smaller than those of ρ_{dot} and ρ_1, respectively. [see blowups in 4.10 (b) and 4.11 (b)]. The curves for ρ_2 (ρ_3) being similar to those for ρ_{dot} (ρ_1) is connected to parity. For j odd there is an extra mode (zero mode) that has to be symmetrically "accommodated" in the DOS. Just for emphasis, we

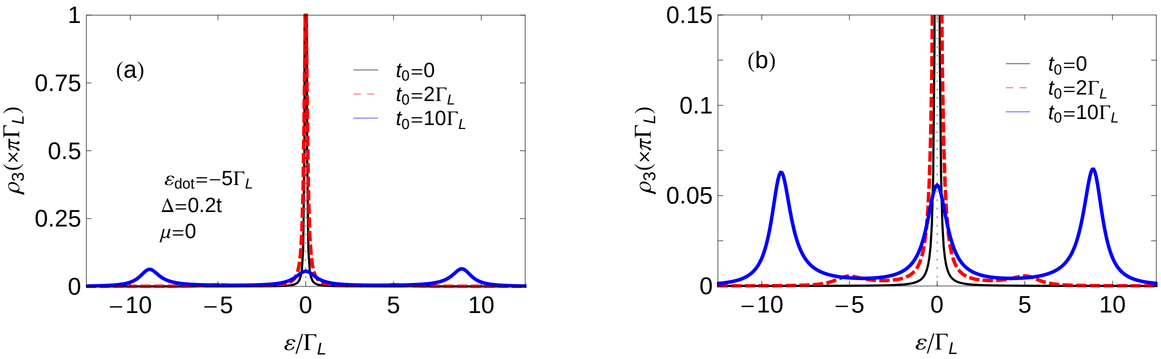

Figure 4.11 – LDOS of the third site ρ_3 in the Kitaev chain as a function of ε for different values of t_0 (a). In (b) we show a blowup of ρ_2 to emphasize the small magnitude of the peaks.

take $t_0 = 100\Gamma_L$ and plot ρ_{dot} (solid black line), ρ_1 (dashed red line) and the DOS for a site in the middle of the chain (solid blue line) for the same set of parameters as in Fig. 4.8. The curves can be seen in Fig. 4.12 and we observe that the only relevant contribution to the DOS at $\varepsilon = 0$ comes from the dot.

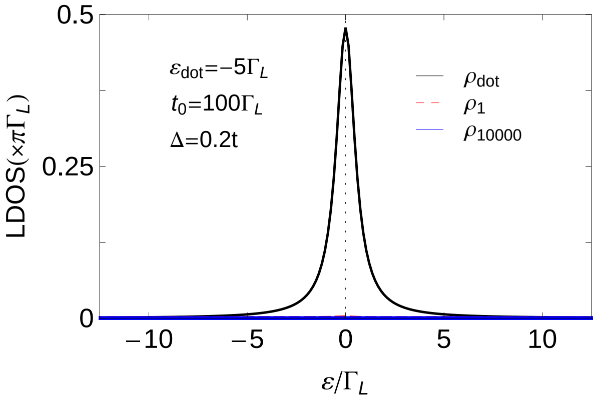

Figure 4.12 – LDOS for the dot, first site and a site in the middle of the chain. The Majorana zero mode has completely leaked to the dot for $t_0 = 100\Gamma_L$.

The other intrinsic feature supporting the presence of the Majorana in the dot, as we shall see, is the pinning of the zero mode at the Fermi level of the leads and its characteristic value of 0.5, either for the DOS (in units of $\pi\Gamma_L$) and for the conductance (in units of e^2/h).

In Fig. 4.13 we have a color map plot of the dot LDOS vs ε and eV_g for the wire in its topological phase ($\Delta > 0$ and $|\mu| < t$). Keeping eV_g constant, e.g., at eV_{g1} (dot-dashed yellow

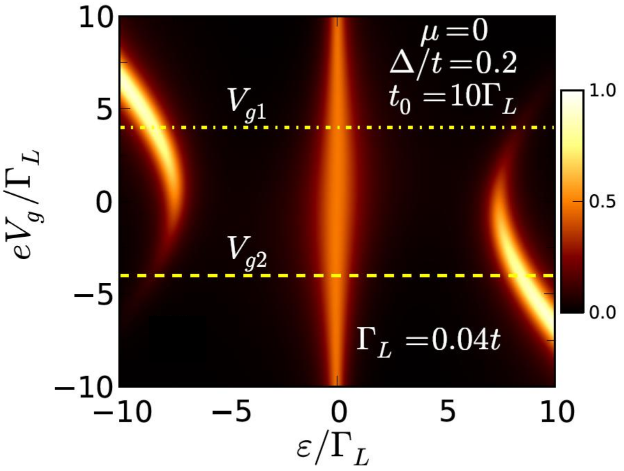

Figure 4.13 – Color map of the electronic density of states as a function of ε and eV_g. The two horizontal lines at eV_{g1} (dot-dashed yellow line) and eV_{g2} (dashed yellow line) represent plots similar to those seen in Fig. 4.8.

line) or eV_{g2} (dashed yellow line), we observe three bright regions that correspond to the three peaks seen in ρ_{dot}, similarly to those in Fig. 4.8 (see for example the blue curve for $t_0 = 10\Gamma_L$). It is more interesting, however, if we set $\varepsilon = 0$ and look along the vertical axis. We can see that the central peak does not change essentially for either $eV_g > 0$ and $eV_g < 0$. Even more surprising is that this peak is pinned at $\varepsilon = \varepsilon_F = 0$ for the entire range of eV_g shown in the plot. This feature resembles in part the Kondo resonance, whose peak of amplitude $\pi\Gamma_L$ remains unchanged only for ε_{dot} above $\varepsilon_F = 0$ (remember that $\varepsilon_{\text{dot}} = -eV_g$). Figure 4.14 shows a sketch of the Majorana (left) and Kondo (right) resonances at $\varepsilon_F = 0$. When the dot level is above ε_F there is a peak at $\varepsilon = 0$ only in the Majorana case.

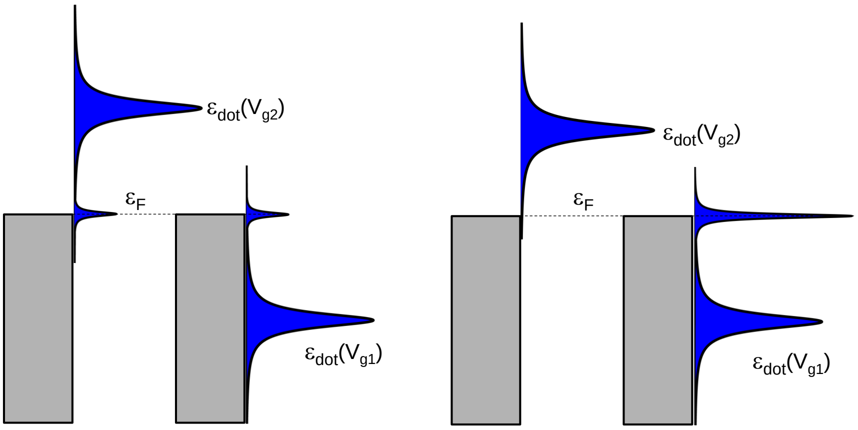
$\varepsilon_{\text{dot}}(V_{g2})$
ε_F
$\varepsilon_{\text{dot}}(V_{g1})$
$\varepsilon_{\text{dot}}(V_{g2})$
ε_F
$\varepsilon_{\text{dot}}(V_{g1})$

Figure 4.14 – Sketch of the dot LDOS for the Majorana (left) and Kondo (right) cases.

.

A possibility to observe the Majorana end mode experimentally and distinguish its zero bias peak unambiguously from that of Kondo would consist in measuring the conductance G through the dot while varying the applied gate voltage eV_g. What we would see is shown in Fig. 4.15 for different values of the chemical potential μ. The solid lines correspond to $\Delta = 0.2t$ and the dashed ones to $\Delta = 0$. For the wire is in its trivial phase $\Delta = 0$ and/or $|\mu| > t$ ($\mu = 1.75t$ for example), we can see a single peak in the conductance G, which occurs when the dot level coincides with the Fermi level. Note that the peaks in this case are slightly shifted from zero. This is due to the real part of the wire Green's function, which shifts the dot level, see Eq. (4.42) derived for $\Delta = 0$. In the topological phase ($\Delta \neq 0$ and $|\mu| < t$) we observe an almost constant

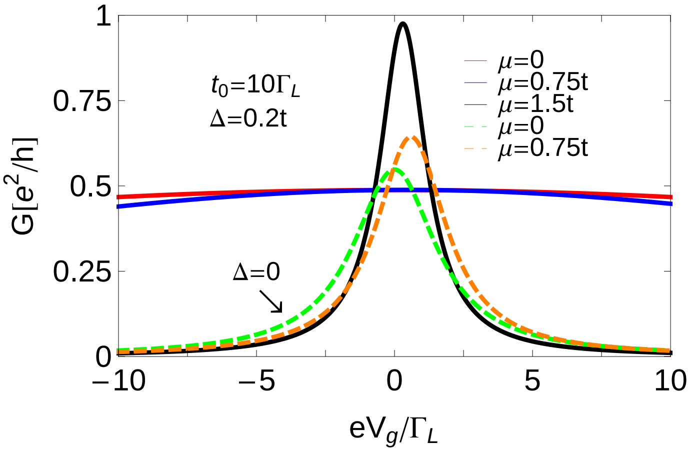

Figure 4.15 – Two-terminal conductance G of the system as a function of the applied gate voltage eV_g. The solid curves correspond to $\Delta = 0.2t$ and the dashed ones to $\Delta = 0$ for distinct μ.

value of $e^2/2h$ for the conductance for $eV_g > 0$ and $eV_g < 0$. This is in contrast with the Kondo case, which presents a plateau at e^2/h only for ε_{dot} below ε_F.

Let us now analyze the contribution of each Majorana A and B to the dot and first chain site density of states $\mathscr{A}$ and $\mathscr{B}$, respectively. Figures 4.16 (a) and 4.16 (b) show a color map plot of $\mathscr{A}_{\text{dot}}$ and $\mathscr{B}_{\text{dot}}$ vs ε and eV_g for the same set of parameters as in Fig. 4.15. We observe that there is a zero-energy peak only in (a) indicating that the pinning seen in the conductance of Fig. 4.15 is due to the dot Majorana A. In (b) we see only lateral peaks at $\varepsilon \approx \pm 7\Gamma_L$ affected by the coupling between the dot Majorana B and the wire. The Majorana A of the first chain site is as well affected by the coupling with B_{dot}. Its DOS also exhibits peaks at $\varepsilon = \pm 7\Gamma_L$ but no zero-energy peaks, Fig. 4.16 (c). At last, we observe that there are no zero modes in $\mathscr{B}_1$ either, what lead us to another evidence of the Majorana being in the dot.

We now discuss another scenario for possibly probing the Majorana bound state in the dot. We look at the conductance G as a function of the chemical potential μ of the wire. When

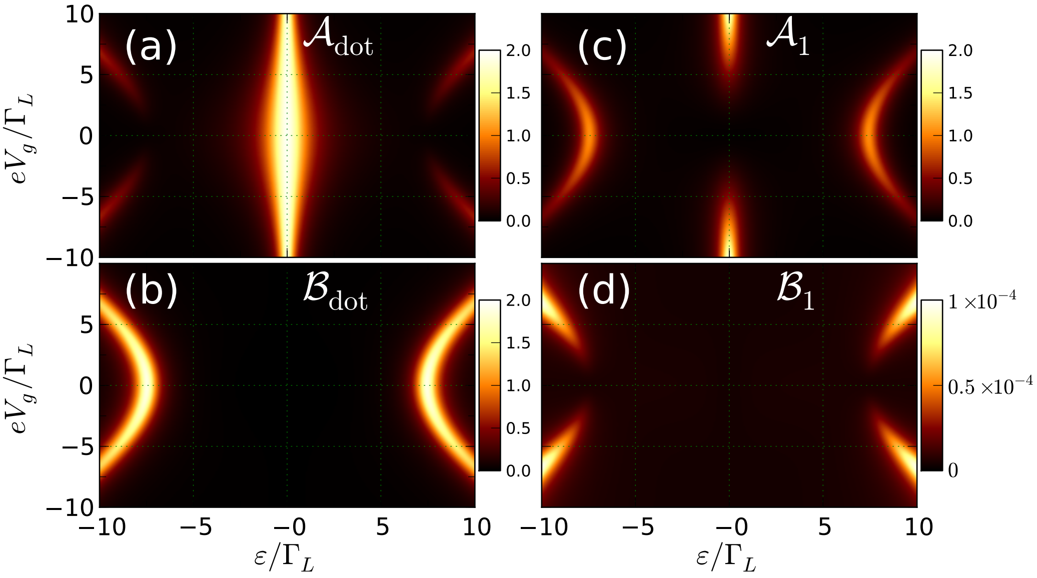

Figure 4.16 – Color map of the Majorana density of states as a function of ε and eV_g of the dot Majoranas A (a) and B (b) and of the first site of the Kitaev chain, (c) and (d), respectively.

we vary μ, the wire undergoes a non-topological to topological phase transition. As we have already mentioned, the nontopological or trivial phase is characterized by $\Delta = 0$ and any value of μ *or* $|\mu| > t$ for any value of Δ. The topological phase, on the contrary, has $\Delta \neq 0$ and $|\mu| < t$. Figure 4.17 (a) shows G vs μ for $\Delta = 0.2t$ and $t_0 = 10\Gamma_L$ for distinct values of $\varepsilon_{\rm dot}$. For $\varepsilon_{\rm dot} = 0$ and $|\mu| \gg t$, the conductance arising from the single dot level at ε_F tends to the value e^2/h. When $\varepsilon_{\rm dot}$ increases, however, the conductance goes to zero since the dot level is

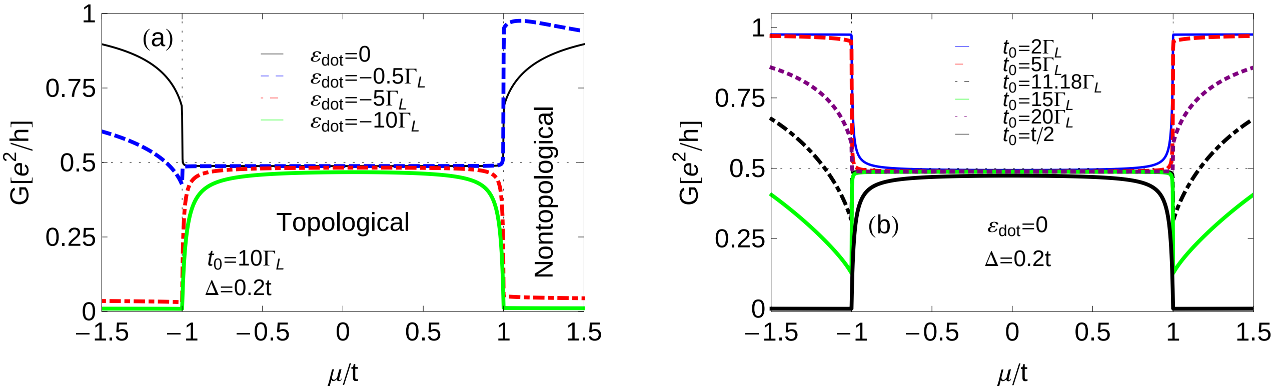

Figure 4.17 – Conductance G as a function of the chemical potential μ. In (a) we fix the dot-wire coupling t_0 and vary $\varepsilon_{\rm dot}$ and in (b) we set $\varepsilon_{\rm dot} = 0$ for several values of t_0, both for $\Delta = 0.2t$.

no longer on resonance with the Fermi level of the leads, the same happening for the trivial phase [see Fig. 4.18 (a)]. The situation in which μ is tuned such that $|\mu| < t$, G suddenly goes to the value $e^2/2h$ because of the Majorana mode in the dot, and remains locked for the entire range of μ and any value of $\varepsilon_{\rm dot}$. In 4.17 (b) we have $\varepsilon_{\rm dot} = 0$ and several values of t_0. The non-trivial case exhibits again the pinning of G at $e^2/2h$. The trivial phase, on the other hand, has the conductance decreased as the coupling t_0 increases, see Fig. 4.18 (b). This is due to the self energy arising from the chain that shifts the dot level.

The curves shown in Fig. 4.18 are for $\Delta = 0$ and the same set of parameters as in Fig. 4.17. They can be obtained from Eq. (4.42). In (a) [(b)] we observe that when $|\mu| < t$ for a fixed t_0 (ε_{dot}) the conductance is very sensitive to ε_{dot} (t_0) as compared to its analogous in Fig. 4.17 (a) [(b)]. This dependence can be directly seen in the analytical expression for G (4.44), e.g., for $\mu = 0$ it reduces to

$$G\left[e^2/h\right] = \frac{\Gamma_L}{\Gamma_L + \Gamma_{\text{chain}}}, \tag{4.45}$$

where $\Gamma_{\text{chain}} = 2t_0^2/t$. The wire in this case behaves as a normal third contact.The kinks seen in the curves are due to the discontinuity of the chain self energy at $\mu = \pm t$.

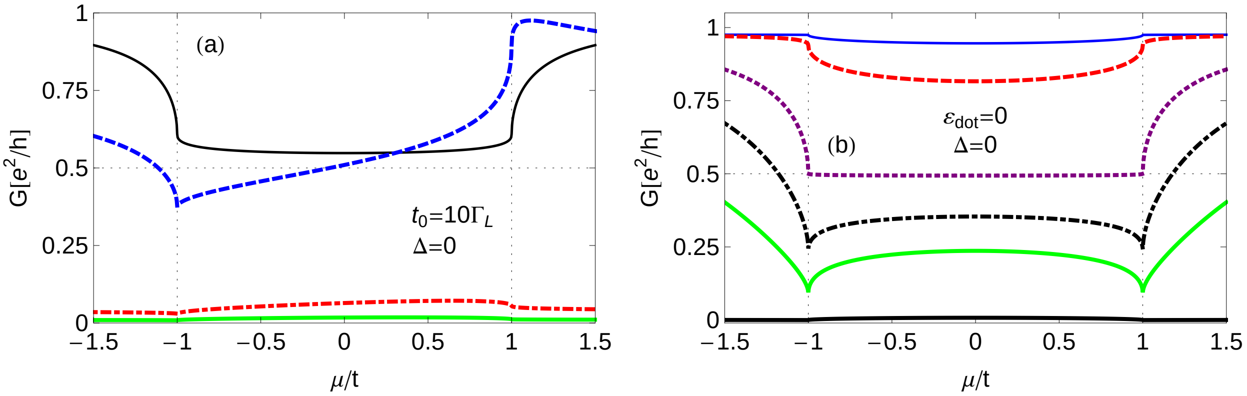

Figure 4.18 – Conductance G as a function of μ for $\Delta = 0$. Panels (a) and (b) show, respectively, curves for $t_0 = 10\Gamma_L$ and different values of ε_{dot} and $\varepsilon_{\text{dot}} = 0$ for several values of t_0. The parameters are the same as those in Fig. 4.17.

A surprising aspect of the conductance for $\varepsilon_{\text{dot}} = 0$ is that if we search a value of t_0 to which G goes to the value $e^2/2h$, we find that at $t_0 = 11.18\Gamma_L$ the curve for the trivial case is indistinguishable from that of $\Delta \neq 0$. In this sense, the value $G = e^2/2h$, first found in Ref. (102) in a similar setup as ours but only for $\varepsilon_{\text{dot}} = \varepsilon_F = 0$, is not per se a proof of a Majorana zero mode in conductance measurements. As we have shown above, we have to vary either the level of the dot or the dot-wire coupling to be able to differentiate the trivial from the non-trivial phases.

Finally, we discuss another interesting case: $\Delta = t$. This is the situation in which the Majoranas A_1 and B_N are completely decoupled from the rest of the chain (see 3.1), A_1 is only

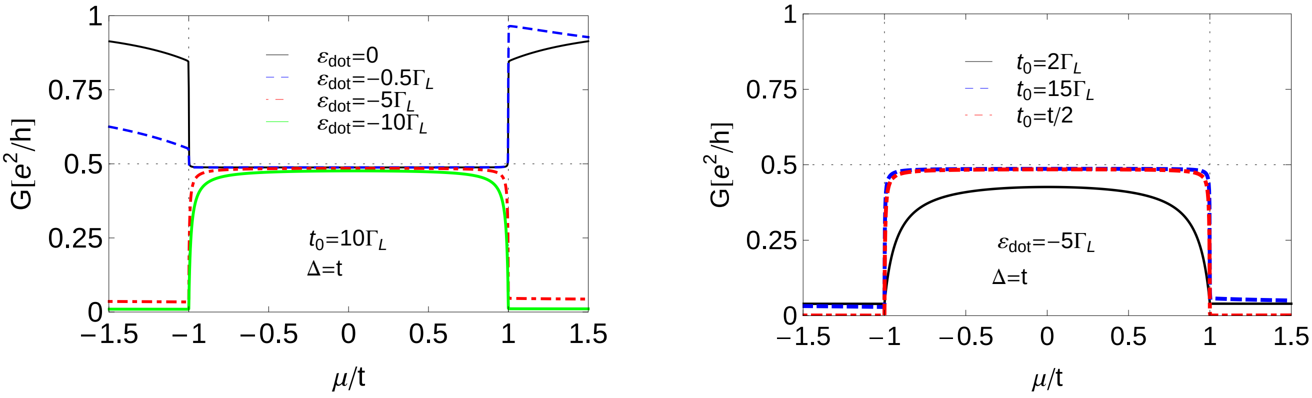

Figure 4.19 – Conductance G as a function of μ for $\Delta = t$. In (a) we set $t_0 = 10\Gamma_L$ and vary $\varepsilon_{\rm dot}$. In (b) we fix $\varepsilon_{\rm dot} = -5\Gamma_L$ for different values of t_0.

coupled to $B_{\rm dot}$ through t_0. In Fig. 4.19 (a) we fix $t_0 = 10\Gamma_L$ and plot G as a function of μ for different values of $\varepsilon_{\rm dot}$. We can observe the same kind of behavior seen in Fig. 4.17 (a). Nevertheless, the conductance for a small value of $\varepsilon_{\rm dot}$ and $|\mu| > t$ seems to go faster to the asymptotically value e^2/h since the hopping parameter t has a higher order effect on the dot. Figure 4.19 (b) shows G vs μ for $\varepsilon = -5\Gamma_L$ and several values of t_0. The dot level being off resonance $\varepsilon_{\rm dot} \neq \varepsilon_F$ leads to a zero conductance in the trivial phase. On the other hand, for $|\mu| < t$ G is pinned at $e^2/2h$ due to the leaked Majorana zero mode in the dot. Note that this feature is more outstanding when we increase the dot-wire coupling.

Our final remark concerns the Kondo resonance. Is it possible to rule out the zero-bias Kondo peak in conductance measurements in systems like ours? First of all, the system we described does not support the Kondo effect (non-interacting system), but we believe that even in setups, in which it may be present, the symmetry of the dot-Majorana resonance with respect to $\varepsilon_{\rm dot}$ above or below ε_F could be used to distinguish the Majorana zero bias peak from that of Kondo. For a discussion on the Kondo effect in the Majorana context see Ref. (107).

Chapter 5

Conclusions

In this thesis, we have investigated quantum transport in two different systems: (i) a ferromagnetic STM tip coupled to a NM host surface with a single adsorbed atom, and (ii) a single-level quantum dot coupled to source and drain leads and connected to a Kitaev wire.

In the STM setup, electrons can tunnel directly from the tip to the surface or via the adatom. Since the tip is ferromagnetic and the host surface (metal or semiconductor) is non-magnetic we observe a spin-diode effect when the adatom is in the regime of single occupancy. This effect leads to an unpolarized current for direct bias ($V > 0$) and polarized current for reverse ($V < 0$) bias voltages, if the tip is nearby the adatom. We used the nonequilibrium Keldysh technique to derive the spin-polarized current in the system and analyze the interplay between the lateral displacement of the tip and the intra adatom Coulomb interaction on the spin-diode effect. As the tip moves away from the adatom the spin-diode effect vanishes and the currents become polarized for both $V > 0$ and $V < 0$. We also showed that there is an imbalance between the up and down spin populations in the adatom, which can be tuned by the tip position and the bias.

In the singly occupied case and direct bias ($V > 0$), the current polarization can vary from zero up to 40% depending on the tip position. For reverse bias, though, the polarization is pinned close to 40% for all tip positions. In the double occupancy regime the current polarization is the same for both forward and reverse biases, with a slight suppression as the tip moves closer to the adatom. Additionally, the adatom magnetization can be tuned by varying the tip position and its sign can switch depending on the bias. Due to the presence of the adatom, we observed spin-resolved Friedel oscillations in the current as the tip moves laterally away from the adatom, thus reflecting the oscillations in the surface LDOS induced by the adatom acting like an effective impurity.

In the Majorana system we have used an exact recursive Green's function approach to calculate the LDOS and the two-terminal conductance G through the quantum dot side-coupled to the Kitaev wire. We have proposed that the calculated conductance can be used as a way of probing the Majorana end mode present in the topological superconducting nanowire represented by the Kitaev chain. As we have shown, by tuning some of the parameters of the system, e.g., the dot-chain coupling or the dot level, via a gate voltage, we found that the end Majorana mode of the wire leaks into the quantum dot thus originating a resonance pinned to the Fermi level of the leads ε_F. In contrast to the usual Kondo resonance arising only for ε_{dot} below ε_F, this unique dot Majorana resonance appears pinned to ε_F even when the gate-controlled energy level ε_{dot} above or below ε_F , provided that the wire is in its topological phase. This leaked Majorana dot mode provides a clear-cut way to probe the Majorana mode of the wire via conductance measurements through the dot.

REFERENCES

1 MOURIK, V.; ZUO, K.; FROLOV, S. M.; PLISSARD, S. R.; BAKKERS, E. P. A. M.; KOUWENHOVEN, L. P. Signatures of Majorana fermions in hybrid superconductor-semiconductor nanowire devices. *Science*, v. 336, n. 6084, p. 1003, 2012. doi: 10.1126/science.1222360.

2 LEIJNSE, M.; FLENSBERG, K. Introduction to topological superconductivity and Majorana fermions. *Semiconductor Science and Technology*, v. 27, n. 12, p. 124003, 2012. doi: 10.1088/0268-1242/27/12/124003.

3 WILCZYNSKI, M.; SWIRKOWICZ, R.; RUDZINSKI, W.; BARNAS, J.; DUGAEV, V. Quantum dots attached to ferromagnetic leads: possibility of new spintronic devices. *Journal of Magnetism and Magnetic Materials*, v. 290-291, p. 209, 2005. doi: 10.1016/j.jmmm.2004.11.184.

4 ENGEL, H.-A.; RECHER, P.; LOSS, D. Electron spins in quantum dots for spintronics and quantum computation. *Solid State Communications*, v. 119, n. 4-5, p. 229, 2001. doi: 10.1016/S0038-1098(01)00110-7.

5 FABIAN, J.; MATOS-ABIAGUE, A.; ERTLER, C.; STANO, P.; ZUTIC, I. Semiconductor spintronics. *Acta Physica Slovaca*, v. 57, n. 4-5, p. 565, 2007. doi: 10.2478/v10155-010-0086-8.

6 JULLIERE, M. Tunneling between ferromagnetic films. *Physics Letters A*, v. 54, n. 3, p. 225, 1975. doi: 10.1016/0375-9601(75)90174-7.

7 BARNAS, J.; FERT, A. Magnetoresistance oscillations due to charging effects in double ferromagnetic tunnel junctions. *Physical Review Letters*, v. 80, n. 5, p. 1058, 1998. doi: 10.1103/PhysRevLett.80.1058.

8 SPIN filtering and spin diode devices in quantum wire systems. *Physica E: Low-dimensional Systems and Nanostructures*, v. 27, n. 3, p. 325, 2005. doi: 10.1016/j.physe.2004.12.008.

9 SOUZA, F. M.; EGUES, J. C.; JAUHO, A. P. Quantum dot as a spin-current diode: A master-equation approach. *Physical Review B*, v. 75, n. 16, p. 165303, 2007. doi: 10.1103/PhysRevB.75.165303.

10 COTTET, A.; BELZIG, W.; BRUDER, C. Positive cross correlations in a three-terminal quantum dot with ferromagnetic contacts. *Physical Review Letters*, v. 92, n. 20, p. 206801, 2004. doi: 10.1103/PhysRevLett.92.206801.

11 TAKAHASHI, S.; MAEKAWA, S. Effect of coulomb blockade on magnetoresistance in ferromagnetic tunnel junctions. *Physical Review Letters*, v. 80, n. 8, p. 1758, 1998. doi: 10.1103/PhysRevLett.80.1758.

12 PENTEADO, P. H.; SOUZA, F. M.; SERIDONIO, A. C.; VERNEK, E.; EGUES, J. C. Scanning tunneling microscope operating as a spin diode. *Physical Review B*, v. 84, n. 12, p. 125439, 2011. doi: 10.1103/PhysRevB.84.125439.

13 ALICEA, J. New directions in the pursuit of Majorana fermions in solid state systems. *Reports on Progress in Physics*, v. 75, n. 7, p. 076501, 2012. doi: 10.1088/0034-4885/75/7/076501.

14 DIRAC, P. A. M. The quantum theory of the electron. *Philosophical Magazine*, v. 117, n. 778, p. 610, 1928. doi: 10.1098/rspa.1928.0023.

15 SCHWABL, F. *Advanced quantum mechanics*. Berlin: Springer, 2008.

16 MAJORANA, E. Teoria simmetrica dell'elettrone e del positrone. *Il Nuovo Cimento*, v. 14, n. 4, p. 171, 1937. doi: 10.1007/BF02961314.

17 WILSON, R. M. Evidence for majorana fermions in a nanowire. *Physics Today*, v. 65, n. 6, p. 14, 2012. doi: 10.1063/PT.3.1587.

18 WILCZEK, F. Majorana returns. *Nature Physis*, v. 5, n. 9, p. 614, 2009. doi: 10.1038/nphys1380.

19 FRANZ, M. Race for majorana fermions. *Physics*, v. 3, p. 24, 2010. doi: 10.1103/Physics.3.24.

20 HUGHES, T. L. Majorana fermions inch closer to reality. *Physics*, v. 4, p. 67, 2011. doi: 10.1103/Physics.4.67.

21 FRANZ, M. Majorana's wires. *Nature Nanotechnology*, v. 8, p. 3, 2013. doi: 10.1038/nnano.2013.33.

22 PHILLIPS, P. *Advanced solid state physics*. Boulder: Westview Press, 2003.

23 COLEMAN, P. *Introduction to many-body physics*. New York: Cambridge University Press, 2012.

24 ANNETT, J. F. *Superconductivity, superfluids, and condensates*. Oxford: Oxford University Press, 2004.

25 MOORE, G.; READ, N. Nonabelions in the fractional quantum Hall effect. *Nuclear Physics B*, v. 360, n. 2-3, p. 362, 1991. doi: 10.1016/0550-3213(91)90407-O.

26 READ, N.; GREEN, D. Paired states of fermions in two dimensions with breaking of parity and time-reversal symmetries and the fractional quantum Hall effect. *Physical Review B*, v. 61, n. 15, p. 10267, 2000. doi: 10.1103/PhysRevB.61.10267.

27 HASAN, M. Z.; KANE, C. L. *Colloquium*: topological insulators. *Reviews of Modern Physics*, v. 82, n. 4, p. 3045, 2010. doi: 10.1103/RevModPhys.82.3045.

28 FU, L.; KANE, C. L. Superconducting proximity effect and Majorana fermions at the surface of a topological insulator. *Physical Review Letters*, v. 100, n. 9, p. 096407, 2008. doi: 10.1103/PhysRevLett.100.096407.

29 FU, L.; KANE, C. L.; MELE, E. J. Topological insulators in three dimensions. *Physical Review Letters*, v. 98, n. 10, p. 106803, 2007. doi: 10.1103/PhysRevLett.98.106803.

30 SAU, J. D.; LUTCHYN, R. M.; TEWARI, S.; SARMA, S. D. Generic new platform for

topological quantum computation using semiconductor heterostructures. *Physical Review Letters*, v. 104, n. 4, p. 040502, 2010. doi: 10.1103/PhysRevLett.104.040502.

31 LUTCHYN, R. M.; SAU, J. D.; SARMA, S. D. Majorana fermions and a topological phase transition in semiconductor-superconductor heterostructures. *Physical Review Letters*, v. 105, n. 7, p. 077001, 2010. doi: 10.1103/PhysRevLett.105.077001.

32 OREG, Y.; REFAEL, G.; OPPEN, F. von. Helical liquids and majorana bound states in quantum wires. *Physical Review Letters*, v. 105, n. 17, p. 177002, 2010. doi: 10.1103/PhysRevLett.105.177002.

33 NILSSON, J.; AKHMEROV, A. R.; BEENAKKER, C. W. J. Splitting of a Copper pair by a pair of Majorana bound states. *Physical Review Letters*, v. 101, n. 12, p. 120403, 2008. doi: 10.1016/0550-3213(91)90407-O.

34 FU, L.; KANE, C. L. Josephson current and noise at a superconductor/quantum-spin-hall-insulator/superconductor junction. *Physical Review B*, v. 79, n. 16, p. 161408, 2009. doi: 10.1103/PhysRevB.79.161408.

35 LINDER, J.; TANAKA, Y.; YOKOYAMA, T.; SUDBØ, A.; NAGAOSA, N. Unconventional superconductivity on a topological insulator. *Physical Review Letters*, v. 104, n. 6, p. 067001, 2010. doi: 10.1103/PhysRevLett.104.067001.

36 GURARIE, V.; RADZIHOVSKY, L.; ANDREEV, A. V. Quantum phase transitions across a p-wave feshbach resonance. *Physical Review Letters*, v. 94, n. 23, p. 230403, 2005. doi: 10.1103/PhysRevLett.94.230403.

37 TEWARI, S.; SARMA, S. D.; NAYAK, C.; ZHANG, C.; ZOLLER, P. Quantum computation using vortices and majorana zero modes of a $p_x + ip_y$ superfluid of fermionic cold atoms. *Physical Review Letters*, v. 98, n. 1, p. 010506, 2007. doi: 10.1103/PhysRevLett.98.010506.

38 SATO, M.; TAKAHASHI, Y.; FUJIMOTO, S. Non-abelian topological order in s-wave superfluids of ultracold fermionic atoms. *Physical Review Letters*, v. 103, n. 2, p. 020401, 2009. doi: 10.1103/PhysRevLett.103.020401.

39 KLINOVAJA, J.; GANGADHARAIAH, S.; LOSS, D. Electric-field-induced majorana fermions in armchair carbon nanotubes. *Physical Review Letters*, v. 108, n. 19, p. 196804,

2012. doi: 10.1103/PhysRevLett.108.196804.

40 EGGER, R.; FLENSBERG, K. Emerging dirac and majorana fermions for carbon nanotubes with proximity-induced pairing and spiral magnetic field. *Physical Review B*, v. 85, n. 23, p. 235462, 2012. doi: 10.1103/PhysRevB.85.235462.

41 SAU, J. D.; TEWARI, S. Topological superconducting state and majorana fermions in carbon nanotubes. *Physical Review B*, v. 88, n. 5, p. 054503, 2013. doi: 10.1103/PhysRevB.88.054503.

42 DAS, A.; RONEN, Y.; MOST, Y.; OREG, Y.; HEIBLUM, M.; SHTRIKMAN, H. Zero-bias peaks and splitting in an Al-InAs nanowire topological superconductor as a signature of Majorana fermions. *Nature Physics*, v. 8, n. 12, p. 887, 2012. doi: 10.1038/NPHYS2479.

43 DENG, M. T.; YU, C. L.; HUANG, G. Y.; LARSSON, M.; CAROFF, P.; XU, H. Q. Anomalous zero-bias conductance peak in a Nb-InSb Nb-nanowire hybrid device. *Nano Letters*, v. 12, n. 12, p. 6414, 2012. doi: 10.1021/nl303758w.

44 LEE, E. J. H.; JIANG, X.; AGUADO, R.; KATSAROS, G.; LIEBER, C. M.; FRANCESCHI, S. D. Zero-bias anomaly in a nanowire quantum dot coupled to superconductors. *Physical Review Letters*, v. 109, n. 18, p. 186802, 2012. doi: 10.1103/PhysRevLett.109.186802.

45 FINCK, A. D. K.; HARLINGEN, D. J. V.; MOHSENI, P. K.; JUNG, K.; LI, X. Anomalous modulation of a zero-bias peak in a hybrid nanowire-superconductor device. *Physical Review Letters*, v. 110, n. 12, p. 126406, Mar 2013. doi: 10.1103/PhysRevLett.110.126406.

46 CHURCHILL, H. O. H.; FATEMI, V.; GROVE-RASMUSSEN, K.; DENG, M. T.; CAROFF, P.; XU, H. Q.; MARCUS, C. M. Superconductor-nanowire devices from tunneling to the multichannel regime: zero-bias oscillations and magnetoconductance crossover. *Physical Review B*, v. 87, n. 24, p. 241401, 2013. doi: 10.1103/PhysRevB.87.241401.

47 GOLDHABER-GORDON, D.; SHTRIKMAN, H.; MAHALU, D.; ABUSCH-MAGDER, D.; MEIRAV, U.; KASTNER, M. A. Kondo effect in a single-electron transistor. *Nature*, v. 391, n. 6663, p. 156, 1998. doi: 10.1038/34373.

48 LAW, K. T.; LEE, P. A.; NG, T. K. Majorana fermion induced resonant Andreev re-

flection. *Physical Review Letters*, v. 103, n. 23, p. 237001, Dec 2009. doi: 10.1103/PhysRevLett.103.237001.

49 PIKULIN, D. I.; DAHLHAUS, J. P.; WIMMER, M.; SCHOMERUS, H.; BEENAKKER, C. W. J. A zero-voltage conductance peak from weak antilocalization in a Majorana nanowire. *New Journal of Physics*, v. 14, n. 12, p. 125011, 2012. doi: 10.1088/1367-2630/14/12/125011.

50 KITAEV, A. Y. Unpaired Majorana fermions in quantum wires. *Physics-Uspekhi*, v. 44, n. 10S, p. 131, 2001. doi: 10.1070/1063-7869/44/10S/S29.

51 NAYAK, C.; SIMON, S. H.; STERN, A.; FREEDMAN, M.; SARMA, S. D. Non-Abelian anyons and topological quantum computation. *Reviews of Modern Physics*, v. 80, n. 3, p. 1083, 2008. doi: 10.1103/RevModPhys.80.1083.

52 KITAEV, A. Y. Fault-tolerant quantum computation by anyons. *Annals of Physics*, v. 303, n. 1, p. 2, 2003. doi: 10.1016/S0003-4916(02)00018-0.

53 LEINAAS, J.; MYRHEIM, J. On the theory of identical particles. *Il Nuovo Cimento B Series 11*, v. 37, n. 1, p. 1, 1977. doi: 10.1007/BF02727953.

54 WILCZEK, F. Magnetic flux, angular momentum, and statistics. *Physical Review Letters*, v. 48, n. 17, p. 1144, 1982. doi: 10.1103/PhysRevLett.48.1144.

55 BEENAKKER, C. Search for majorana fermions in superconductors. *Annual Review of Condensed Matter Physics*, v. 4, n. 1, p. 113, 2013. doi: 10.1146/annurev-conmatphys-030212-184337.

56 VERNEK, E.; PENTEADO, P. H.; SERIDONIO, A. C.; ; EGUES, J. C. Majorana sneakily leaking into a quantum dot connected to a kitaev wire. *arXiv:1308.0092*.

57 STONER, E. C. Collective electron ferromagnetism. ii. energy and specific heat. *Proceedings of the Royal Society of London A*, v. 169, n. 938, p. 339, 1939. doi: 10.1098/rspa.1939.0003.

58 SOUZA, F. M.; EGUES, J. C.; JAUHO, A. P. TMR effect in a FM-QD-NM system. *Brazilian Journal of Physics*, v. 34, n. 2B, p. 565, 2004.

59 HAUG, H.; JAUHO, A.-P. *Quantum kinetics in transport and optics of semiconductors*. Berlin: Springer, 2008.

60 RAMMER, J.; SMITH, H. Quantum field-theoretical methods in transport theory of metals. *Reviews of Modern Physics*, v. 58, n. 2, p. 323, Apr 1986. doi: 10.1103/RevModPhys.58.323.

61 BRUUS, H.; FLENSBERG., K. *Many-body quantum theory in condensed matter physics an introduction*. New York: Oxford University Press, 2004.

62 SOUZA, F. M. de. *Transporte quântico em spintrônica: corrente e shot noise via funções de Green de não-equilíbrio*. 2004. 166 p. Tese (Doutorado) — Instituto de Física de São Carlos, Universidade de São Paulo, São Carlos, 2004.

63 RAMMER, J. *Quantum field theory of non-equilibrium states*. New York: Cambridge University Press, 2007.

64 LANGRETH, D. C. *Linear and nonlinear electron transport in solids*. New York: Plenum Publishers, 1976.

65 FIETE, G. A.; HELLER, E. J. *Colloquium*: theory of quantum corrals and quantum mirages. *Reviews of Modern Physics*, v. 75, n. 3, p. 933–948, 2003. doi: 10.1103/RevModPhys.75.933.

66 TERSOFF, J.; HAMANN, D. R. Theory of the scanning tunneling microscope. *Physical Review B*, v. 31, n. 2, p. 805, 1985. doi: 10.1103/PhysRevB.31.805.

67 PLIHAL, M.; GADZUK, J. W. Nonequilibrium theory of scanning tunneling spectroscopy via adsorbate resonances: Nonmagnetic and Kondo impurities. *Physical Review B*, v. 63, n. 8, p. 085404, 2001. doi: 10.1103/PhysRevB.63.085404.

68 MEIR, Y.; WINGREEN, N. S. Landauer formula for the current through an interacting electron region. *Physical Review Letters*, v. 68, n. 16, p. 2512, 1992. doi: 10.1103/PhysRevLett.68.2512.

69 LANDAUER, R. Electrical resistance of disordered one-dimensional lattices. *Philosophical Magazine*, v. 21, n. 172, p. 863, 1970. doi: 10.1080/14786437008238472.

70 VERNEK, E.; SANDLER, N.; ULLOA, S. E. Kondo screening suppression by spin-orbit interaction in quantum dots. *Physical Review B*, v. 80, n. 4, p. 041302, 2009. doi: 10.1103/PhysRevB.80.041302.

71 SUN, Q.-f.; WANG, J.; GUO, H. Quantum transport theory for nanostructures with Rashba spin-orbital interaction. *Physical Review B*, v. 71, n. 16, p. 165310, 2005. doi: 10.1103/PhysRevB.71.165310.

72 RUDZINSKI, W.; J., B. Tunnel magnetoresistance in ferromagnetic junctions: tunneling through a single discrete level. *Physical Review B*, v. 64, n. 8, p. 085318, 2001. doi: 10.1103/PhysRevB.64.085318.

73 AVOURIS I.W. LYO, R. E. W. P.; HASEGAWA, Y. Real space imaging of electron scattering phenomena at metal surfaces. *Journal of Vaccum Science & Technology B*, v. 12, n. 3, p. 1447, 1994. doi: 10.1116/1.587314.

74 KANISAWA, K.; BUTCHER, M. J.; YAMAGUCHI, H.; HIRAYAMA, Y. Imaging of Friedel oscillation patterns of two-dimensionally accumulated electrons at epitaxially grown inas(111) *A* surfaces. *Physical Review Letters*, v. 86, n. 15, p. 3384, 2001. doi: 10.1103/PhysRevLett.86.3384.

75 AFFLECK, I.; BORDA, L.; SALEUR, H. Friedel oscillations and the Kondo screening cloud. *Physical Review B*, v. 77, n. 18, p. 180404, 2008. doi: 10.1103/PhysRevB.77.180404.

76 ALICEA, J. Majorana fermions in a tunable semiconductor device. *Physical Review B*, v. 81, n. 12, p. 125318, 2010. doi: 10.1103/PhysRevB.81.125318.

77 SAU, J. D.; TEWARI, S.; LUTCHYN, R. M.; STANESCU, T. D.; SARMA, S. D. Non-Abelian quantum order in spin-orbit-coupled semiconductors: search for topological Majorana particles in solid-state systems. *Physical Review B*, v. 82, n. 21, p. 214509, 2010. doi: 10.1103/PhysRevB.82.214509.

78 STANESCU, T. D.; TEWARI, S. Majorana fermions in semiconductor nanowires: fundamentals, modeling, and experiment. *Journal of Physics: Condensed Matter*, v. 25, n. 23, p. 233201, 2013. doi: 10.1088/0953-8984/25/23/233201.

79 IVANOV, D. A. Non-Abelian statistics of half-quantum vortices in p-wave superconduc-

tors. *Physical Review Letters*, v. 86, n. 2, p. 268, 2001. doi: 10.1103/PhysRevLett.86.268.

80 ZHANG, C.; TEWARI, S.; LUTCHYN, R. M.; SARMA, S. D. $p_x + ip_y$ superfluid from s-wave interactions of fermionic cold atoms. *Physical Review Letters*, v. 101, n. 16, p. 160401, 2008. doi: 10.1103/PhysRevLett.101.160401.

81 KRAUS, Y. E.; AUERBACH, A.; FERTIG, H. A.; SIMON, S. H. Majorana fermions of a two-dimensional $p_x + ip_y$ superconductor. *Physical Review B*, v. 79, n. 13, p. 134515, 2009. doi: 10.1103/PhysRevB.79.134515.

82 FU, L.; KANE, C. L. Probing neutral Majorana fermion edge modes with charge transport. *Physical Review Letters*, v. 102, n. 21, p. 216403, 2009. doi: 10.1103/PhysRevLett.102.216403.

83 AKHMEROV, A. R.; NILSSON, J.; BEENAKKER, C. W. J. Electrically detected interferometry of Majorana fermions in a topological insulator. *Physical Review Letters*, v. 102, n. 21, p. 216404, 2009. doi: 10.1103/PhysRevLett.102.216404.

84 COOK, A.; FRANZ, M. Majorana fermions in a topological-insulator nanowire proximity-coupled to an s-wave superconductor. *Physical Review B*, v. 84, n. 20, p. 201105, 2011. doi: 10.1103/PhysRevB.84.201105.

85 SATO, M.; FUJIMOTO, S. Topological phases of noncentrosymmetric superconductors: edge states, Majorana fermions, and non-Abelian statistics. *Physical Review B*, v. 79, n. 9, p. 094504, 2009. doi: 10.1103/PhysRevB.79.094504.

86 POTTER, A. C.; LEE, P. A. Topological superconductivity and Majorana fermions in metallic surface states. *Physical Review B*, v. 85, n. 9, p. 094516, 2012. doi: 10.1103/PhysRevB.85.094516.

87 KLINOVAJA, J.; FERREIRA, G. J.; LOSS, D. Helical states in curved bilayer graphene. *Physical Review B*, v. 86, n. 23, p. 235416, 2012. doi: 10.1103/PhysRevB.86.235416.

88 FULGA, I. C.; HAIM, A.; AKHMEROV, A. R.; OREG, Y. Adaptive tuning of Majorana fermions in a quantum dot chain. *New Journal of Physics*, v. 15, n. 4, p. 045020, 2013. doi: 10.1088/1367-2630/15/4/045020.

89 NIELSSEN, H.; NINOMIYA, N. The Adler-Bell-Jackiw anomaly and Weyl fermions in a crystal. *Physics Letters B*, v. 130, n. 6, p. 389, 1983. doi: 10.1016/0370-2693(83)91529-0.

90 SANTOS, L.; RYU, S.; CHAMON, C.; MUDRY, C. Topological qubits in graphenelike systems. *Physical Review B*, v. 82, n. 16, p. 165101, 2010. doi: 10.1103/PhysRevB.82.165101.

91 JACKIW, R.; ROSSI, P. Zero modes of the vortex-fermion system. *Nuclear Physics B*, v. 190, n. 4, p. 681, 1981. doi: 10.1016/0550-3213(81)90044-4.

92 ALICEA, J.; OREG, Y.; REFAEL, G.; OPPEN, F. von; FISHER, M. P. A. Non-abelian statistics and topological quantum information processing in 1d wire networks. *Nature Physics*, v. 7, n. 5, p. 412, 2011. doi: 10.1038/NPHYS1915.

93 TEWARI, S.; STANESCU, T. D.; SAU, J. D.; SARMA, S. D. Topological minigap in quasi-one-dimensional spin-orbit-coupled semiconductor Majorana wires. *Physical Review B*, v. 86, n. 2, p. 024504, 2012. doi: 10.1103/PhysRevB.86.024504.

94 TINKHAM, M. *Introduction to superconductivity*. New York: Dover, 1996.

95 BYCHKOV, Y. A.; RASHBA, E. I. Oscillatory effects and the magnetic susceptibility of carriers in inversion layers. *Journal of Physics C: Solid State Physics*, v. 17, n. 33, p. 6039, 1984. doi: 10.1088/0022-3719/17/33/015.

96 DRESSELHAUS, G. Spin-orbit coupling effects in zinc blende structures. *Physical Review*, v. 100, n. 2, p. 580, 1955. doi: 10.1103/PhysRev.100.580.

97 JOSEPHSON, B. D. Coupled superconductors. *Reviews of Modern Physics*, v. 36, n. 1, p. 216, 1964. doi: 10.1103/RevModPhys.36.216.

98 DATTA, S.; DAS, B. Electronic analog of the electro-optic modulator. *Applied Physics Letters*, v. 56, n. 7, p. 665, 1990. doi: 10.1063/1.102730.

99 WINKLER, R. Rashba spin splitting and Ehrenfest's theorem. *Physica E: Low-dimensional Systems and Nanostructures*, v. 22, n. 1, p. 450, 2004. doi: 10.1016/j.physe.2003.12.043.

100 CALSAVERINI, R. S.; BERNARDES, E.; EGUES, J. C.; LOSS, D. Intersubband-induced spin-orbit interaction in quantum wells. *Physical Review B*, v. 78, n. 15, p. 155313, 2008. doi: 10.1103/PhysRevB.78.155313.

101 LEIJNSE, M.; FLENSBERG, K. Scheme to measure Majorana fermion lifetimes using a quantum dot. *Physical Review B*, v. 84, n. 14, p. 140501, 2011. doi: 10.1103/PhysRevB.84.140501.

102 LIU, D. E.; BARANGER, H. U. Detecting a Majorana-fermion zero mode using a quantum dot. *Physical Review B*, v. 84, n. 20, p. 201308(R), 2011. doi: 10.1103/PhysRevB.84.201308.

103 MEIR, Y.; WINGREEN, N. S.; LEE, P. A. Transport through a strongly interacting electron system: Theory of periodic conductance oscillations. *Physical Review Letters*, v. 66, n. 23, p. 3048, 1991. doi: 10.1103/PhysRevLett.66.3048.

104 PRADA, E.; SAN-JOSE, P.; AGUADO, R. Transport spectroscopy of *ns* nanowire junctions with Majorana fermions. *Physical Review B*, v. 86, n. 18, p. 180503, 2012. doi: 10.1103/PhysRevB.86.180503.

105 RAINIS, D.; TRIFUNOVIC, L.; KLINOVAJA, J.; LOSS, D. Towards a realistic transport modeling in a superconducting nanowire with Majorana fermions. *Physical Review B*, v. 87, n. 2, p. 024515, 2013. doi: 10.1103/PhysRevB.87.024515.

106 FERRY, S. M. G. D. K.; BIRD, J. *Transport in nanostructures*. New York: Cambridge University Press, 2009.

107 LEE, M.; LIM, J. S.; LÓPEZ, R. Kondo effect in a quantum dot side-coupled to a topological superconductor. *Physical Review B*, v. 87, n. 24, p. 241402(R), 2013. doi: 10.1103/PhysRevB.87.241402.

108 ZUBAREV, D. N. Double-time green functions in statistical physics. *Soviet Physics Uspekhi*, v. 3, n. 3, p. 320, 1960. doi: 10.1070/PU1960v003n03ABEH003275.

APPENDICES

Appendix A

Some analytical results

In this appendix, we present in more detail the derivation of Eq. (4.34) and some results that can be obtained analytically from it. In particular, we show how to determine the density of states of a semi-infinite tight binding chain, a result that we use to model the source and drain leads of our system.

As shown in section 4.2.1 [Eq. (4.26)], the dot Green's function in the Majorana representation for $t_0 = 0$ is given by

$$\bar{G}_{dd}(\varepsilon) = \left[\mathbf{I}_{2\times 2} - \bar{g}_d(\varepsilon) V_0(\varepsilon)\right]^{-1} \bar{g}_d(\varepsilon), \tag{A.1}$$

or more explicitly

$$\bar{G}_{dd}(\varepsilon) = \frac{1}{\left(1 - \frac{\mu_0^2 g_d^2}{4}\right)} \begin{pmatrix} g_d & i\frac{\mu_0 g_d^2}{2} \\ -i\frac{\mu_0 g_d^2}{2} & g_d \end{pmatrix}. \tag{A.2}$$

To determine $G_{dd}(\varepsilon)$ we use Eq. (4.13),

$$\begin{aligned} G_{dd}(\varepsilon) &= \frac{g_d(2 - \mu_0 g_d)}{\left(4 - \mu_0^2 g_d^2\right)} \\ &= \frac{g_d}{2 + \mu_0 g_d} \\ &= \frac{1}{2\left(g_d^{-1} + \frac{\mu_0}{2}\right)} \\ &= \frac{1}{\varepsilon - \Sigma_L + \mu_0 + i\eta} \end{aligned} \tag{A.3}$$

and finally obtain

$$G_{dd}(\varepsilon) = \frac{1}{\varepsilon - \varepsilon_{\mathrm{dot}} - \sum_{\mathbf{k},\ell} |V_{\ell\mathbf{k}}|^2 (\varepsilon - \varepsilon_{\ell\mathbf{k}})^{-1} + i\eta}, \tag{A.4}$$

in which we have used the definitions of g_d, Σ_L and μ_0 (see section 4.2.1). This result could have been equally derived by using the electron representation.

In order to determine an analytical expression for the dot DOS and for the conductance, we need to work on Eq. (A.4). We first have to calculate $\sum_{\mathbf{k},\ell} |V_{\ell\mathbf{k}}|^2 (\varepsilon - \varepsilon_{\ell\mathbf{k}})^{-1}$, which as we shall see, is directly connected to the density of states of the leads ρ_ℓ. By assuming that the coupling between the dot and leads is k-independent $V_{\ell\mathbf{k}} = V_\ell$ and converting the sum in $\mathbf{k}$ into an integral (1D case), we obtain

$$\begin{aligned} \sum_{\mathbf{k}} \frac{1}{\omega \pm \varepsilon_{\ell\mathbf{k}} + i\eta} &= P \sum_{\mathbf{k}} \frac{1}{\omega \pm \varepsilon_{\ell\mathbf{k}}} - i\pi \sum_{\mathbf{k}} \delta(\omega \pm \varepsilon_{\mathbf{k}}) \\ &= P \int_{-D}^{D} d\varepsilon \frac{\rho_\ell(\varepsilon)}{\omega \pm \varepsilon} - i\pi \rho_\ell(\omega), \end{aligned} \tag{A.5}$$

where P stands for the principal value of the integral and $D = 10t$ is the half-bandwidth of the leads conduction band. Note here that we are using a general formulation, i.e., in principle the density of states of the source and drain leads can be different. As we already mentioned, the DOS is connected to the imaginary part of the Green's function $\rho_\ell(\varepsilon) = -\frac{1}{\pi}\mathrm{Im}G_\ell(\varepsilon)$, in which G_ℓ is the lead Green's function. Below we show a relation between the real and imaginary parts of G_ℓ (108),

$$\begin{aligned} \mathrm{Re}G_\ell(\omega) &= -\frac{P}{\pi} \int_{-\infty}^{\infty} d\varepsilon \frac{\mathrm{Im}G_\ell(\omega)}{\omega - \varepsilon} = P \int_{-\infty}^{\infty} d\varepsilon \frac{\rho_\ell(\varepsilon)}{\omega - \varepsilon} \quad \text{(a)} \\ \mathrm{Re}G_\ell(\omega) &= \frac{P}{\pi} \int_{-\infty}^{\infty} d\varepsilon \frac{\mathrm{Im}G_\ell(\omega)}{\omega + \varepsilon} = -P \int_{-\infty}^{\infty} d\varepsilon \frac{\rho_\ell(\varepsilon)}{\omega + \varepsilon} \quad \text{(b)}, \end{aligned} \tag{A.6}$$

where in the latter we have used $\rho(-\varepsilon) = \rho(\varepsilon)$, which as we will see is the case in our system.

Substituting Eqs. (A.6) into (A.5) we have

$$\begin{aligned} \sum_{\mathbf{k}} \frac{1}{\omega - \varepsilon_{\ell\mathbf{k}} + i\eta} &= \mathrm{Re}G_\ell(\omega) - i\pi\rho_\ell(\omega) \quad \text{(a)} \\ \sum_{\mathbf{k}} \frac{1}{\omega + \varepsilon_{\ell\mathbf{k}} + i\eta} &= -\mathrm{Re}G_\ell(\omega) - i\pi\rho_\ell(\omega) \quad \text{(b)}. \end{aligned} \tag{A.7}$$

The task then is to calculate the Green's functions of the leads. To do so, we suppose they are constituted of a normal semi-infinite metallic wire modeled by a tight-binding chain. The

Hamiltonian of the system can be written as

$$H = -t \sum_{j=1}^{\infty} \left(c_j^{\dagger} c_{j+1} + c_{j+1}^{\dagger} c_j \right), \tag{A.8}$$

where we assumed the chemical potential (Fermi energy) is zero and the hopping parameter $t = D/2$, see Fig. A.1(a). The "real" system we solve Fig. A.1(b), however, is composed of site 1, whose free Green's function is $g_1(\omega) = 1/(\omega + i\eta)$ and a renormalized site $\tilde{2}$, to which we attribute a Green's function $\tilde{g}_2$ to be determined. By applying the equation of motion technique we obtain

$$G_{11}(\omega) = g_1(\omega) + g_1(\omega)(-t)\tilde{G}_{21}(\omega) \tag{A.9}$$

and

$$\tilde{G}_{21}(\omega) = \tilde{g}_2(\omega)(-t)G_{11}(\omega). \tag{A.10}$$

Using the expression above in (A.9) we have

$$\left(1 - g_1 t^2 \tilde{g}_2\right) G_{11} - g_1 = 0, \tag{A.11}$$

but from Fig. A.1(d) we know that $G_{11} = \tilde{g}_2 \equiv \tilde{g}$, i.e., if another site is added to the chain, the already renormalized Green's function essentially does not change (remember that we are treating a semi-infinite chain). We now solve Eq. (A.11) for $\tilde{g}(\omega)$ (quadratic equation) and find

$$\tilde{g}(\omega) = \frac{1 - \sqrt{1 - 4 g_1(\omega)^2 t^2}}{2 g_1(\omega) t^2}, \tag{A.12}$$

where we have already chosen the minus sign, which guarantees that for $\omega \gg t$, $\tilde{g}(\omega) \to 1/\omega$.

The Green's function $\tilde{g}(\omega)$ is what we previously called $G_{\ell}(\omega)$. The real and imaginary (ρ_{ℓ}) parts of $G_{\ell}(\omega)$ are given by

$$\rho_{\ell}(\omega) = \frac{1}{2\pi t^2} \sqrt{4t^2 - \omega^2}\, \theta(2t - \omega)\, \theta(2t + \omega) \tag{A.13}$$

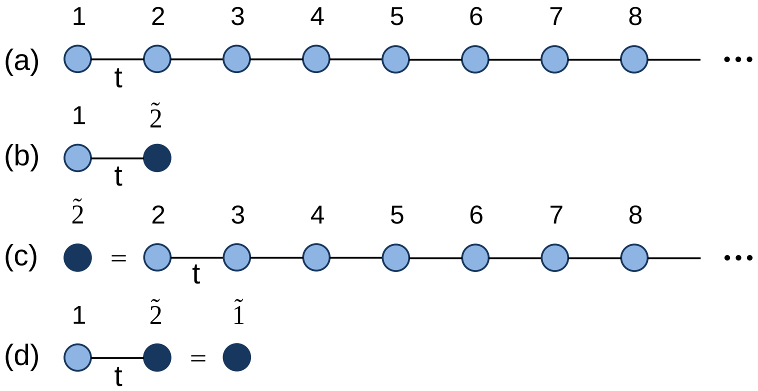

Figure A.1 – Semi-infinite wire modeling the leads of our setup (a). The sites are coupled by a hopping parameter $t = D/2$. In (b) we illustrate the "real" coupled system we solve: a site 1 of the original chain connected to a site $\tilde{2}$ renormalized by the rest of the chain (c). If another site is added to the already renormalized site nothing changes essentially, that is $\tilde{1} = \tilde{2}$" (d).

and

$$\mathrm{Re}G_\ell(\omega) = \begin{cases} \dfrac{\omega}{2t^2} & \omega < |2t| \\ \\ \dfrac{\omega}{2t^2}\left(1 - \dfrac{\sqrt{\omega^2 - 4t^2}}{|\omega|}\right) & \omega > |2t|, \end{cases} \tag{A.14}$$

in which $2t = D$ corresponds to the edge of the conduction band. In Fig. A.2 we plot these two quantities as functions of the energy ($\omega \to \varepsilon$). We can see that the DOS is symmetric as we stated before and non-zero only within $[-2t, 2t]$. The real part, however, is linear in ε in this interval, which leads to kinks in the conductance of the system as a function of the chemical potential of the wire (see Sec. 4.3). Note that we use L as the index of $G_L(\varepsilon)$ and $\rho_L(\varepsilon)$. This is so because we consider leads symmetrically coupled to the dot.

Finally, we write the dot Green's function (A.4) as

$$G_{dd}(\varepsilon) = \frac{1}{\varepsilon - \varepsilon_{\mathrm{dot}} - \Lambda(\varepsilon) + i\Gamma_L(\varepsilon) + i\eta}, \tag{A.15}$$

where $\Lambda(\varepsilon) = 2|V_L|^2\mathrm{Re}G_L(\varepsilon)$ and $\Gamma_L(\varepsilon) = 2\pi|V_L|^2\rho_L(\varepsilon)$. The dot DOS and the conductance are given, respectively, by

$$\begin{aligned} \rho_{\mathrm{dot}}(\varepsilon) &= -\frac{1}{\pi}\mathrm{Im}G_{dd}(\varepsilon) \\ &= \frac{1}{\pi}\frac{\Gamma_L^2}{(\varepsilon - \varepsilon_{\mathrm{dot}} - \Lambda_L)^2 + \Gamma_L^2} \end{aligned} \tag{A.16}$$

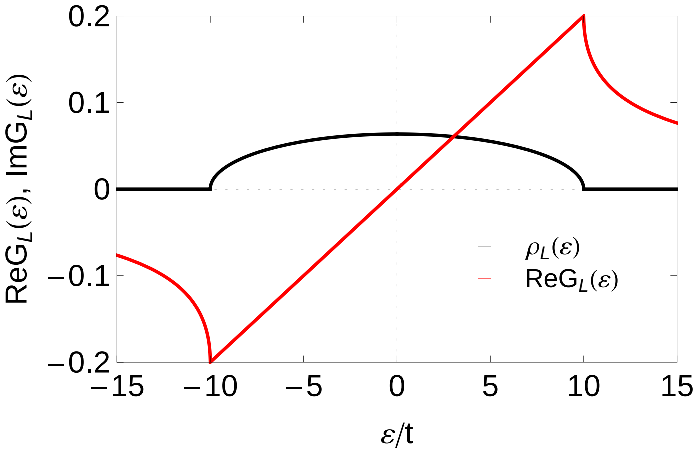

Figure A.2 – Linear behavior of the real part (red curve) of $G_L(\varepsilon)$ within the edges of the conduction band $D = 10t$, $t = 10$ meV, and DOS of the leads (black curve).

and

$$G\left[e^2/h\right] = \frac{\Gamma_L^2}{\left(\varepsilon_{\mathrm{dot}} + \Lambda_L(0)\right)^2 + \Gamma_L^2}. \tag{A.17}$$